

Enhancing Ion Transport in Thick Li-Ion Battery Electrodes by Pore Engineering

A Dissertation

Presented to

The Academic Faculty

by

Doyoub Kim

In Partial Fulfillment

of the Requirements for the Degree

Doctor of Philosophy in the

School of Materials Science and Engineering

Georgia Institute of Technology

August 2023

COPYRIGHT © 2023 BY DOYOUNG KIM

Enhancing Ion Transport in Thick Li-Ion Battery Electrodes by Pore Engineering

Approved by:

Dr. Gleb Yushin, Advisor
School of Materials
Science and Engineering
Georgia Institute of Technology

Dr. Faisal Alamgir
School of Materials
Science and Engineering
Georgia Institute of Technology

Dr. Ting Zhu (MSE/ME)
School of Materials
Science and Engineering
Georgia Institute of Technology

Dr. Alexander Alexeev
School of Mechanical Engineering
Georgia Institute of Technology

Dr. Seung Woo Lee
School of Mechanical Engineering
Georgia Institute of Technology

Date Approved: July 21, 2023

To my parents

ACKNOWLEDGEMENTS

Throughout my journey, numerous people have added a bit of adventure and countless people to thank. I would like to express my sincere gratitude to the people who have provided guidance, unwavering encouragement, and support at every stage of my journey. It would not have been possible without my academic advisor, thesis committee members, collaborators, lab mates, friends and most importantly my family.

First of all, I would like to express my deepest gratitude to Dr. Gleb Yushin, who has been an indispensable person in my research journey. His unwavering support, patience, guidance and enthusiasm for research allowed me to mature significantly as an independent researcher, project manager and raised the caliber of my work. The growth I have experienced under his mentorship has been invaluable.

I am deeply grateful to my thesis committee members: Dr. Alamgir, Dr. Alexeev, Dr. Zhu and Dr. Lee for their invaluable insights for their invaluable guidance and constructive feedback. Their invaluable insights and guidance helped me strengthen my research and shape the direction of my research throughout my journey. Your expertise and dedication have been crucial in refining my research and questions and suggestions have pushed me to dig deeper and broaden my perspective.

To my collaborators, thank you for your time, invaluable discussions, and support. I was fortunate to work with Dr. Alexandre Magasinski, Aashray Narla, Ashwin Sankara Raman, and Dr. Samik Jhulki. Their help was invaluable in exploring the project and discussing to overcome the challenges throughout the research projects. I would like to extend my sincere thanks to my collaborators Dr. Yueyi (Diana) Sun, Dr. Baolin Wang, Abiram Krishnan, Dr. Alexeev, Dr. Zhu and Dr. Alamgir from Georgia Institute of Technology for their work have helped me and inspired me in many ways.

To my current and former lab mates, I want to express my gratitude for their contributions and support during our time working together. In particular, I would like to thank Dr. Ah-young Song and Dr. Dong-Chan Lee for helping me get settled in the first few months of the program and for our conversations on various topics ranging from personal to research issues, inspiring me not to fall back but to keep moving forward and expand my research during some difficult years of my journey. I would also like to thank Dr. Jim Benson for training me on experimental tools both in and out of the lab during the first few months of my Ph.D. program. I would like to thank Aashray Narla and Dr. Fujia Wang for their camaraderie throughout my Ph.D. I would like to thank Dr. Wenbin Fu for the guidance and conversations we had, especially in the last few years, about research and careers after the PhD. I would like to express my gratitude to Dr. Anirudth Ramanujapuram, Dr. Dan Gordon, Dr. Enbo Zhao, Dr. Chenchen Hu, Anirudth Ramanujapuram, Dr., Enbo Zhao, Dr. Xiaolei Ren, Dr. Shunrui Luo, Dr. Zifei Sun, Dr. Rebecca Glaser, Dr. Billy Johnson, Crystal Jain, Dr. Mengting Liu, Dr. Yiran Xiao, Dr. Wenqiang Hu, Vismay Chandra, Rishika Jakhar, Peter Wang, Yice Wang and Navneeth Rajiv.

I was fortunate to have had the opportunity to work with such highly motivated students: Kyle Hunady, Ritvik Sriram and Kaixi (Kevin) Chen. Their diligence and curiosity, in turn, have allowed me to grow as a mentor. I am deeply grateful for this enriching experience.

I would like to express my heartfelt gratitude to my dear friends: Han Kyul, Hoseok, Junghwan, who have steadfastly stood as my pillars of strength throughout this Ph.D. journey. Despite being scattered in different parts of the U.S. and Hong Kong, our shared memories through virtual platforms have been sources of immense comfort and joy. To Han Kyul and Hoseok, your unwavering support, encouragement, and faith, as well as our conversations

while meeting in different cities in the U.S. have always served as a motivating force during the most difficult times. A special mention to Han Kyul - I wish you the best of luck in the remaining years of your Ph.D. program. I have the utmost confidence in your ability to complete it successfully. To Jiyun, thank you for your support and I wish you the best of luck in your future ahead.

In closing, I would like to express my deepest gratitude to my parents for their sacrifice, unconditional love, unwavering faith, and tireless support. Without them, this journey would not have been possible. No words can truly describe what you have done for me and the depth of my appreciation. I am incredibly blessed to call you my family. I dedicate this work to both of you.

Table of Contents

ACKNOWLEDGMENTS	iv
LIST OF TABLE(S)	x
LIST OF FIGURES	xi
LIST OF ABBREVIATIONS	xix
SUMMARY	xx
CHAPTER 1. Introduction	1
1.1 Background on the need for lithium-ion battery research	1
1.2 Theoretical background of lithium-ion battery	4
1.3 Development in lithium-ion battery material research	10
1.3.1 Cathode materials	10
1.3.2 Anode materials	11
CHAPTER 2. Motivation and Research Objectives	13
2.1 Electrode design considerations	13
2.2 Motivation behind thick and dense electrodes and their limitations	15
2.3 Research design and objectives	18
CHAPTER 3. Sparsely laser-patterned tapered channels in thick and dense high-nickel NCA electrode	21
3.1 Introduction	21
3.2 Experimental Methods	23
3.2.1 Preparation of electrode	23
3.2.2 Material Characterizations	23
3.2.3 Electrochemical Tests	25
3.2.4 Simulation methods	25

3.3	Results and discussion	27
3.4	Conclusion	40
3.5	Supplementary figures	41
CHAPTER 4	Fast-rate, high loading laser-micromachined graphite and silicon blended graphite lithium-ion battery anodes	50
4.1	Introduction	50
4.2	Experimental Methods	51
4.2.1	Preparation of electrode	51
4.2.2	Material Characterizations	51
4.2.3	Electrochemical Tests	52
4.3	Results and discussion	53
4.4	Conclusion	61
4.5	Supplementary figures	62
CHAPTER 5	Micropillar channel patterning in high loading graphite and silicon blended graphite anodes	64
5.1	Introduction	64
5.2	Experimental Methods	65
5.2.1	Material	65
5.2.2	Fabrication of a micropillar template	65
5.2.3	Material characterization	66
5.2.4	Electrochemical Tests	67
5.3	Results and discussion	68
5.4	Conclusion	75
CHAPTER 6	Conclusion and future work	76
6.1	Conclusion	76
6.2	Future work	77

APPENDICES**79**

A.1 Permission for the Reuse of Copyright Materials

A.2 US Patent

A.3 Korea Patent

REFERENCES**82**

LIST OF TABLE(S)

Table 2.1 Theoretical mass loss of each hexagonal array pattern with different shaped holes.....**20**

LIST OF FIGURES

Figure 1.1	Observed cell prices from 1991 to 2021 (Reproduced with permission from Ref. 7).....	2
Figure 1.2	Energy density comparison among different energy storage systems (Reproduced with permission from Ref. 12)	3
Figure 1.3	Example of battery components and different form factors (Reproduced with permission from Ref. 12).....	4
Figure 1.4	Lithium-ion battery schematic illustration (Reproduced with permission from Ref. 17).....	6
Figure 2.1	Schematic of the femto-second laser treatment of thick battery electrode.....	18
Figure 2.2	Experimental design of hexagonal array pattern with different hole diameter and spacing.....	19
Figure 3.1	Illustration of laser patterning and its effects. a. The schematic diagram shows the role of laser treatment in reducing tortuosity and improving electrolyte wetting and ion transport, thereby enhancing the electrochemical rate performance of thick and dense battery electrodes. b. The graph shows the achievable energy density at high current density when using thick and dense electrodes laser-patterned with a dense laser pattern. c. The table provides examples of electrode material losses for various patterns, demonstrating that minimal electrode losses (0.1% to 8%) can be achieved with appropriate pattern architecture.....	28
Figure 3.2	Material characterization of channel formation and morphology within a high-nickel NCA electrode with a capacity of 6 mAh/cm ² . a. X-ray diffraction of the electrode before and after laser patterning, demonstrating the absence of deleterious structural changes regardless of residual laser heat. The representative top-view SEM images show the effective formation of b. hexagonal array channel patterns extending from 30 μm to 100 μm. c. SEM cross section of a 30 μm – 100 μm laser-patterned electrode showing the formation of tapered channels. Energy dispersive X-ray spectroscopy (EDS) mapping of the laser-patterned electrode provides an elemental map, where red and purple represent elements introduced during epoxy preparation for the cross-sectional imaging, and light green, sky blue, dark green, and orange are from the high-nickel NCA electrode and aluminum current collector, respectively. Supplementary Figure S3-1 provides additional information on the elements. Note that 30 μm – 100 μm represents the upper diameter of the channel and, correspondingly, the distance between the closest channels.....	29

Figure 3.3 Electrochemical performance comparison of pristine and laser-patterned electrodes with capacities of 4.8 mAh/cm² and 6 mAh/cm². Discharge rate capability tests for a. pristine and laser-patterned b. 30 μm – 100 μm and c. 50 μm – 100 μm, for the 4.8 mAh/cm² electrode samples. The charge rate was held constant at 0.1C for the 0.1C cycle and 0.2C for the 1C and 2C discharge rate cycles. d. The discharge rate capacities shown in Figures 3.a, 3.b, and 3.c were normalized based on the capacities obtained at 0.1C. For the 6 mAh/cm² electrodes, additional discharge rate capability experiments were conducted for e. pristine and laser patterned f. 30m - 100m, g. 50m - 100m, and h. 50 μm – 450 μm. For these experiments, the charge rate was 0.1C for the 0.1C cycle and 0.2C for the 0.2C, 0.5C, 1C, and 2C cycles. i. The discharge rate capacities in Figures 3.a, 3.b, and 3.c have been normalized based on the capacities secured at 0.1C. j. Figure 3d and k. Figure 3i are bar graphs of the normalized capacities derived from j. Figure. 3d k. Figure 3i.....**31**

Figure 3.4 Effect of laser patterning on tortuosity and diffusivity as a function of channel size and channel spacing. The normalized Nyquist plot obtained for a. different laser-patterned channel sizes with channel spacing set to 100 μm. and b. different channel sizes with channel spacing set to 4.8 mAh/cm². c. Table of McMullin numbers derived by linearly fitting the impedance of symmetric cells. The Nyquist plot obtained for d. Different laser-patterned channel sizes while channel spacing was set to 100 μm and e. Different channel spacing while channel size was fixed at 100 μm for a loading of 6 mAh/cm². f. Table of McMullin numbers derived from linear fitting of the impedance obtained from symmetric cells in Figures 4d and 4e. The laser treatment induces a periodic array of conical channels in a porous electrode matrix. g. Geometry of a laser-patterned hexagonal array electrode with conical channels of different porosity in the upper and lower halves of the electrode. The top corresponds to 10% porosity, while the bottom, closest to the Al foil, corresponds to 18% porosity, for a total porosity of 14% for the entire electrode (Supplementary Figure S3-3). h. Contour plot of the normalized effective diffusivity based on the steady-state decrease in electrolyte concentration across the laser-patterned hexagonal array electrode at a load of 6 mAh/cm² when the electrode thickness excluding the Al foil was fixed at 80 μm.....**35**

Figure 3.5 Evaluation of the effect of laser patterning on electrolyte absorption. Electrode immersion measurements reveal the rate of electrolyte impregnation into laser-patterned electrodes with varying a. channel diameters and b. channel spacing during the first 300 seconds after immersion in 1M LiPF₆ EC:DEC (V:V = 1:1) solution. c. Depicts the geometric representation of a single unit of NCA cathodes based on hole patterning, with each unit exhibiting periodic side boundaries. d. COMSOL simulations reveal that the presence of laser-patterned perforations enhances ion transport in the modeled electrode elements. The depicted unit has a side length of 100 μm and a height of 80 μm, and its openings have end diameters of 20 μm and 40 μm. The simulation result depicts the time necessary for the average electrolyte concentration to permeate pristine and laser-patterned electrodes.....**37**

Supplementary

Figure S3-1.....**41**

The EDS of the cross-section of the laser patterned electrode with the conical-shaped channels shown in Figure 3.2d. The corresponding EDS elemental mapping of a. C b. O c. Ni d. Al e. Co

Supplementary

Figure S3-2.....**41**

Optical images of the cross-section of laser patterned 6 mAh/cm² electrodes with channel sizes of a. 30 μm and b. 50 μm in diameter with different spacings

Supplementary

Figure S3-3.**42**

Nano-Computed Tomography (nano-CT) images of the cross-section of a pristine 4.8 mAh/cm² electrode and the measured porosity values for different layers of the electrode. The light green and yellow layers correspond to the bottom layer closer to the Al foil and the top layer further away from the Al foil, respectively.

Supplementary

Figure S3-4.....43

Electrochemical performance of pristine and laser-patterned 6 mAh/cm² Discharge Rate Capabilities of Unpatterned and Laser-Patterned Electrodes. The following graphs show discharge rate capability experiments for a. unpatterned electrodes and b., c., and d. laser-patterned electrodes with dimensions of 50 μm - 100 μm, 50 μm - 450 μm, and 50 μm - 700 μm, respectively. In these experiments, the charge rate remained constant at 0.1C for the 0.1C cycle and at 0.2C for the 0.2C, 0.5C, 1C, and 2C discharge rates. e. Shows the discharge rate capacities derived from Supplementary Figures S3-4a, S3-4b, S3-4c, and S3-4d, all normalized relative to the discharge rate capacities initially obtained at 0.1C

Supplementary

Figure S3-5.44

Electrochemical performance of pristine and laser-patterned 6 mAh/cm² Comparison of discharge rate capabilities of pristine and Laser-Patterned Electrodes. The graphs shows discharge rate capability experiments for a. pristine electrodes and b. laser-patterned electrodes with dimensions ranging from 100 μm - 250 μm and c. 100 μm - 700 μm. In these experiments, the charge rate was kept at 0.1C for the 0.1C cycle and 0.2C for the 0.2C, 0.5C, 1C, and 2C discharge rates. Panel d. illustrates the discharge rate capacities deduced from Supplementary Figures S3-5a, S3-5b, and S3-5c, which are all normalized based on the capacities initially attained at a 0.1C discharge rate

Supplementary

Figure S3-6.....45

Electrochemical performance of pristine and laser-patterned 6 mAh/cm² Comparison of Discharge Rate Capability for Pristine and Laser-Patterned Electrodes. The figure shows discharge rate capability tests for a. pristine and laser-patterned electrodes with dimensions of b. 50 μm - 700 μm and c. 100 μm - 700 μm. For these tests, the charge rate was fixed at 0.1C for the 0.1C cycle and 0.2C for the 0.2C, 0.5C, 1C and 2C discharge rates. d. shows the discharge rate capacities derived from Supplementary Figures. S3-6a, S3-6b and S3-6c, normalized relative to the capacities obtained at a discharge rate of 0.1C.

Supplementary

Figure S3-7.....46

Electrochemical performance of pristine and laser-patterned 4.8 mAh/cm² Discharge rate capability tests for a. pristine, and laser patterned b. 30 μm – 700 μm c. 30 μm – 250 μm electrode samples through which the charge rate was fixed 0.2C for discharges rates of 0.2C, 0.5C, 1C and 2C. d. Discharge rate capacities obtained in Supplementary Figures S3-7a, S3-7b and S3-7c were normalized based on the capacities obtained at 0.2C

Supplementary

Figure S3-8.47

Electrochemical performance of pristine and laser-patterned 4.8 mAh/cm² Discharge Rate Capabilities of Pristine and Laser-Patterned Electrodes. This figure shows discharge rate measurements for a. pristine, b. laser-patterned 50 m - 100 m, and c. laser-patterned 50 m - 900 m electrode samples. Throughout these experiments, the charge rate remained constant at 0.2C regardless of the discharge rate: 0.2C, 0.5C, 1C, or 2C. d. Shows the discharge rate capacities derived from Supplementary Figures S3-8a, S3-8b, and S3-8c, which are all normalized based on the discharge rate capacities initially obtained at 0.2C.

Supplementary

Figure S3-9.48

Effect of laser-patterning on tortuosity on the channel size and the channel spacing on 6 mAh/cm² laser patterned electrodes Normalized Nyquist plot for laser-patterned channels with fixed channel size a. 30 μm or b. 100 μm.

Supplementary

Figure S3-10.48

Evaluation of the Effect of Laser-Patterning on Electrolyte Absorption and Average Lithium Concentration. The immersion tests in a 1M LiPF₆ EC:DEC (V:V = 1:1) solution illustrate the rate of electrolyte impregnation into laser-patterned electrodes with different channel spacings. COMSOL simulations show the differences in electrolyte impregnation for pristine and laser-patterned electrodes with different channel spacing and a fixed channel diameter of b. 30 μm and c. 50 μm. As a function of channel diameter and channel spacing, plot d shows the time required to reach an average concentration of 90% of the maximum concentration in the lower electrode layer. The percentage of volume removed by laser patterning is shown in Supplementary Figure S3-10e.

Supplementary

Figure S3-11.49

Effects of laser patterning on electrodes of different thicknesses and homogeneous porosities a. Illustration of a laser-patterned hexagonal array electrode with a homogeneous total porosity of 14% throughout the electrode, in which the top and bottom layers away from and closer to the aluminum current collector have the uniform porosity. Normalized effective diffusivity contour plots for b. 60 μm and c. 80 μm thick electrodes based on the steady-state electrolyte concentration gradient across the laser-patterned hexagonal array electrode.

Figure 4.1	Material characterization of channel formation and morphology within a graphite electrode with a capacity of 4.8 mAh/cm ² graphite electrodes. a. X-ray diffraction of the electrode before and after laser patterning (50 μm - 100 μm), demonstrating the absence of deleterious structural changes regardless of residual laser heat. b. Scanning electron microscopy (SEM) images show some non-uniform surface coloration, which may be due to heating caused during laser patterning c. Optical cross sectional image of a 30 μm - 100 μm laser-patterned electrode showing the formation of tapered channels.....	53
Figure 4.2	Figure 4. Effect of laser patterning on tortuosity and diffusivity as a function of channel spacing on 4.8 mAh/cm ² graphite electrode. The normalized Nyquist plot obtained for a. different laser-patterned channel sizes with channel size set to 50 μm. and b. Table of McMullin numbers derived by linearly fitting the impedance of symmetric cells.....	54
Figure 4.3	Effect of laser patterning on tortuosity and diffusivity as a function of channel spacing 6 mAh/cm ² silicon blended graphite electrode. The normalized Nyquist plot obtained for a. different laser-patterned channel sizes with channel size set to 50 μm.....	56
Figure 4.4	Evaluation of the effect of laser patterning on electrolyte absorption of 4.8 mAh/cm ² graphite electrode. Electrode immersion measurements reveal the rate of electrolyte impregnation into laser-patterned electrodes with varying channel spacing with channel size fixed to a.50 μm and b.30 μm during the first 300 seconds after immersion in 1M LiPF ₆ EC:DEC (V:V = 1:1) solution.....	57
Figure 4.5.	Electrochemical performance comparison of pristine and laser-patterned electrodes with capacities of 6 mAh/cm ² silicon blended graphite electrodes. Charge rate capability tests for a. pristine and laser-patterned b. 30 μm – 100 μm and c. 50 μm – 100 μm. The discharge rate was held constant at 0.1C for the 0.1C cycle and 0.2C for the 0.2C, 0.5, 1C and charge rate cycles. d. The charge rate capacities shown in Figures 4.5a, 4.5b and 4.5c were normalized based on the capacities obtained at 0.1C.....	58
Figure 4.6.	Electrochemical performance comparison of pristine and laser-patterned electrodes with capacities of 4.8 mAh/cm ² graphite electrodes. Charge rate capability tests for a. pristine and laser-patterned b. 30 μm – 100 μm and c. 50 μm – 100 μm. The discharge rate was held constant at 0.1C for the 0.1C cycle and 0.2C for the 0.2C, 0.5, 1C and charge rate cycles. d. The charge rate capacities shown in Figures 4.6a, 4.6b and 4.6c were normalized based on the capacities obtained at 0.1C.....	59

Supplementary.....62

Figure S4-1. Electrochemical performance comparison of pristine and laser-patterned electrodes with capacities of 6 mAh/cm² silicon blended graphite electrodes. Charge rate capability tests for a. pristine and laser-patterned b. 50 μm – 100 μm and c. 50 μm – 450 μm. The discharge rate was held constant at 0.1C for the 0.1C cycle and 0.2C for the 0.2C, 0.5, 1C and charge rate cycles. d. The charge rate capacities shown in Supplementary Figures S4-1a, S4-1b, and S4-1c were normalized based on the capacities obtained at 0.1C.

Supplementary.....63

Figure S4-2. Electrochemical performance comparison of pristine and laser-patterned electrodes with capacities of 6 mAh/cm² silicon blended graphite electrodes. Charge rate capability tests for a. pristine and laser-patterned b. 50 μm – 100 μm and c. 50 μm – 450 μm. The discharge rate was held constant at 0.1C for the 0.1C cycle and 0.2C for the 0.2C, 0.5, 1C and charge rate cycles. d. The charge rate capacities shown in Supplementary Figures S4-2a, S4-2b and S4-2c were normalized based on the capacities obtained at 0.1C.

Supplementary.....63

Figure S4-3 Evaluation of the effect of laser patterning on electrolyte absorption. Electrode immersion measurements reveal the rate of electrolyte impregnation into laser-patterned electrodes with varying channel size with channel spacing fixed to a. 700 μm and b. channel size fixed to 100 μm with varying spacing during the first 300 seconds after immersion in 1M LiPF₆ EC:DEC (V:V = 1:1) solution.

Figure 5.1 Schematic of the electrode patterning process using a hexagonal array of micro-pillars on a silicon wafer template with a hexagonal pattern. The process uses the stamping template to create an array of indentations or holes in fully densified, high stress graphite anodes in a matter of seconds.....**68**

Figure 5.2 SEM images of the hexagonal array in top view, the micropillars in side view, a single micropillar in side view, and the top view of micropillar channels fabricated on a graphite electrode with 100 μm and 900 μm channel size and spacing.....**70**

Figure 5.3 Charge curves of graphite anode at different C-rates a. before and b. after stamping using micropillar-based silicon wafer template for patterning hexagonal array patterns on thick and dense graphite electrodes. The effect of the hexagonal array patterning using the micropillar-based silicon wafer template on the c. specific and d. normalized charge capacities is further elucidated by comparative bar graphs.....**71**

Figure 5.4

Illustrates a. the average voltage at different C-rates before and after patterning with hexagonal arrays. b. An immersion test performed both before and after patterning to demonstrate the effect of micropillar patterning. C. An impedance measurement of the symmetrical cell is performed to derive the McMullin number both before and after patterning on the thick and dense graphite anode electrodes. MN is the McMullin number. The voltage profile of the d. pre-stamped and e. post-stamped 4.8 mAh/cm² graphite electrodes at 0.5C spanning from the 1st to the 50th cycle in the potential range of 0.01 ~ 1.6V (vs. Li/Li+) is shown. f. The cycling performance of the pre- and post-stamped graphite electrodes at 0.5C for 50 cycles following the initial 2 cycles at 0.1C and 2 cycles at 0.2C is shown. Each 0.5C charge cycle was followed by a slower 0.2C charge.....**73**

LIST OF SYMBOLS AND ABBREVIATIONS

EDX	Energy dispersive X-ray spectroscopy
EIS	Electrochemical impedance spectroscopy
EV	Electric vehicles
F	Faraday's constant
Li	Lithium
Li ⁺	Lithium-ion
LIB	Lithium-ion battery
NCA	Lithium nickel cobalt aluminum oxide
NCM	Lithium nickel cobalt manganese oxide
NMP	N-methyl-2-pyrrolidone
PVDF	Polyvinylidene fluoride
SEM	Scanning electron microscope
XRD	X-ray diffraction
Z	Impedance

SUMMARY

Lithium-ion batteries (LIBs), a critical component of EVs and ESSs, have been instrumental in the advancement of portable electronic devices. Although conventional LIB materials offer good energy and power densities, performance limitations necessitate further enhancement. Enhanced mass loading and areal capacity of up to 5 - 7 mAh/cm² are necessary to maintain volumetric capacity and rapid charge-discharge capabilities while obtaining higher volumetric and gravimetric energy densities. Though reduced porosity (20%), larger and denser electrodes with higher areal capacities impede lithium-ion transport, leading to worse rate performance, especially at high charge rates.

To address these issues, the study looked at the trade-off between electrochemical performance and the loss of laser patterning material in thick and dense high-nickel NCA, graphite, and silicon-blended graphite anodes that are commercially available. Even with sparse spacing of 450 μm , these electrodes' straight, tapered channels were laser-patterned, which reduced electrode tortuosity and sped up ion diffusion while greatly outperforming pristine electrodes in terms of rate performance.

The study also discovered that thick layers on large area cathodes reduce battery rate performance and ion transport kinetics. Nevertheless, the introduction of conical and tapered channels via laser patterning and micropillar-based patterning overcame this restriction, decreasing the average ion transport distance and improving electrolyte impregnation, thereby enabling greater utilization of thick and dense cathodes and anodes for superior lithium-ion batteries. This enhanced ion access to the electrode particles at high C-rates in thick and dense NCA cathodes. The work meticulously evaluated the trade-off between capacity retention due to fast ion movement and mass loss due to laser patterning using laser and micropillar based channel patterning with channel size (15 ~ 100 μm) and spacing (100 ~ 900 μm). Even with

large channel hole spacings and little active mass losses, there were appreciable rate increases of up to 3~4 times at high (dis)charge rates of 1C and 2C.

This extensive study deepened the understanding of the interactions between electrochemical performance, tortuosity, and electrolyte wetting and provided a new avenue for redesigning automotive Li-ion battery electrodes to increase power and energy densities for more affordable, longer-range, and fast-charging EVs.

CHAPTER 1. INTRODUCTION

1.1 Background on the need for lithium-ion battery research

Since the advent of the Industrial Revolution, energy has served as the bedrock of human civilization. Generations have exploited fossil fuels, leading to a global economy deeply entrenched in oil dependence. Despite escalating environmental concerns, the trend showed only a mere slow transition, with many developing nations poised to transition into “fossil fuel economies”, implying an inevitable surge in global fossil fuel consumption while the developed nations are slow to accelerate the transition away from the fossil fuel economy. This unabated fossil fuels over just a few generations over a couple hundred years has subjected our planet and mankind to the twin perils of unprecedented climate change and CO₂ emissions^{1,2}.

In response to the growing concern and awareness of environmental issues, gradual efforts have been made to move away from fossil fuels in order to curb our dependence on them and to reduce toxic air pollutants, especially in densely populated urban centers as many countries move toward banning sales of internal combustion engine^{3,4}. Among the many energy storage systems that have been developed, lithium-ion batteries have emerged as a compelling candidate over the past three decades, lithium-ion batteries have emerged as a completing candidate. Their potential as an energy storage system has received considerable attention and has been widely used in consumer electronics and now in electric vehicles, contributed to the much-needed shift toward sustainable energy solutions^{5,6}.

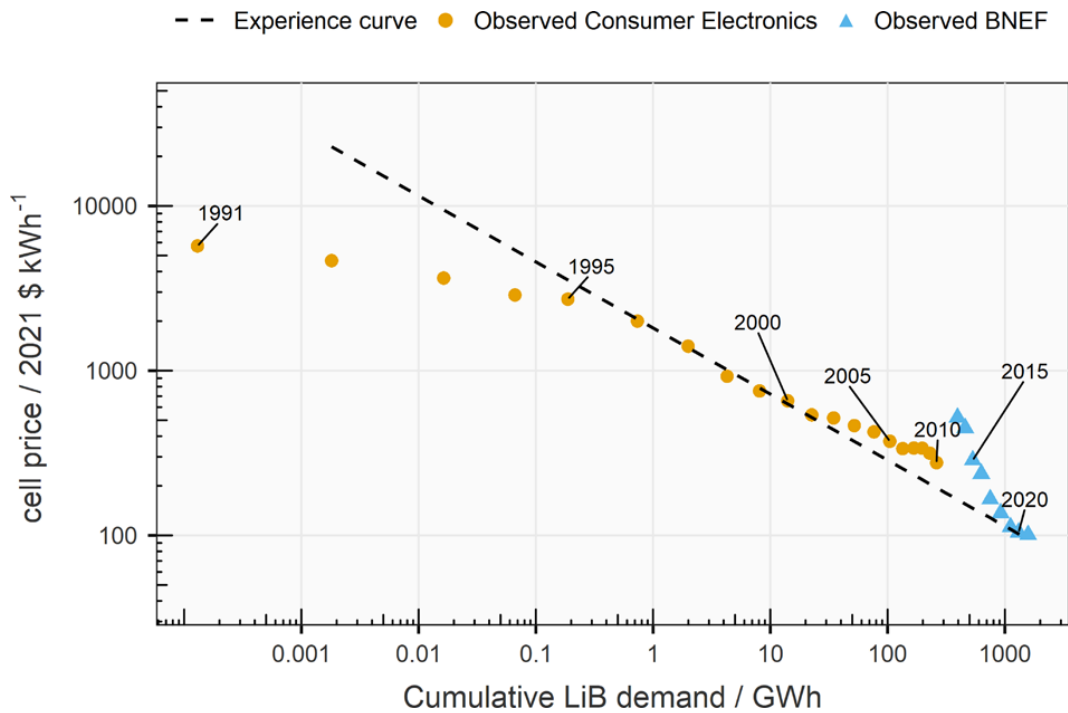


Figure 1.1 Observed cell prices from 1991 to 2021⁷ (Reproduced with permission from Ref. 7)

Renewable energy production, particularly from wind and solar, is at an all-time high and is expected to double by 2040⁸. However, their widespread adoption is hampered by the intermittent nature of renewable energy sources such as solar and wind energy as well as geographic limitations, necessitating advances in energy storage and grid integration^{9,10}. The price of lithium-ion batteries has dropped significantly over the past three decades from \$5000 /kWh to \$127 /kWh from their initial commercialization to 2022, indicating a 25% price drop with each doubling of the cumulative volume of battery cells used^{7,11}. This ongoing trend highlights the decreasing cost of LIBs as their adoption and production continue and expected to increase in the coming years.

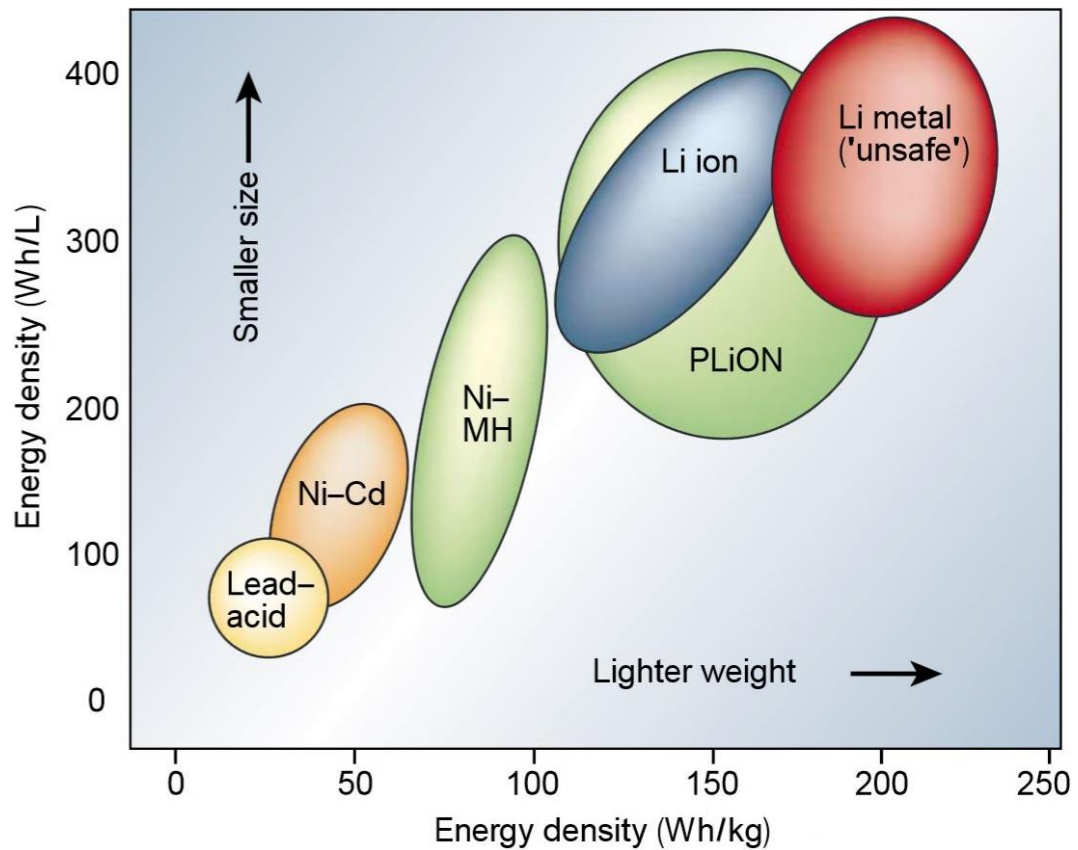


Figure 1.2 Energy density comparison among different energy storage systems¹²
 (Reproduced with permission from Ref. 12)

In 1991, Sony introduced LIBs with a LiCoO_2 cathode and a soft carbon anode with a specific energy density of 80 Wh/kg and an energy density of 200 Wh/L, while another type with a hard carbon anode had a slightly higher specific energy of 120 Wh/kg and an energy density of 295 Wh/L^{13,14}. The energy density of a battery is primarily determined by voltage and specific capacity, both of which are influenced by the electrode materials, more specifically the redox potential of the material used. Extensive research has been conducted to improve electrode materials, including activities such as tuning chemical composition, doping, surface modification, optimizing particle size, and more recently, increasing the carbon-to-oxygen ratio and

the amount of nickel (Ni) in cathode materials such as lithium nickel cobalt aluminum oxide (NCA) and lithium nickel cobalt manganese oxide (NCM). These advancements aim to reduce reliance on expensive and rare cobalt (Co), increase capacity without compromising cathode integrity or requiring higher charging voltages that can impact the calendar and cycle life of automotive LIB cells, among other benefits^{15,16}.

1.2 Theoretical background of a lithium-ion battery

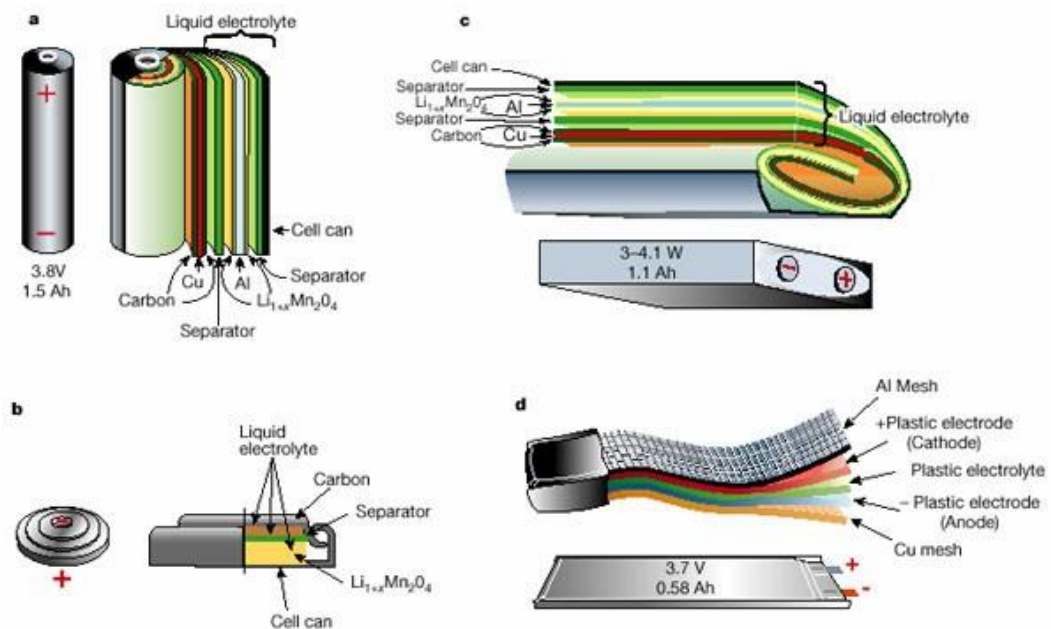


Figure 1.3 Example of battery components and different form factors¹²
(Reproduced with permission from Ref. 12)

A LIB consists of four basic components: cathode, anode, separator, electrolyte and two current collectors (aluminum and copper current collectors). The positive and negative electrodes consist of (electro)active material, conductive carbon for improved

electrical contact and polymer binder for cohesion among the other electrode components and structural integrity. These composites are typically placed in an organic solvent, n-methyl-2-pyrrolidone (NMP), and thoroughly mixed to disperse the conductive carbon well enough to form electrical networks and homogeneous mixture with polymer binder and conductive carbon. The electrolyte in a battery consists of soluble salts and an organic solvent and plays a key role in facilitating the efficient transfer of Li^+ ions between the cathode and anode. This essential mechanism ensures the smooth and reliable operation of the battery by allowing the controlled flow of electrical current during the charging and discharging processes^{10,17}.

Once the electrode slurry is prepared, the resulting slurry is casted onto a current collector foil followed by a drying process. For the positive electrode, active materials are typically LiCoO_2 , LiFePO_4 and (high nickel) layered lithium nickel cobalt aluminum oxide (NCA) and lithium nickel cobalt manganese oxide (NCM) cathode materials and they are casted as a thin film on aluminum foil, while graphite or silicon blended graphite are used as active materials for the anode and casted onto a copper foil with different binders which will be discussed later.

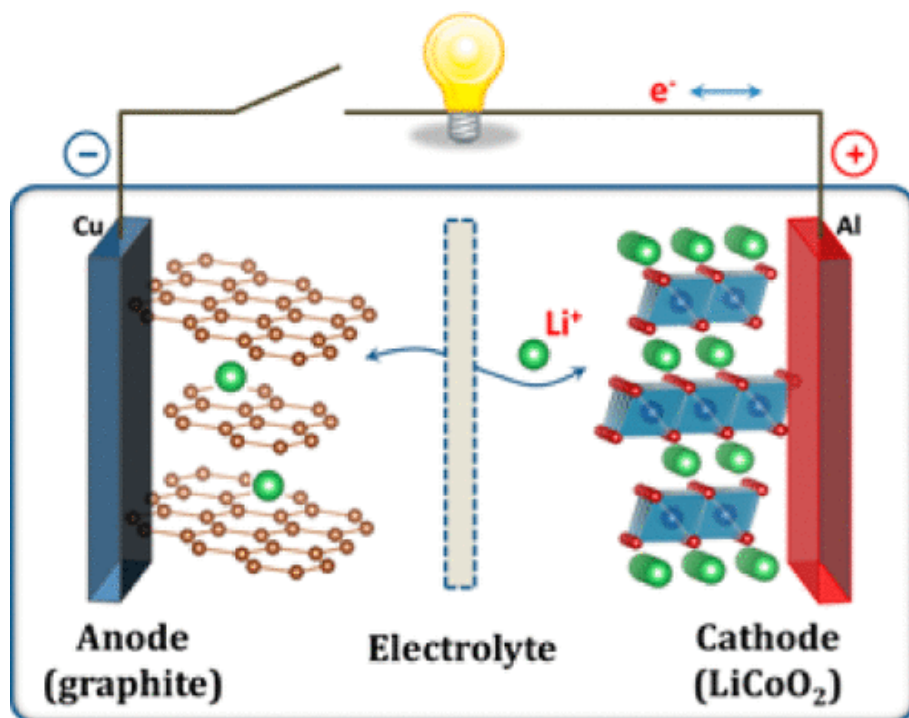
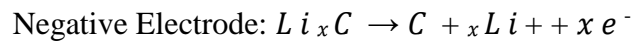
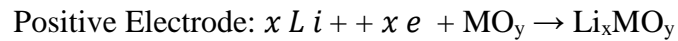


Figure 1.4 Lithium ion battery schematic illustration¹⁷ (Reproduced with permission from Ref. 17)

Lithium-ion batteries work by converting chemical energy from reversible oxidation-reduction (redox) reactions into electric energy by moving electrons through an external circuit and providing electric current between current collectors. The redox reactions occur reversibly. Following the “rocking chair” principle, Li⁺ ions transfer between the cathode and anode through the electrolyte, while both the resulting electron flow occurs through the external circuit. That is, the electric current flows from one current collector to the other through the external circuit. The separator acts as a barrier between the cathode and anodes to block the flow of electrons and to prevent short-circuiting, instead functioning as a medium for the transfer of charged ions. During charging, Li⁺ ions move from cathode to anode, while during discharging, they move from the anode to the cathode.

The following are examples of reactions that occur at the positive and negative electrodes during the discharge process. Note that these reactions are reversed during the charge process.



Theoretical capacity of battery electrode is defined by the thermodynamic property of the material and refers to the amount of charge that could be stored or generated. It can be calculated using the following equation:

$$\text{Theoretical Capacity} = \frac{nF}{3.6 \times M}$$

where the variable ‘n’ represents the number of moles of Li that participate in the electrochemical reaction, ‘F’ stands for Faraday’s constant and ‘M’ is the molecular weight of the material. It's important to clarify that the weight referred to here does not include the weight of other components of the battery electrode, such as the current collector, conductive additives, and binder etc.

The potential of a battery is dictated by the chemical potential difference between cathode and anode materials as a result choosing the correct set of materials is critical for the overall performance of the battery. Commercial LIBs work primarily via an intercalation (lithiation) and deintercalation (delithiation) process which involve the

reversible insertion and de-insertion of lithium ions into the cathode and anode electrode while releasing electrons to an external circuit back and forth.

The cell voltage is determined by the Gibbs free energy of the electrochemical reaction and is the sum of electrical potential and chemical potential as follows.

$$G = \mu_i + z_i F \mathcal{E}$$

where μ_i , z_i , F and \mathcal{E} are the chemical potential of the species, the effective charge on lithium, the Faraday constant and electrical potential, respectively.

The open circuit voltage a LIB cell is controlled by the chemical potential difference between cathode and anode materials without current flow and is determined by the following relationship.

$$V = \frac{\mu_{Li}^{cathode} - \mu_{Li}^{anode}}{ze}$$

where $\mu_{Li}^{cathode}$, μ_{Li}^{anode} , z and e are the chemical potentials of cathode and anode, lithium ion charge and electron charge, respectively.

On the contrary, the nominal voltage refers to the voltage at which the circuit is closed, i.e. it takes into account the internal resistance and polarization, which contribute to a slightly lower voltage compared to the equilibrium voltage, also known as the open circuit voltage, during discharge. During charge, the nominal voltage is greater than the open circuit voltage. The voltage difference between the equilibrium

voltage and the nominal voltage becomes more apparent at high current densities. The voltage difference is attributed to the three different polarizations: ohmic, activation and concentration polarizations.

Polarization in the context of batteries refers to a condition where the voltage of the battery increases during charging or decreases during discharging due to various internal resistances and reactions. It essentially represents a loss of energy and is a key factor limiting the rate performance of a battery. Polarization increases with the rate of charge or discharge. The two main types of polarization are ohmic polarization and concentration polarization. Ohmic polarization refers to losses due to the resistance of battery components such as the electrolyte and electrodes, while concentration polarization is caused by the limited rate of chemical reactions occurring in the battery.

Efforts have been made to improve rate performance by modifying the components of the battery. These modifications include reducing the size of the active particles in the electrodes, which can increase the specific surface area and reduce the charge transfer resistance; reducing the thickness of the electrodes, which can reduce both ohmic resistance and concentration polarization; increasing the porosity of the electrodes, which can reduce concentration polarization by improving electrolyte contact and reducing tortuosity; and optimizing electrolyte concentration and viscosity, which can also reduce concentration polarization¹⁸.

1.3 Developments in Lithium-Ion Battery Research

1.3.1 Cathode materials

Lithium Cobalt Oxide (LCO) cathodes face several challenges. They deliver a capacity of less than 180 mAh/g, below their theoretical maximum of 274 mAh/g^{13,19}. They also have a high cobalt content, a scarce and expensive material, making them less affordable and scalable, particularly for applications such as electric vehicles (EVs). To make matters worse, most of the cobalt is sourced from regions where unethical practices are used to mine²⁰. LCO batteries also have poor thermal stability, leading to thermal runaway and limiting the operating voltage to 4.1V or less, with a usable capacity of about 140 mAh/g²¹. High-voltage LCO batteries can reach up to 4.4 V and offer improved capacities, but face problems such as phase transitions and excessive side reactions with the electrolyte that cause gradual particle pulverization. However, these advantages come with their own challenges: irreversible bulk and surface phase transitions from O3 hexagonal to hybridized O1-O3 hexagonal phase and excessive side reactions with the electrolyte, leading to gradual particle pulverization²².

As an effort to reduce the amount of Co, previous research push the nickel content increase the reversible specific capacity from 160 mAh/g of NMC111 ($\text{LiNi}_{1/3}\text{Mn}_{1/3}\text{Co}_{1/3}\text{O}_2$) attained when charging to 4.2V vs. Li/Li^+ to approximately 200 mAh/g of NMC811 ($\text{LiNi}_{0.85}\text{Mn}_{0.1}\text{Co}_{0.1}\text{O}_2$) attained at 4.25-4.3V vs. Li/Li^+ using the two electron transfer from $\text{Ni}^{2+}/\text{Ni}^{4+}$ ²³⁻²⁵. The trend has been similar with NCA and

NCA811 demonstrating reversible volumetric capacity of close to 700 mAh/cm³ at the electrode level²⁵. The so-called Ni rich layered oxide cathode materials (NMC and NCA with nickel content of $\geq 80\%$) still rely on a small content of aluminum (Al), cobalt (Co) and other metals for structural, thermal and cycle stabilities which are vital for EV applications^{8,26}. In more recent cathode designs, a gradually changing Co concentration (from small or no near the core to high near the surface) and gradually changing Ni concentration (from very high near the core to greatly reduced near the surface) have been successfully utilized²⁷⁻²⁹. In an alternative way, the use of single crystalline cathode particles prevents microcracking phenomena of polycrystalline cathode materials (often aggravated by electrolyte decomposition, gas evolution and dissolution of transition metals from grain boundaries) for improved cell stability²¹, although often at the expense of higher synthesis costs, reduced rate performance and lower attainable energy density. Currently, Li-excess disordered cathode materials are under extensive research to further increase energy density via oxygen anionic redox reaction (changing oxidation state for some of the oxygen anions from -2 to -1), although insufficient stability of such system remains an issue³⁰⁻³³.

1.3.2 Anode materials

As a counterpart electrode for high energy and high capacity battery electrode for cell level, anode material development is also crucial. While there has been much progress in commercialization for a new generation of Ni-rich cathode materials, commercial LIBs initially used coke (160-220 mAh/g), an amorphous carbon by-

product, as an anode material. However, the shift to graphite anodes occurred due to their advantages, including a higher theoretical specific capacity (372 mAh/g), low de-lithiation potential, and high electrical conductivity. Graphite, an intercalation-type material, can accommodate a maximum of one Li-ion per six carbon atoms (LiC_6). As such, graphite has been widely used as a commercially viable anode material for the past three decades. However, its relatively smaller capacity (372mAh/g) to silicon counterparts and irreversible capacity losses from the SEI formation hinders improving energy density of LIBs to satisfy the EV demands to reach price parity with combustion-engine vehicles. Thus, silicon (Si) is considered as a very promising contender to replace the conventional graphite anode due to its extremely high theoretical capacities of ~ 3579 mAh/g at room temperature (corresponding to the formation of $\text{Li}_{15}\text{Si}_4$ during lithiation/LIB charge), reasonably low operating potential ($\sim 0.25\text{V}$ vs. Li/Li^+ vs. around 0.15V for graphite operating voltage) and material abundance^{34,35}. However, its huge volume expansion during lithiation and contraction during de-lithiation brings upon detrimental effects on electrical contact between active materials, binder and current collector, cracking of active material and large irreversible capacity losses due to SEI instabilities³⁶. While some of the companies are developing unique composite anodes with high (40-80 wt. %) Si content and small volume changes at the composite particle level, the most common industrial solution in 2020 was to mix small amounts (commonly $< 5\text{wt.}\%$) of Si-based material (commonly silicon oxide, SiO_x) with conventional graphite anode to increase specific capacity up to around 400-430 mAh/g. Larger amounts of SiO_x induces undesirably fast degradation and too large irreversible capacity losses in the first cycle as Li irreversibly bonds with O of the SiO_x ³⁷.

CHAPTER 2

Motivation and Research Objectives

2.1. Electrode design considerations

In the quest to increase the energy density of lithium-ion batteries (LIBs), increasing the thickness of the electrodes is a promising strategy. However, this step presents challenges as thicker and denser electrodes can lead to limited electrolyte infiltration, reduced battery material utilization, and reduced electrochemical performance, especially in high-rate applications^{26,38,39}. Thicker and denser electrodes, while potentially beneficial in increasing energy density, can result in reduced battery material utilization, limited electrolyte infiltration, and reduced electrochemical performance^{40,41}. This is due to the high tortuosity of the pore network and the elongated ion diffusion pathways, which are significant barriers to efficient ion movement. These limitations are particularly significant in high rate applications.

Therefore, the process of designing high energy density thick electrodes that are low in porosity and tortuosity and thicker than 80 μm becomes a complex challenge. This is especially true given current practices where critical parameters such as particle size distribution, porosity and pore size are often ignored or relegated to secondary importance⁴²⁻⁴⁴.

The impact of particle size and distribution in the overall performance of a battery cannot be overstated. These factors play a critical role in determining the solid state diffusion length of Li^+ ions, electrode surface area and porosity. Smaller particles, due to their shorter solid state diffusion length, are advantageous as they can reduce overpotentials and allow for faster C-rate operation. However, these advantages come

with a significant drawback: the increased surface area of smaller particles can lead to a higher proportion of passivation layers, such as the solid electrolyte interphase (SEI). On the other hand, larger particles have longer solid state diffusion lengths but higher tap density, resulting in higher volumetric energy density. A combination of these particles, with a narrow-to-medium particle size distribution (PSD) and low polydispersity index (PDI), can result in better packing and improved electrolyte access, improving battery performance. Over time, the SEI can cause an irreversible loss of capacity, undermining the initial benefits of smaller particles⁴⁵.

Particle size and shape distribution can result in heterogeneity of reaction activity within the particle, which can lead to electrode cracking and capacity loss. Lithiation - the process of Li^+ ions being inserted into the lattice of a material - occurs at different rates for particles of varying sizes⁴⁶. Small particles tend to undergo lithiation in a faster and more uniform manner than their larger counterparts, leading to lower surface concentrations of lithium ions. It is challenging to achieve uniform particle dispersion in electrodes, which can cause heterogeneous reactions and compromise charge distribution, especially when the active components are located in the carbon/binder domain (CBD)⁴⁷⁻⁴⁹. Inconsistent pore networks, non-uniform pore distribution, and increased ion transport resistance can lead to a mismatch between ionic and electronic conductivity, which reduces battery performance and lifetime.

The porosity and tortuosity of an electrode have a significant effect on its ionic conductivity. Although high porosity improves mass transport, it can also lead to mechanical weakness and cracking or delamination. Meanwhile, high tortuosity reduces ion and electron transit while increasing polarization. The use of techniques such as high-temperature sintering, laser patterning, and density gradient electrodes has improved ion transport in thick electrodes by creating low-tortuosity pore architectures

and balancing porosity and tortuosity⁵⁰⁻⁵⁵.

2.2 Motivation behind thick and dense electrodes and their limitations

In a LIB cell two-sided anodes, separator and two-sided cathodes are either stacked (sandwiched) together in many layers or rolled to form a cell. The volume fraction of the separator and current collector foils (Cu foil for the anode and Al foil for the anode) commonly consume at least 15 vol. % (sometimes as much as 30 vol. %) of the overall stack (roll) made with conventional (relatively thin, 50-70 μm /each side electrodes), which consequently reduces the LIB volumetric and gravimetric capacities. From this point of view, thick electrode design eradicates the need for multiple layers of components and increases the weight percentage of active electrode layers in the cells to over 90 vol.% and even higher when electrode porosity is low. Consequently, the significantly higher volumetric and gravimetric energy densities of LIBs reduce the battery weight and increase the driving mileage of EVs. In addition, thicker electrodes open more opportunities for cost reduction of over 10% (the actual value depends on the electrode design)²⁶.

Unfortunately, increase in traditional cathode thickness more than $\sim 80 \mu\text{m}$ while simultaneously retaining high density and low electrode porosity (e.g., $< 30\text{-}35\%$) is extremely challenging. It typically leads to significant reduction in cell rate capability, energy efficiency and stability. Based on the previous research, it has been reported that thick electrode electrodes with high percentage of active and low porosity suffer from large internal resistance, which consist of electric resistance (R_e), electrolyte bulk resistance (R_{sol}) and ionic resistance (R_{ion}) components^{56,57}.

Thick electrodes suffer from large and highly tortuous paths of electrons and

ions, which plays as a significant obstacle to attain fast rate of LIB charge and discharge. Sluggish electronic and ionic conduction brings upon internal resistance and potential drop at high current density, limits the effective use of voltage window, causes undesired lithium plating, and detrimentally affects the cell energy density and stability. From the electrode engineering perspective, the battery performance limiting factors prevents economic and full use of thick battery electrodes and hinders homogeneous electrochemical reactions under fast charging and discharging.

To determine the more dominant factors in tackling the key issues of low porosity (dense) thick electrodes, Orikasa et al. used combination of cross section mapping of absorption energy and four-point probe to investigate the effective and ionic conductivities in LiFePO_4 composite electrodes with high porosity and low porosity. This study demonstrated that the ionic conduction is a more dominant factor in improving rate performance of low porosity composite battery electrodes⁵⁷. Ogihara et al. conducted an impedance measurement study using symmetric cell platform under low temperature to prevent any kinetic hindrance from high temperature⁵⁸. In the study, the symmetric cell impedance measurement was conducted under non-faradaic environment to determine the resistance value at high frequency region and conclude that ionic resistance in high frequency region is affected by the percentage of porosity, carbon content and thickness. In short, ionic conduction is one of the most important and dominating factor that determines and affects the tortuosity of the electrode, thereby, leading to critical capacity fading.

To quantify the impact of electrode pore tortuosity, previous research often used electrochemical techniques and (3D X-ray) tomography^{59,60}. In electrochemical approach, transmission line model analysis (TLM) is used to quantify ionic resistance of a porous electrode by blocking the faradaic charge transfer reactions and leaving

only ionic and high frequency resistance (HFR) values ($Z = \frac{R_{ion}}{3} + R_{HFR}$) from the impedance measurements^{61,62}.

McMullin number and tortuosity (see Eq. 2 for their relationship) can be quantified from electrochemical measurements. If one successfully reduces their values in dense and thick LIB electrodes, significant reduction in R_{ion} and overall impedance Z could be attained. Indeed, the shorter ionic transport path significantly reduces ion diffusion time (characteristic time for ion diffusion is proportional to the square of the path length) and consequently improve rate performance of thick battery electrodes under higher current densities.

$$N_M = \frac{R_{ion} \times A \times \kappa}{d} = \frac{\tau}{\varepsilon}$$

[where N_m =McMullin number, R_{ion} = ionic resistance obtained from the TLM measurement, A =cross-sectional area, κ = conductivity of electrolyte, d = thickness, ε is the porosity, τ is the tortuosity]

To lower tortuosity of the dense and thick electrodes, laser patterning has been previously proposed. For example, Kim et al. used highly ordered and hierarchical laser patterning to reduce electrode tortuosity and demonstrated that a laser patterned graphite electrode had improvement in capacity retention at higher current density and reduced ohmic drop at higher C-rates. However, this work used highly porous (50%) electrodes, which are not commercially viable due to low volumetric capacity and low volumetric energy density.

2.3 Research design and objectives

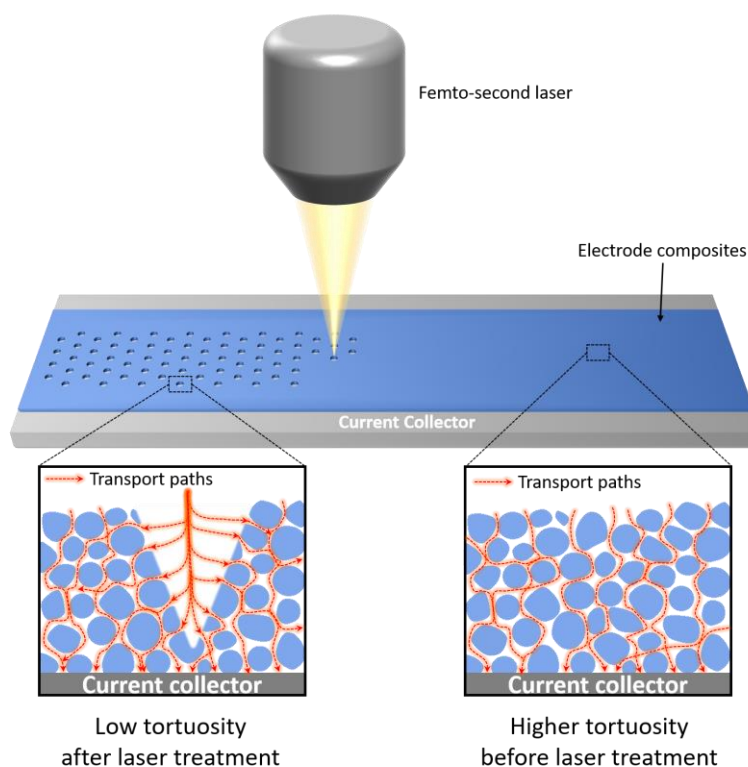


Figure 2.1 Schematic of the femto-second laser treatment of thick battery electrode.

Figure 2.1 shows schematic of the concept proposed for the systematic studies of electrode rate performance using a WS-FLEX IR femtosecond laser to micro-machine hexagonal array of holes with different diameter and spacing. The characteristic time for ion diffusion is proportional to the square of the average diffusion path, which is influenced by both the thickness of the electrode and its tortuosity. Therefore, increasing electrode thickness from 100 to 200 μm may induce up to 4 times reduction in cell rate performance (provided, the rate is mostly limited by ion transport and that other limitations may be neglected, in the simplistic case). Introduction of straight channels offers potential to partially overcome discussed above challenges at the expense of small additional porosity (2-10%).

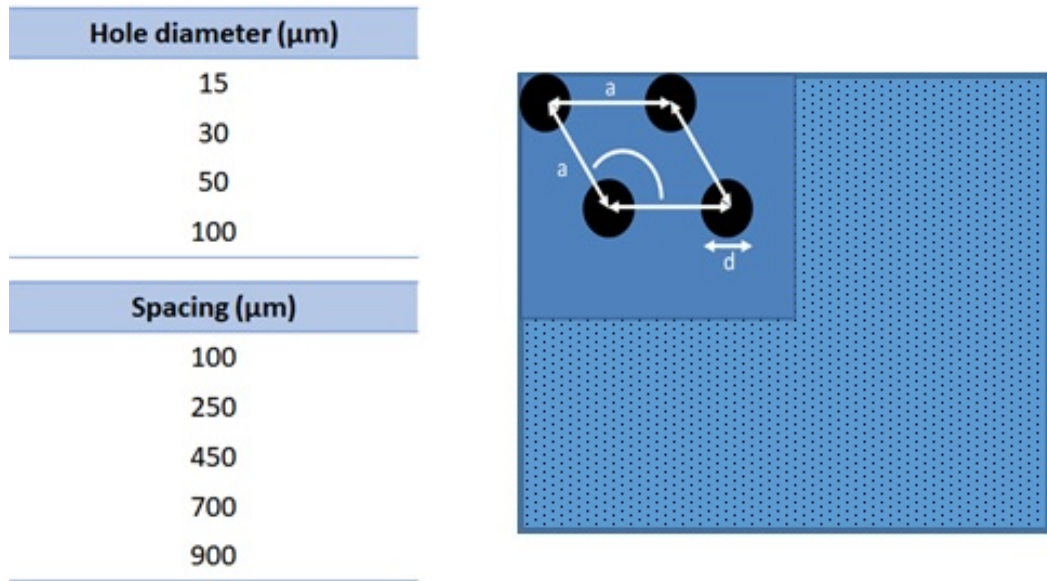


Figure 2.2 Experimental design of hexagonal array pattern with different hole diameter and spacing.

Figure 1 shows schematic of the concept proposed for the systematic studies of electrode rate performance using WS-FLEX IR femtosecond laser to laser make hexagonal array of holes with different diameter and spacing. Characteristic ion diffusion time is proportional to the square of the average diffusion path, which is dependent on both the electrode thickness and tortuosity. Therefore, increasing electrode thickness from 100 to 200 μm may induce up to 4 times reduction in cell rate performance (provided, the rate is mostly limited by ion transport and that other limitations may be neglected, in the simplistic case). Introduction of straight channels offers potential to partially overcome discussed above challenges at the expense of small additional porosity (2-10%). The technique should allow us to control the spacing and the size of the pore channels as shown in Figure 2. If needed, other pore patterning techniques (e.g., mechanical indentation into the electrode) may be investigated at later

stages of the project.

Table 1 shows the theoretical mass losses after perforation calculated for each laser perforation assuming that the holes are perfectly cylindrical and conical. From a practical standpoint, conical holes may be preferred considering smaller mass loss of electrode material. The difference in mass losses after laser perforation is more noticeable for larger hole with smaller spacing. There is a broad range of hole sizes and spacing that retained 97-99%+ of the capacity for cylindrical holes which was promising from practical point of view (e.g., electrode mass loss and capacity).

Diameter (μm)	Spacing (μm)	Cylindrical Holes	Conical Holes
		% Density for full depth	% Density for full depth
15	450	99.9	99.97
15	100	98.0	99.32
30	450	99.6	99.87
30	700	99.8	99.94
30	900	99.9	99.97
30	250	98.7	99.56
30	150	96.4	98.79
30	100	91.8	97.28
40	100	85.5	95.17
50	100	77.3	92.45
50	150	89.9	96.64
50	250	96.4	98.79
50	450	98.9	99.63
50	700	99.5	99.85
50	900	99.7	99.91
100	900	98.9	99.63

Table 2.1 Theoretical mass loss of each hexagonal array pattern with different shaped holes

CHAPTER 3

SPARSELY LASER-PATTERNED TAPERED CHANNELS IN THICK AND DENSE HIGH-NICKEL NCA ELECTRODE

Doyoub Kim, Alexandre Magasinski, Yueyi Sun, Baolin Wang, Aashray Narla, Seung-Hun Lee, Hana Yoo, Samik Jhulki, Ah-Young Song, Jinho Hah, Ting Zhu, Alexander Alexeev, Gleb Yushin. This chapter is reproduction of “High Energy and Power Densities in Thick and Dense Li-Ion Battery Electrodes via Sparsely Laser-Patterned Conical Channels”, *submitted*.

3.1 Introduction

To meet the growing demand for high energy density and power density in LIB for EV battery (LIB) for electric vehicle (EV) applications (particularly in EVs offering long driving range of 400-700 miles), production of lower cost, higher energy density cells is critically needed. The use of thick (80–100 μm) and dense electrodes with high areal capacity ($\geq 6 \text{ mAh/cm}^2$) is considered a promising solution to increase cell energy and simultaneously reduce production costs^{26,63,64}. This is because such designs reduce the volume and mass fractions of many inactive components (separators, aluminum (Al) and copper (Cu) current collectors, etc.). The EV battery cost reductions come both directly from savings on such materials in cells and indirectly from increased cell volumetric and gravimetric energy densities and thus reduced number of cells and smaller and cheaper battery (including smaller and cheaper battery safety/management system) needed in an EV to attain the same range^{8,65,66}.

The highest performance cathodes currently in use or under the final stages of development for EV LIBs include nickel (Ni)-rich lithium nickel manganese cobalt oxides (NMC, such as NMC811 or $\text{LiNi}_{0.8}\text{Mn}_{0.1}\text{Co}_{0.1}\text{O}_2$ with practical capacity of up to

~190 mAh/g) and Ni-rich lithium nickel cobalt aluminum oxides (NCA, such as $\text{LiNi}_{0.8}\text{Co}_{0.15}\text{Al}_{0.05}\text{O}_2$ with practical capacity of up to ~200 mAh/g)⁶⁷⁻⁷⁰. To maximize the volumetric cathode capacity, such cathodes are typically densified to retain <20% porosity. When such electrodes are produced with high areal capacity loadings, their rate performance become sluggish due to the ion diffusion time being proportional to the square of the diffusion path, which is proportional to the electrode thickness and the tortuosity⁷¹. If the tortuosity were thickness-independent, then increase in cathode areal loading by 40% would increase diffusion time by ~2x, thus dramatically reducing rate performance during both charge and discharge. This, in turn, may also jeopardize LIB cycle life or safety because slow ion transport may induce uneven de-lithiation of the cathode or (in case of similarly slow ion transport within the anode) inhomogeneous lithiation and localized Li plating on the anode, particularly at high current densities or at lower temperatures⁴⁷. In addition, the LIB energy and electrode capacity harvested at fast rates would also be limited, thus reducing practically attainable EV range. If the tortuosity increases with cathode thickness, such undesirable effects would be further enhanced.

In this study, we present novel results showing how thick lithium nickel cobalt aluminum oxide (NCA) cathodes with conical and tapered channels significantly improve capacity retention at higher current densities. Surprisingly, our research shows that significant rate performance improvements can be achieved even when the laser-drilled pore channels are widely spaced, exceeding the electrode thickness by several orders of magnitude.

Further investigation shows that commercially manufactured calendered electrodes have a denser layer near the electrode surface, which hinders ion movement and electrolyte wetting during lithium-ion battery (LIB) operation. However, the

incorporation of pore channels successfully overcomes these limitations, facilitating ion transport and leading to a significant capacity enhancement at discharge rates of 1C-2C. Notably, this enhancement requires only a small reduction, ranging from 0.37% to 0.03%, in the theoretically achievable volumetric capacity for the 450 μm hexagonal pattern of conical pores.

3.2 Experimental Methods

3.2.1 Preparation of electrode

This study is conducted with high Ni (> 80) containing NCA electrode supplied by Samsung SDI Co Ltd. Two types of electrodes were explored with aerial capacities of 4.8 mAh/cm² and 6 mAh/cm², respectively, and both have the active material > 95 wt.%. WS-FLEX IR femtosecond laser is used with different variations of laser frequency, power speed and repetitions to optimize and obtain the most controllable hexagonal array pattern with minimal unwanted damage to the electrodes. The laser micro-machine is used to prepare AUTOCAD design to make hexagonal array patterns appropriately.

3.2.2 Material Characterizations

The Panalytical XPert PRO Alpha-1 XRD was used for all XRD experiments to examine the structural change and impurity formation before and after the laser micromachining. Data was collected for the 2θ range of 15–60°. Cross-section sample was first immersed in epoxy and left for up to one day to harden. The laser-micromachined NCA is individually mounted using two-part epoxy resin and hardener mixture in 1:0.23 (wt./wt.) ratio. These samples were ground using a series of different

SiC papers up to 4000 grits and polished on PoliCloth (Buehler, USA) using 1 μm diamond suspension followed by polishing on Buehler VibroMet 2 using 0.05 μm colloidal silica suspension. During grinding and polishing steps, samples were thoroughly washed with acetone and rinsed with isopropanol (IPA) to remove residue and stains. The polished samples were then characterized using Leica digital microscope to obtain cross-sectioned images. Scanning electron microscopy (SEM) SU8010 was used to observe the channel size and spacing after laser micro-machining from the top using a standard SEM stub while SU8230 was used to examine the cross-sections of the electrode to determine the shape of the channels and elemental distribution of the cross-sections using the EDS capability. 3D confocal microscopy was used to examine the pore shape of laser micromachined electrodes with different channel size and spacing variations. 3D pictures of electrodes and templates were captured with Olympus LEXT OLS 4000 laser confocal microscope (Olympus Scientific Solutions Americas Inc., USA) with a fixed laser wavelength of 405 nm and using magnification ranges: $\times 108 - \times 17,000$. The microscope was also used to measure the geometrical properties (measurement accuracy ca. ± 1 nm) of the hexagonal array of channels. For each sample, three measurements were carried out at different positions of the electrode and the average data were used for all calculations. Immersion test was conducted to observe electrolyte impregnation before and after laser patterned electrodes with different channel size and spacing. The experiments were conducted using pre-cut strips of 15 mm width using a Sigma 700/701 tensiometer (Biolin Scientific AB, Beijing, CPR), and a 1.0 M solution of lithium hexafluorophosphate (LiPF_6) in EC / DEC = 50/50 (v/v) (Battery, Millipore Sigma, USA) was used as a wetting liquid. The measurement process is systematically controlled by a computer, and the mass of the electrolyte adsorbed by the electrode is recorded over time. A weight

versus time (m-t) curve was constructed, from which the wettability of the electrode with the electrolyte is calculated.

3.2.3 *Electrochemical Tests*

After one cycle of C/10 and C/5 rates, followed by each cycle with varying discharge rates (C/2, 1C, 2C, 3C) is conducted while the charge rate is fixed at C/5. In between each charge and discharge cycle, there is a 10-minute gap allowed for equilibration. To study the impedance and tortuosity of the electrodes, electrochemical impedance spectroscopy was performed at an open circuit potential after a preliminary rest period of 24 h after making the fresh half cells. Impedance data were collected in a galvanostatic mode, and the frequency range was selected from 100 kHz to 10 mHz taking 10 points per decade. The Nyquist plots were measured with the 10 mV amplitude of the AC voltage.

3.2.4 *Simulation methods*

We model Li-ion diffusion within a hexagonal electrode element of fixed height 80 μm and various side lengths 100 – 700 μm . Periodic boundary conditions are applied in horizontal directions. We construct modeled electrode element with a less porous top layer (porosity 8%) and a more porous bottom layer (porosity 15%) to match the experimental observed electrode configurations (Figure 2.1). We include top-down holes with diameters 10 – 50 μm on the four corners of modeled electrode element by setting porosity 100% for the holes. Transport of Li-ion within modeled electrode element is governed by $\partial(\epsilon_{p,i}c)/\partial t + \nabla \cdot [(-D_{Li+} \times \epsilon_{p,i}/\tau_{F,i})\nabla c] + u \cdot \nabla c = S$. Where c , $\epsilon_{p,i}$, $\tau_{F,i}$, D_{Li+} and S are the concentration of Li-ion, porosity and tortuosity of electrode layer material, Li-ion diffusion coefficient and source. Once we attach the top surface to a reservoir, Li-ions diffuse into modeled electrode element. We analyzed

the effect of hole sizes and patterns on Li-ion concentration and total Li-ion count within modeled electrode element over time.

A model is developed to consider the porous electrode structure with a periodic array of conical channels as shown in Figure 1. The electrode thickness L and the porosity of the porous electrode matrix (yellow part in Figure 1a) ε_b are fixed since they are unchanged before and after laser treatment. The remaining parameters include the top-hole diameter d , spacing s and bottom-hole diameter d' determine the energy density and areal capacity of the electrode. Based on Fick's first law of diffusion, $J = D_{\text{eff}} \nabla C$, we know that when the flux J is fixed, the effective diffusivity D_{eff} is inversely proportional to the steady state concentration drop across the electrode ΔC . Therefore, the rate of ion transport indicated by D_{eff} can be evaluated by computing ΔC . The steady state concentration drop across the electrode is calculated from the modified porous electrode model^{72,73}. In our calculations, the classic Bruggeman relationship between tortuosity τ and porosity ε , $\tau = \varepsilon^{-0.5}$, is employed. From the cross-section view of the electrode in Figure 4g (right diagram), there are two limiting paths for ion transport from point A (next to separator) to point B (next to current collector). One path (red arrow) is through the porous electrode matrix alone and parallel to the channel; the other one (green arrow) is first along the channel and then laterally across the porous electrode matrix. An effective concentration drop ΔC_{eff} is computed by the addition rule of parallel resistors from ΔC through the two paths. The contours for the effective diffusivity D_{eff} (inverse of ΔC_{eff}) is shown in Figure 4g as a function of the porosity of the channels ε_c and hole-diameter d for $\varepsilon_b=0.14$ and $L=80 \mu\text{m}$. The effective diffusivity D_{eff} is normalized by that before laser treatment (electrode without channels) such that this value indicates the increase of D_{eff} after laser treatment. The porosity of the channels ε_c r

represents a measure of loss of active materials due to laser treatment. It is related to s by equation $\epsilon_c = (d^2 + d'^2 + d \cdot d') / 3s^2$ for a specific set of d and d' by which the shape of the conical channels is determined. In the computation of Fig. 4g, the slope of the surface is assumed to be fixed which means the difference between d and d' is constant.

3.3 Results and discussion

Introduction of straight pore channels into the cathode can potentially increase C-rate performance^{39,74}. If the gains in accessible capacity due to a faster ion transport in thick, high-loading electrodes during sufficiently fast charge or discharge could be made substantially higher than the loss of capacity due to mass loss during the formation of straight pore channels, additional efforts and costs associated with such channel formation may be justified. Previous research demonstrated the positive impact on rate enabled by the use of laser sources to introduce patterned channels within NMC electrodes⁷⁵. However, such work studied highly porous (up to 50%) cathodes, which are not commercially viable due to their low volumetric capacity and energy density⁷⁶⁻⁷⁸. As such, there remains an open question whether formation of straight pore channels occupying much smaller volume fractions (e.g., 1-5 vol. %) may be suitable for meaningful improvements in the cathode rate performance.

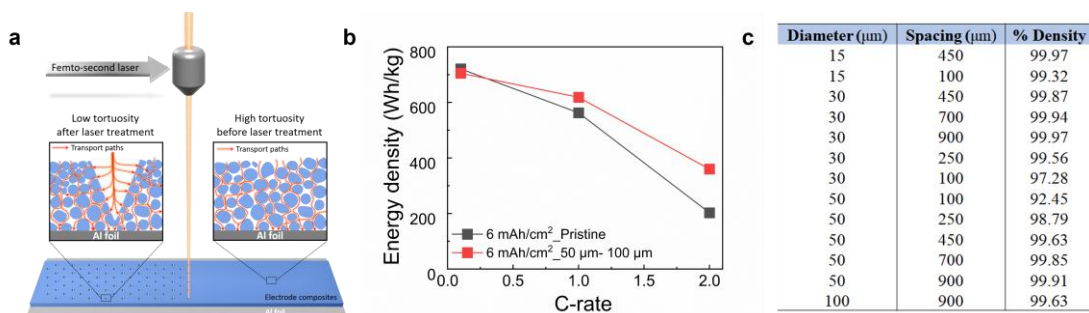


Figure 3.1 Illustration of laser patterning and its effects. **a.** The schematic diagram shows the role of laser treatment in reducing tortuosity and improving electrolyte wetting and ion transport, thereby enhancing the electrochemical rate performance of thick and dense battery electrodes. **b.** The graph shows the achievable energy density at high current density when using thick and dense electrodes laser-patterned with a dense laser pattern. **c.** The table provides examples of electrode material losses for various patterns, demonstrating that minimal electrode losses (0.1% to 8%) can be achieved with appropriate pattern architecture.

In this chapter, we report on a first systematic study to elucidate the impacts of laser patterned channels of different thicknesses, width and spacing on achievable capacities at different C-rates in cells comprising dense and thick NCA cathodes with areal capacity up to ~ 6 mAh/cm². We unambiguously demonstrate that this approach may significantly improve both power density and accessible energy density in EV LIB cells.

Figure 3.1a shows schematic of the laser-patterning process, where a regular array of conically shaped pore channels is introduced into an electrode. This process is rather fast in industrial settings it can be done much faster: roll-to-roll before or after calendaring using an array of lasers, an array of optical fibers⁷⁹ or fiber Bragg gratings⁸⁰ carrying the laser signal from a single more powerful source. Figure 3.1b shows examples of the electrode material losses for selected patterns, demonstrating that very small electrode losses may be realized with proper pattern engineering (0.03-7.55 vol.%).

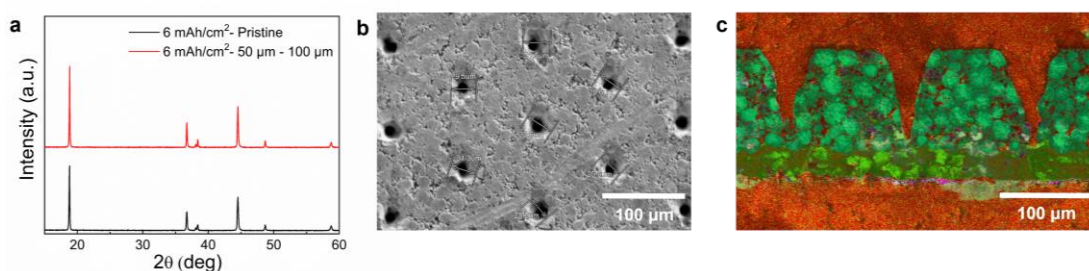


Figure 3.2 Material characterization of channel formation and morphology within a high-nickel NCA electrode with a capacity of 6 mAh/cm². **a.** X-ray diffraction of the electrode before and after laser patterning, demonstrating the absence of deleterious structural changes regardless of residual laser heat. The representative top-view SEM images show the effective formation of **b.** hexagonal array channel patterns extending from 30 μm to 100 μm. **c.** SEM cross section of a 30 μm – 100 μm laser-patterned electrode showing the formation of tapered channels. Energy dispersive X-ray spectroscopy (EDS) mapping of the laser-patterned electrode provides an elemental map, where red and purple represent elements introduced during epoxy preparation for the cross-sectional imaging, and light green, sky blue, dark green, and orange are from the high-nickel NCA electrode and aluminum current collector, respectively. Supplementary Figure S3-1 provides additional information on the elements. Note that 30 μm – 100 μm represents the upper diameter of the channel and, correspondingly, the distance between the closest channels.

We patterned two commercially produced thick and dense high nickel NCA cathodes (electrode density of ~3.7 g/cc, thickness of ~80 and ~95 μm and areal capacities of 4.8 and 6 mAh/cm², respectively) using a fs-laser source to create channels of controllable size (width and depth) and spacing between them (see Experimental section for additional details). We observed the color change (darkening) of the material around the laser cut channels induced by the residual heat from laser patterning. However, the laser patterning process does not cause any undesirable changes in the overall phase of the bulk NCA cathodes, as determined from the identical powder X-ray diffraction (XRD) profiles of pristine and laser-patterned electrodes (Figure 3.2a), suggesting a possible local binder carbonization.

The representative top-view scanning electron microscopy (SEM) images reveal the

presence of uniformly distributed hexagonal array of holes on the top surface (see example patterns with the surface diameter of $\sim 30\ \mu\text{m}$ and spacing $\sim 100\ \mu\text{m}$ in Figure 3.2b). The cross-sectional optical images of the laser-patterned electrode demonstrated in Supplementary Figure S3-2 reveal that the created channels are conical and tapered. The conical shape of the channels likely originates from the local heat distribution under the laser beam and the resulting material losses, where the electrode becomes the hottest on the top surface, while the heat is dissipated more readily near the metallic aluminum (Al) current collector. Figure 3.2c shows examples of such channels spaced $\sim 100\ \mu\text{m}$ from each other and extending from the top of the cathode surface down to the Al foil. Such channels should facilitate ion transport throughout the entire electrode bulk. Cross-sectional energy-dispersive X-ray spectroscopy (EDS) mapping confirm the presence of all the expected elements (Supplementary Figure S3-1). From a practical standpoint, conical holes may be preferred over cylindrical holes of same diameter from the consideration of smaller electrode mass loss in the case of the former, while still providing an effective way for less tortuous path for ion transport.

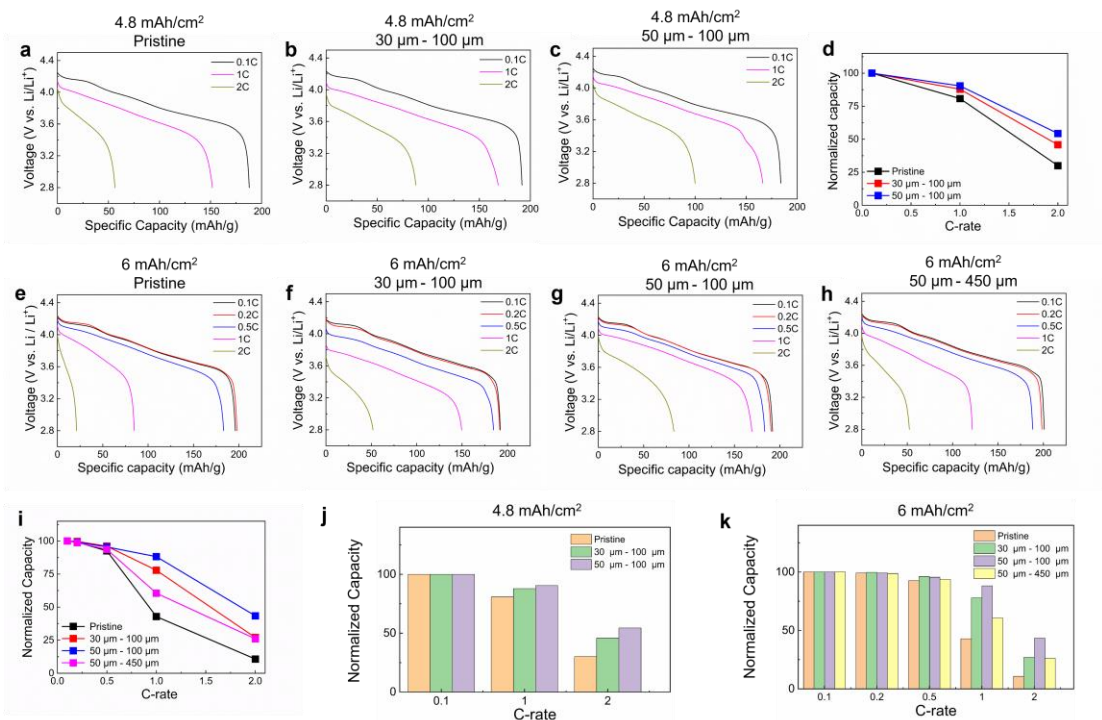


Figure 3.3. Electrochemical performance comparison of pristine and laser-patterned electrodes with capacities of 4.8 mAh/cm² and 6 mAh/cm². Discharge rate capability tests for a. pristine and laser-patterned b. 30 μm – 100 μm and c. 50 μm – 100 μm, for the 4.8 mAh/cm² electrode samples. The charge rate was held constant at 0.1C for the 0.1C cycle and 0.2C for the 1C and 2C discharge rate cycles. d. The discharge rate capacities shown in Figures 3.a, 3.b and 3.c were normalized based on the capacities obtained at 0.1C. For the 6 mAh/cm² electrodes, additional discharge rate capability experiments were conducted for e. pristine and laser patterned f. 30 μm – 100 μm, g. 50 μm – 100 μm, and h. 50 μm – 450 μm. For these experiments, the charge rate was 0.1C for the 0.1C cycle and 0.2C for the 0.2C, 0.5C, 1C, and 2C cycles. i. The discharge rate capacities in Figures 3.a, 3.b, and 3.c have been normalized based on the capacities secured at 0.1C. j. Figures 3.d and k. Figure 3.i are bar graphs of the normalized capacities derived from j. Figure 3.d k. Figure 3.i.

Electrochemical tests were conducted in half cells of 2032-type using pristine or patterned NCA cathodes, Li metal foil anode, 1M LiPF₆ EC:DEC (V:V = 1:1) electrolyte and Celgard 2400 separator (see experimental section for cell fabrication details) to reveal the impact of straight pore channels on the electrochemical performance, and to compare and quantify the discharge rate capabilities of the pristine and laser-patterned samples with different channel spacings and sizes. Compared to the pristine electrode, the laser-patterned cathodes resulted in noticeably improved rate performance, showing higher rate capacities at current densities in the range from 1C to 3C (Figure 3.3) likely due to faster ion transport throughout the bulk electrode. To effectively compare the values for the electrodes of areal capacity of 4.8 mAh/cm², the discharge capacities obtained from each half cells for high C-rates were normalized by the discharge capacity obtained at a 0.1C (slow) rate (Figure 3.3d). The results clearly show that beyond 0.5C, the channels begin to noticeably influence the achievable capacity, as we had hoped to attain. Furthermore, for the pore channel spaced at ~100 μm the rate performance was particularly impressive, exceeding those from other samples by quite some margin, especially at faster C-rates. A similar but even stronger trend was also observed with higher capacity loading of ~6 mAh/cm² (cathodes thickness ~95 μm). For such a high loading automotive cathode, the roles of channels for the capacity improvement at high C rate (1C and 2C) is much more evident (Figure 3.3i and Figure 3.3k). Notably, that the normalized capacity difference between pristine and 100 μm-spacing laser patterned samples increases from approximately two to four times as the C-rate increases from 1C to 2C for the largest pores (Figures 3.3j and 3.3k).

To further examine the roles of the channels and minimize active material loss, we fabricated an electrode sample with larger separation between the hexagonal array of holes (~450 μm). Despite the spacing between the holes exceeding the electrode

thickness, noticeable improvements were nonetheless obtained with such an electrode system exhibiting higher capacities (approximately 1.45 and 2.45 times, respectively) than that of the pristine sample at 1C and 2C (Figure 3.3i). They indicate that the electrode tortuosity is orientation-dependent, and that the ion transport is likely severely blocked at the denser or more torturous electrode top surface layer. In this case, much faster ion transport during the discharge (cathode lithiation) could be attained if the Li ions migrate throughout the electrode by initially propagating vertically through the ordered channels and then laterally through a less dense and less torturous electrode portion closer to the Al current collector foil. Indeed, our X-ray tomography measurements of the cathodes confirmed higher density of the top surface electrode layer (note that the Supplementary Figure S3-3 may under-estimate a fraction of the binder relative to the remaining pores since the active material has much higher density compared to the binder). The high resistivity of the top electrode channel also highlights the advantages of having the conical shape of the pore channels because a larger fraction of the more ionically resistive material is removed, while keeping the total pore volume small (note that the volume of a perfect straight cone is 1/3 of the volume of a cylinder with the same top diameter; volume of the convex cone is even smaller).

Interestingly, while reducing the top pore diameter from nominally $\sim 50\ \mu\text{m}$ to $\sim 30\ \mu\text{m}$ slightly reduced the rate performance, it still showed significant improvement exceeding that of the $\sim 450\ \mu\text{m}$ -spaced channel electrode at 1C and 2C and suggesting that closely spaced arrays of more narrow channels may enable faster ion transport pathways at high C-rates. This hints toward the importance of ion-transport pathways in both vertical and horizon directions; while vertical ion transport is clearly much faster through the formed pore channels, the kinetics of the overall ion transport may quickly become limited by horizontal ion transport ability if the pore spacing is too large and

exceed the electrode thickness substantially (Figure 3.3d and 3.3i). The ideal size and space distribution of the pore channels should thus depend on the distribution of the active material and binder throughout the dense calendered electrode and the resulting distributions of pore sizes and pores shapes (that are being filled with electrolyte during cell operation). For very uniform electrodes (with the top electrode portion having equal density to the bottom electrode portion) smaller and more narrowly spaced pore channels (with the spacing smaller than electrode thickness) may be beneficial. However, for commercially produced electrodes evidently having a denser top surface layer larger spacing (larger than the electrode thickness) may still be highly advantageous. Such electrode pattern is commonly easier and faster to make via laser-drilling. In addition, the total volume of the electrode removed by the laser may become substantially smaller (Figure 3.1c). We hypothesize that the undesirable dense surface layer may be formed by hot roller calendaring, which should make the binder near the top electrode surface hotter and thus softer and more deformable.

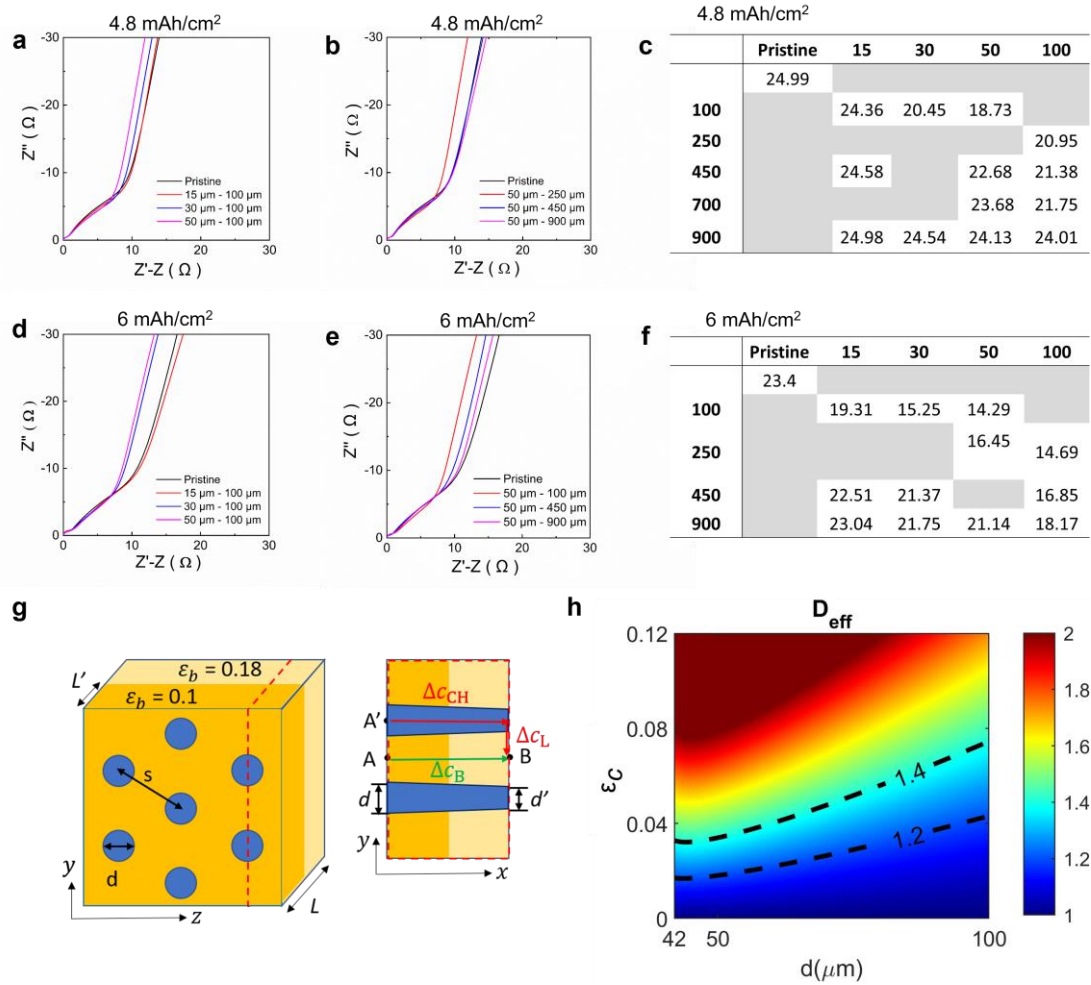


Figure 3.4 Effect of laser patterning on tortuosity and diffusivity as a function of channel size and channel spacing. The normalized Nyquist plot obtained for a. different laser-patterned channel sizes with channel spacing set to 100 μm and b. different channel sizes with channel spacing set to 4.8 mAh/cm². c. Table of McMullin numbers derived by linearly fitting the impedance of symmetric cells. The Nyquist plot obtained for d. Different laser-patterned channel sizes while channel spacing was set to 100 μm and e. Different channel spacing while channel size was fixed at 100 μm for a loading of 6 mAh/cm². f. Table of McMullin numbers derived from linear fitting of the impedance obtained from symmetric cells in Figures 4d and 4e. The laser treatment induces a periodic array of conical channels in a porous electrode matrix. g. Geometry of a laser-patterned hexagonal array electrode with conical channels of different porosity in the upper and lower halves of the electrode. The top corresponds to 10% porosity, while the bottom, closest to the Al foil, corresponds to 18% porosity, for a total porosity of 14% for the entire electrode (Supplementary Figure S3-3). h. Contour plot of the normalized effective diffusivity based on the steady-state decrease in electrolyte concentration across the laser-patterned hexagonal array electrode at a load of 6 mAh/cm² when the electrode thickness excluding the Al foil was fixed at 80 μm .

To elucidate the effect of laser patterning on tortuosity, McMullin numbers - which reflect the tortuosity factor of the electrodes - were derived based on the impedance tests conducted on symmetric cells in non-faradaic environment (Figure 3.4). The laser patterning contributes to the substantial reduction in McMullin number, both when the channel size increases and the channel spacing decreases, confirming less tortuous ion transport pathways for patterned electrodes. The 4.8 mAh/cm² electrode patterned with a very large spacing of 900 μm shows a very small difference in McMullin number, even for larger pore channels of ~100 μm (Figure 3.4c). As the spacing reduces to 450, 250 and 100 μm, the reduction in the McMullin number becomes more apparent (Figure 3.4c). With 50 μm conical channel electrodes, the McMullin number decreases from ~24.1 to ~18.7 when the spacing reduces from 900 μm down to 100 μm, which is substantially smaller than that of the pristine NCA electrode (~25) (Figure 3.4c). This trend becomes even stronger for the thicker and higher areal capacity 6 mAh/cm² electrodes, (Figure 3.4f) demonstrating that the rate limiting ion transport resistance in thick and dense electrode maybe directly linked to the reduction in electrode tortuosity. Somewhat to our surprise, slightly smaller McMullin number was obtained in thicker electrodes (Figure 3.4), which we explained by the later generation of the coating and calendaring technologies employed to produce such samples.

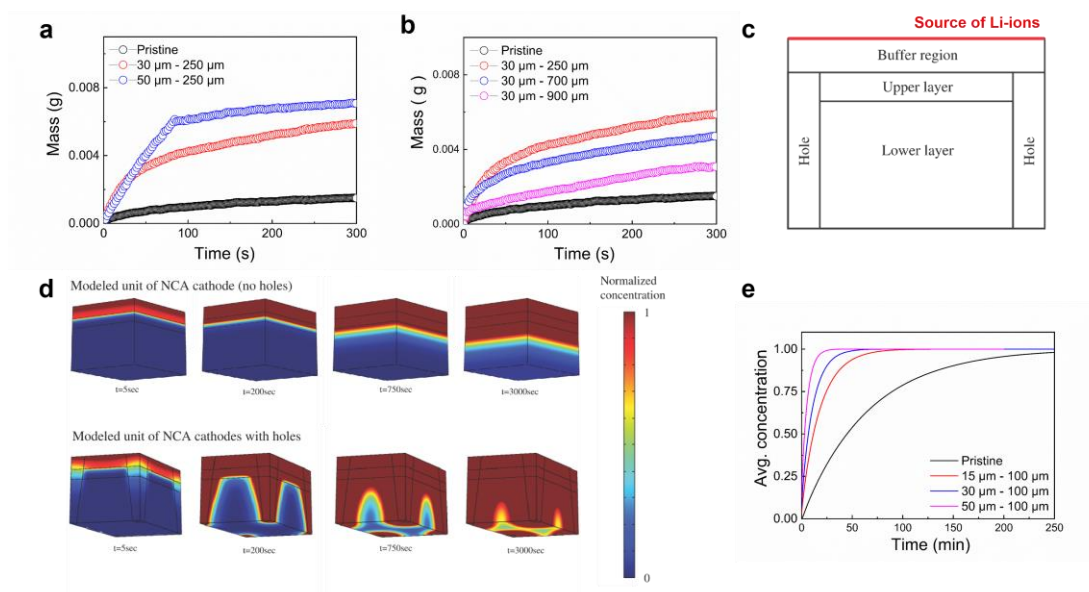


Figure 3.5 Evaluation of the effect of laser patterning on electrolyte absorption. Electrode immersion measurements reveal the rate of electrolyte impregnation into laser-patterned electrodes with varying a. channel diameters and b. channel spacing during the first 300 seconds after immersion in 1M LiPF₆ EC:DEC (V:V = 1:1) solution. c. Depicts the geometric representation of a single unit of NCA cathodes based on hole patterning, with each unit exhibiting periodic side boundaries. d. COMSOL simulations reveal that the presence of laser-patterned perforations enhances ion transport in the modeled electrode elements. The depicted unit has a side length of 100 μm and a height of 80 μm, and its openings have end diameters of 20 μm and 40 μm. The simulation result depicts the time necessary for the average electrolyte concentration to permeate pristine and laser-patterned electrodes.

Electrode immersion tests were also conducted to compare the electrolyte impregnation ability of the laser-patterned 4.8 mAh/cm² electrodes. Consistent with the trend observed for the McMullin numbers, the laser patterned electrodes underwent substantially faster electrolyte filling. However, the overall impact of laser patterning on the wetting rate was dramatically stronger than what we initially envisioned based on the rate performance (Figure 3.3) and tortuosity measurements (Figure 3.4). Indeed, the patterned electrodes were impregnated by a few times higher amount of electrolyte for a given amount of time (Figure 3.5a and Figure 3.5b). Also note that the electrodes with smaller channel spacing show significantly faster and larger electrolyte

impregnation (Figure 3.5a and Figure 3.5b), consistent with the electrochemical performance observed for them. Taken the trends in McMullin numbers and electrode immersion tests together, the laser patterned electrodes with larger channel size and small channel spacing significantly minimize tortuosity for ionic conduction and enhance electrolyte wetting.

We modeled Li-ion diffusion within a hexagonal electrode element of fixed electrode height (80 μm) and various channel diameters from 10 μm to 50 μm and spacings (100 – 700 μm) in an electrode with a denser top layer porosity of approximately 8% and a less dense layer that is closer to the Al foil with a porosity of approximately 15% to match the experimentally observed electrode in Supplementary Figure S3. The result shows that electrodes with patterned holes significantly reduce the time needed to reach a specified average Li-ion concentration as the pore channel diameter increases when the channel spacing is fixed to 100 μm (Figure 3.5d). The total ion count within a modeled electrode element with holes significantly exceeds those without holes until the discharging and charging time is so large such that the electrodes saturate. But having too many channels with large diameter within the modeled electrode element with small side length would reduce volumetric capacity. By removing more material leads to faster ion transportation, but one gets significantly diminishing returns after removing 8-10 vol%.

We developed a model matrix to consider the laser patterned electrode structure with a periodic hexagonal array of conical channels based on Figure 3.2c and Supplementary Figure S3-2, in order to enhance the understanding of how laser patterning with various channel sizes and spacings affects the decrease in McMullin number. Figure 3.4g depicts a model structure in which the electrode thickness L and

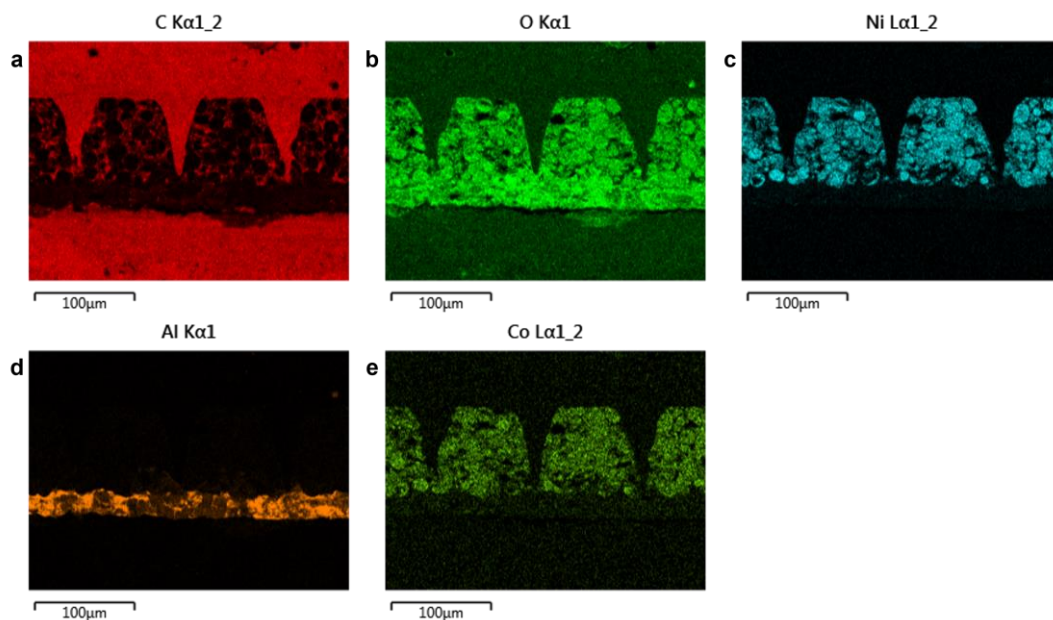
the porosity of the porous electrode matrix ϵ_p are fixed since they are unchanged before and after laser treatment. The remaining adjustable parameters are as follows: top hole-diameter d , spacing s and bottom hole-diameter d' (accounting for tapered conical channels), which collectively determine the energy density and areal capacity of the electrode. Contours for the effective diffusivity D_{eff} (see Methods) are shown in Figure 3.4h as a function of porosity resulting from the channels ϵ_c (due to the loss of active materials from laser patterning of a hexagonal array) and channel diameter d , for the case of a thick and dense 6 mAh/cm² electrode (with the thickness of ~80 μm excluding the Al foil). The higher the loss of electrode material the larger the channel diameter and smaller the channel spacing, as shown in Table 2.1. It is worth noting that the black dashed lines in Figure 4h indicate that the effective diffusivity D_{eff} increases from 1 to 1.2, 1.4 and higher even with losses of electrode materials slightly less than 2 wt.% ($\epsilon_c = 0.02$), 4wt.%, ($\epsilon_c = 0.04$) and higher, while the channel diameter is fixed to 50 μm from laser patterning. As the electrode material loss becomes closer to 8 wt.% corresponding to a channel spacing of 100 μm or less, D_{eff} increases from 1 to 1.6 or higher in a significant manner. This indicates the smaller channel spacing is desirable to achieve lower tortuosity, boost electrolyte impregnation (as shown in Figure 5b), and more importantly improve ion transport in thick and dense electrodes while tolerating some loss of electrode materials. Similarly, given that ϵ_c is slightly smaller than 0.04 in such a way that it is on the dashed line with a normalized effective diffusivity of 1.4, it would be decreased to the normalized effective diffusivity of 1.2 either by reducing electrode material loss (indicating a smaller channel spacing when the channel size is fixed to 50 μm) or by increasing the channel size while maintaining the same electrode material loss. This scenario corresponds to a design that aims to achieve the maximum rate of

ion transport for a tolerable loss of active materials.

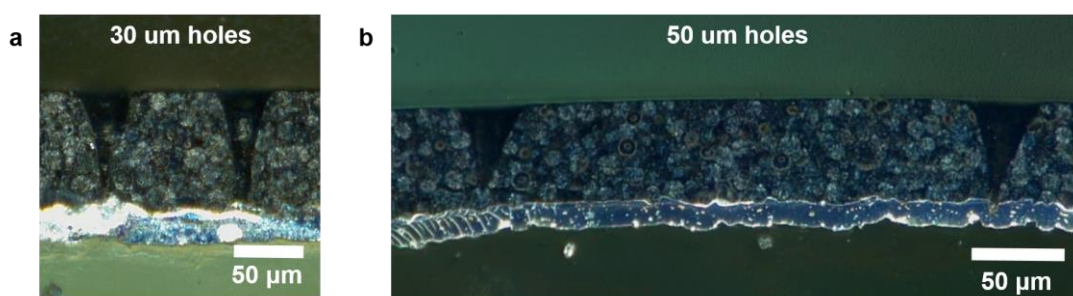
3.4 Conclusion

This work revealed that the formation of dense layer on the surface of high areal capacity loading automotive cathodes significantly reduces ion transport kinetics and Li-ion battery rate performance. Such a limitation, however, could be overcome successfully by introducing conical and tapered channels via laser patterning. Such channel holes shorten mean ion transport distance and improve electrolyte wetting. Facile vertical ion transport pathways through the straight channels followed by their horizontal transport were found to allow for much improved and homogeneous access of the ions to the electrode particles at high C-rates in thick and dense NCA cathodes. The trade-off between mass (volumetric capacity) loss due to laser patterning and gain in capacity retention due to fast ion transport was systematically analyzed via creation of channels of controlled size/volume and their spacing. Both hole size and their spacing are important for accessing high capacity at a fast C-rate, as the ion transport kinetics for laser patterned electrodes is largely determined by the horizontal ion transport kinetics. Even for channel hole spacings as large as 450 μm and mass losses of 0.37-0.03%, significant rate improvements could be attained. This systematic study combined both experimental observation and diffusion modeling to enhance our understanding of interdependence among electrochemical performance, tortuosity, and electrolyte wetting. The gained insights will provide a major thrust to redesigning automotive Li-ion battery electrodes to attain higher power and energy density at the cell level, so as to achieve cheaper, longer driving range EVs that retain fast charging capability.

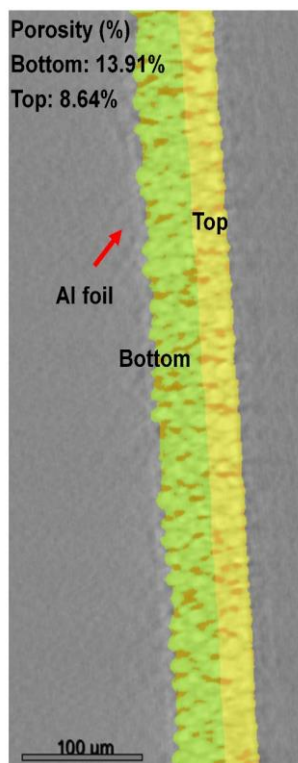
3.5 Supplementary Figures



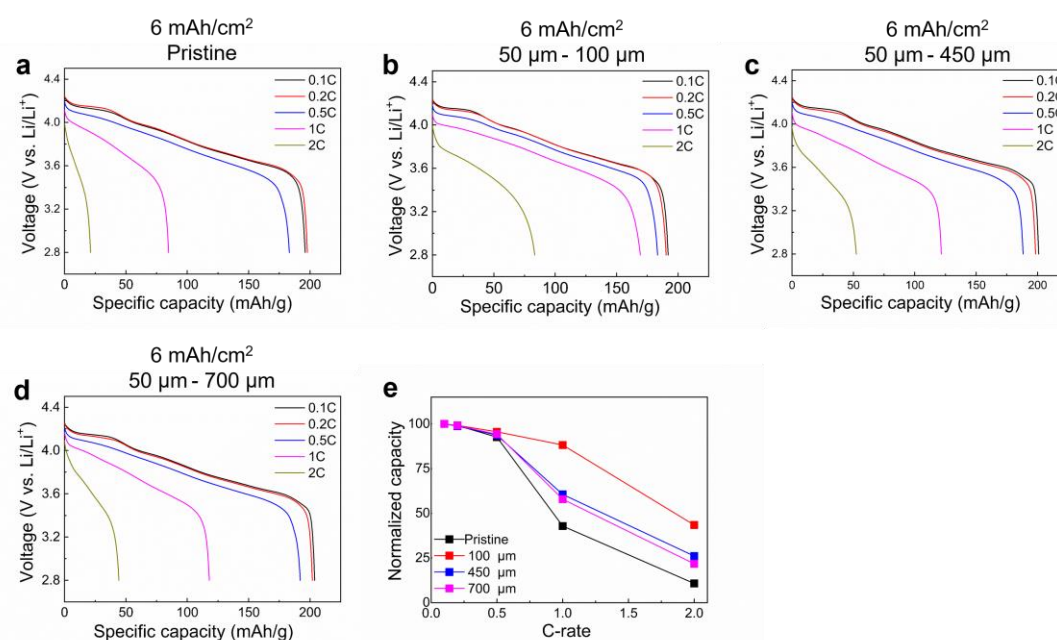
Supplementary Figure S3-1 The EDS of the cross-section of the laser patterned electrode with the conical-shaped channels shown in Figure 3.2d. The corresponding EDS elemental mapping of a. C b. O c. Ni d. Al e. Co.



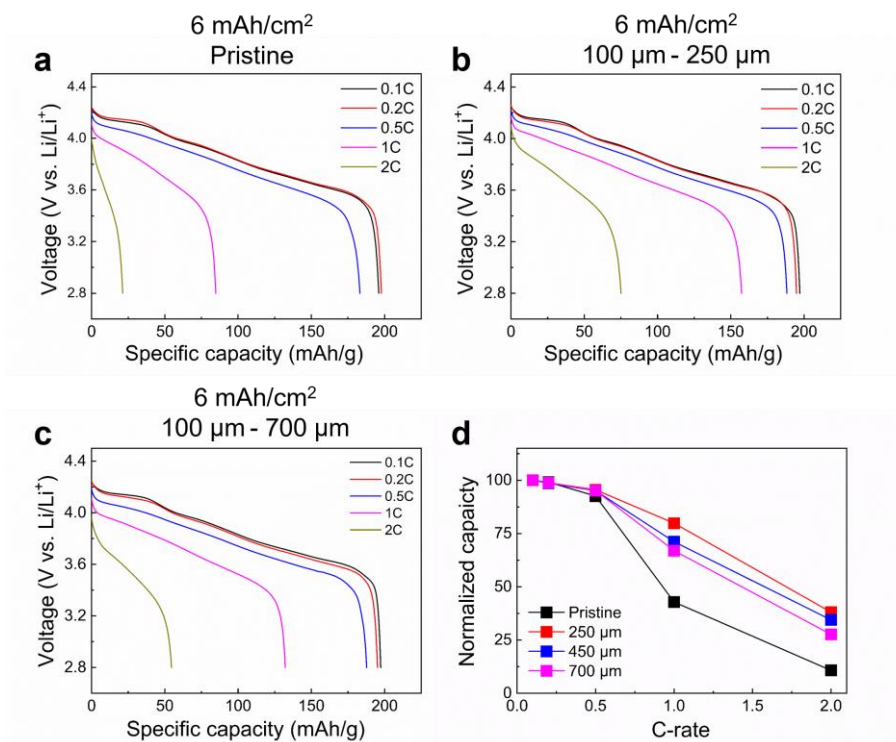
Supplementary Figure S3-2 Optical images of the cross-section of laser patterned 6 mAh/cm² electrodes with channel sizes of a. 30 μm and b. 50 μm in diameter with different spacings.



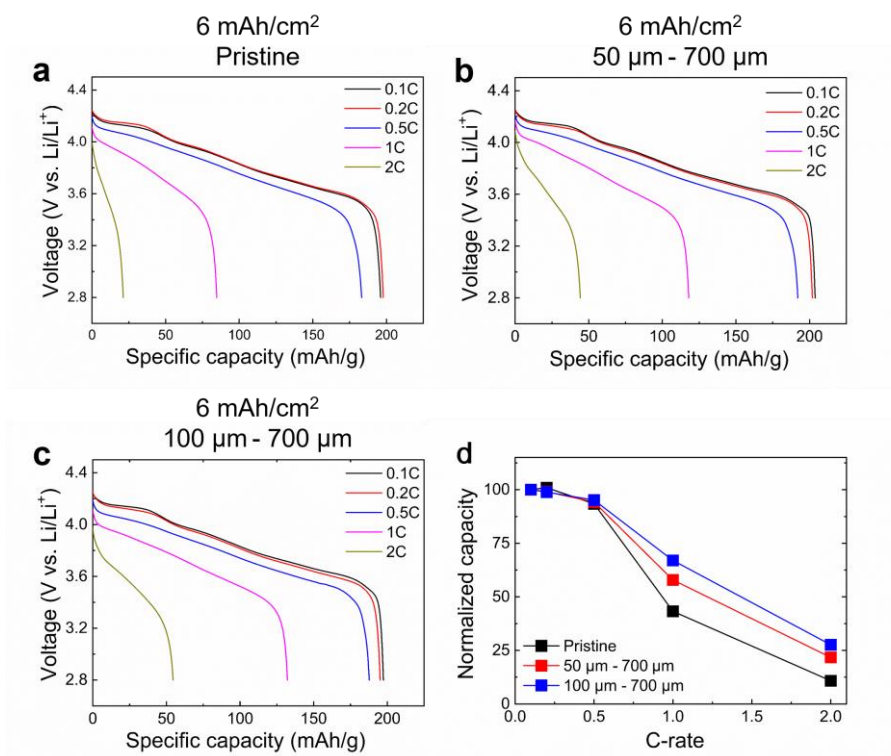
Supplementary Figure S3-3 Nano-Computed Tomography (nano-CT) images of the cross-section of a pristine 4.8 mAh/cm² electrode and the measured porosity values for different layers of the electrode. The light green and yellow layers correspond to the bottom layer closer to the Al foil and the top layer further away from the Al foil, respectively.



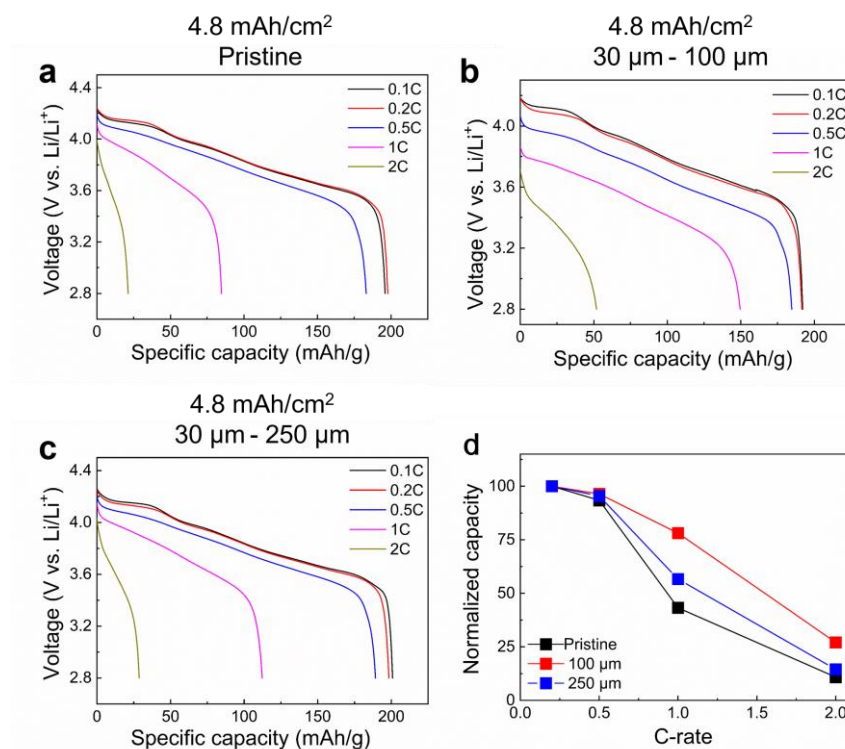
Supplementary Figure S3-4 Electrochemical performance of pristine and laser-patterned 6mAh/cm² Discharge Rate Capabilities of Unpatterned and Laser-Patterned Electrodes. The following graphs show discharge rate capability experiments for a. unpatterned electrodes and b., c., and d. laser-patterned electrodes with dimensions of 50 μm - 100 μm, 50 μm - 450 μm, and 50 μm - 700 μm, respectively. In these experiments, the charge rate remained constant at 0.1C for the 0.1C cycle and at 0.2C for the 0.2C, 0.5C, 1C, and 2C discharge rates. e. Shows the discharge rate capacities derived from Supplementary Figures S3-4a, S3-4b, S3-4c, and S3-4d, all normalized relative to the discharge rate capacities initially obtained at 0.1C.



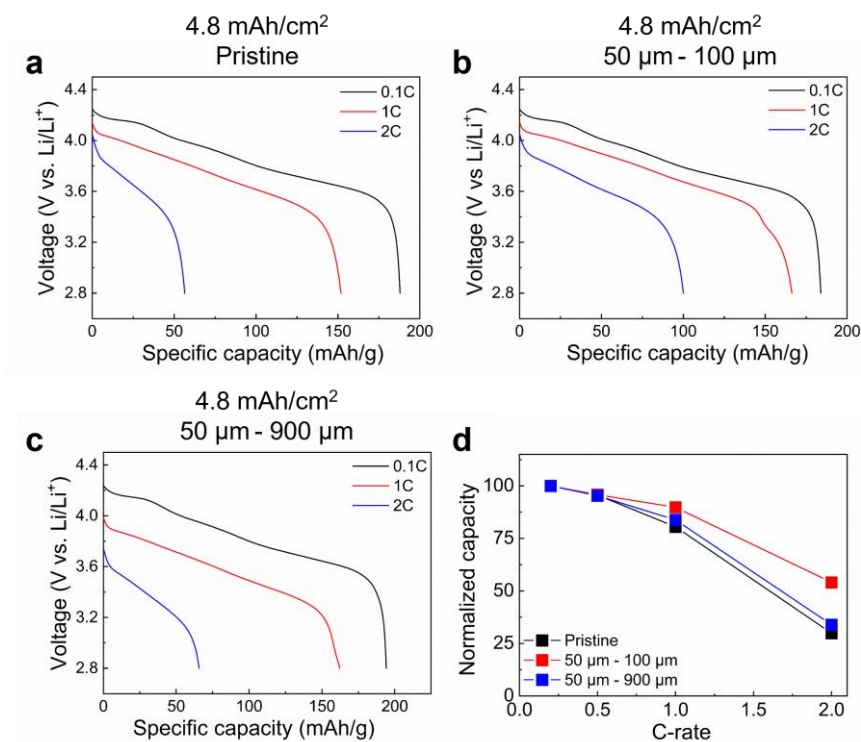
Supplementary Figure S3-5 Electrochemical performance of pristine and laser-patterned 6 mAh/cm² Comparison of discharge rate capabilities of pristine and Laser-Patterned Electrodes. The graphs shows discharge rate capability experiments for **a.** pristine electrodes and **b.** laser-patterned electrodes with dimensions ranging from 100 μm - 250 μm and **c.** 100 μm - 700 μm. In these experiments, the charge rate was kept at 0.1C for the 0.1C cycle and 0.2C for the 0.2C, 0.5C, 1C, and 2C discharge rates. Panel **d.** illustrates the discharge rate capacities deduced from Supplementary Figures S3-5a, S3-5b, and S3-5c, which are all normalized based on the capacities initially attained at a 0.1C discharge rate.



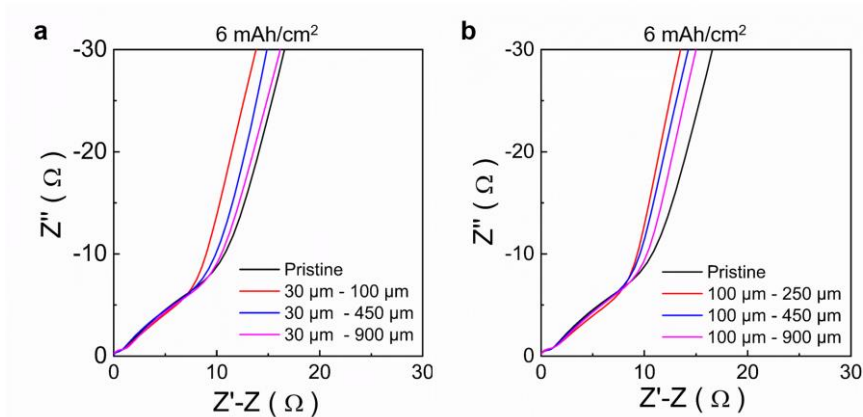
Supplementary Figure S3-6 Electrochemical performance of pristine and laser-patterned 6 mAh/cm² Comparison of Discharge Rate Capability for Pristine and Laser-Patterned Electrodes. The figure shows discharge rate capability tests for **a.** pristine and laser-patterned electrodes with dimensions of **b.** 50 μm - 700 μm and **c.** 100 μm - 700 μm. For these tests, the charge rate was fixed at 0.1C for the 0.1C cycle and 0.2C for the 0.2C, 0.5C, 1C and 2C discharge rates. Panel **d.** shows the discharge rate capacities derived from Supplementary Figures S3-6a, S3-6b and S3-6c, normalized relative to the capacities obtained at a discharge rate of 0.1C.



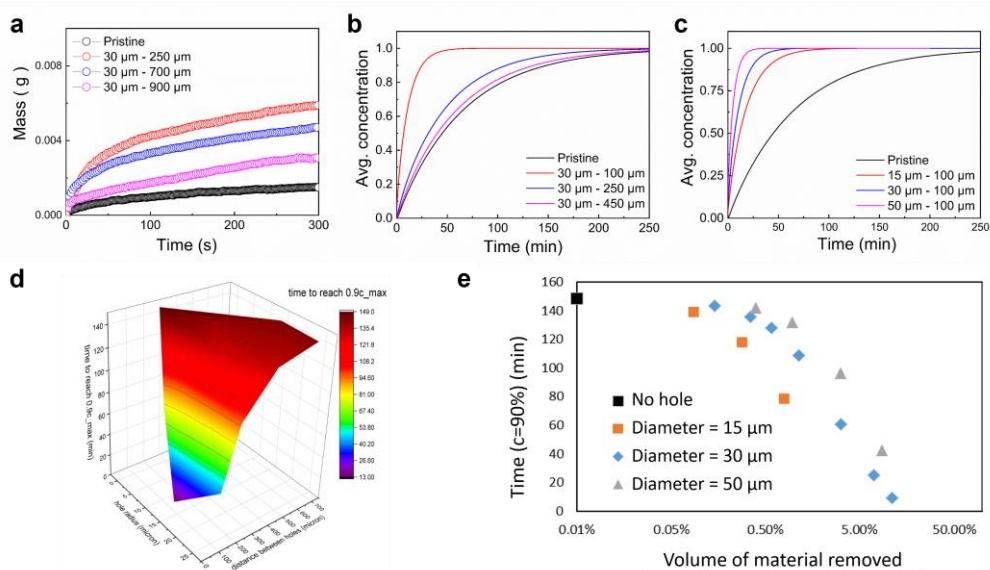
Supplementary Figure S3-7 Electrochemical performance of pristine and laser-patterned 4.8 mAh/cm² Discharge rate capability tests for a. pristine, and laser patterned b. 30 μm - 700 μm c. 30 μm – 250 μm electrode samples through which the charge rate was fixed 0.2C for discharges rates of 0.2C, 0.5C, 1C and 2C. d. Discharge rate capacities obtained in Supplementary Figures S3-7a, S3-7b and S3-7c were normalized based on the capacities obtained at 0.2C



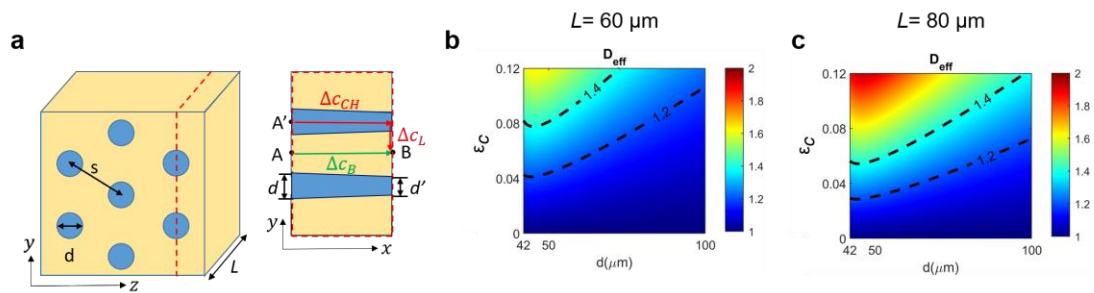
Supplementary Figure S3-8 Electrochemical performance of pristine and laser-patterned 4.8 mAh/cm² Discharge Rate Capabilities of Pristine and Laser-Patterned Electrodes. This figure shows discharge rate measurements for a. pristine, b. laser-patterned 50 μm - 100 μm, and c. laser-patterned 50 μm - 900 μm electrode samples. Throughout these experiments, the charge rate remained constant at 0.2C regardless of the discharge rate: 0.2C, 0.5C, 1C, or 2C. d. Shows the discharge rate capacities derived from Supplementary Figures S3-8a, S3-8b, and S3-8c, which are all normalized based on the discharge rate capacities initially obtained at 0.2C.



Supplementary Figure S3-9 Effect of laser-patterning on tortuosity on the channel size and the channel spacing on 6mAh/cm² laser patterned electrodes. Normalized Nyquist plot for laser-patterned channels with fixed channel size a. 30 μm or b. 100 μm.



Supplementary Figure S3-10 Evaluation of the Effect of Laser-Patterning on Electrolyte Absorption and Average Lithium Concentration. The immersion tests in a 1M LiPF₆ EC:DEC (V:V = 1:1) solution illustrate the rate of electrolyte impregnation into laser-patterned electrodes with different channel spacings. COMSOL simulations show the differences in electrolyte impregnation for pristine and laser-patterned electrodes with different channel spacing and a fixed channel diameter of b. 30 μm and c. 50 μm. As a function of channel diameter and channel spacing, plot d shows the time required to reach an average concentration of 90% of the maximum concentration in the lower electrode layer. The percentage of volume removed by laser patterning is shown in plot Supplementary Figure S3-10e.



Supplementary Figure S3-11 Effects of laser patterning on electrodes of different thicknesses and homogeneous porosities a. Illustration of a laser-patterned hexagonal array electrode with a homogeneous total porosity of 14% throughout the electrode, in which the top and bottom layers away from and closer to the aluminum current collector have the uniform porosity. Normalized effective diffusivity contour plots for b. 60 μm and c. 80 μm thick electrodes based on the steady-state electrolyte concentration gradient across the laser-patterned hexagonal array electrode.

CHAPTER 4.

FAST RATE, HIGH LOADING LASER-MICROMACHINED GRAPHITE AND SILICON BLENDED GRAPHITE ANODES FOR LITHIUM-ION BATTERY

Doyoub Kim, Alexandre Magasinski, Aashray Narla, Seung-Hun Lee, Hana Yoo, Samik Jhulki, Ah-Young Song, Jinho Hah, Gleb Yushin. *In preparation*

4.1 Introduction

In the previous chapter, it was shown that laser micromachining of patterned conical holes in thick, high areal loading NCA cathodes effectively reduces tortuous ion conduction pathways and improves electrolyte impregnation and rate performance. However, if the LIB anodes are not able to effectively operate at high current densities, charging at fast rates or reduced temperatures may lead to high Li-ion concentration, local lithium plating and “dead Li” formation negatively affecting electrochemical performance of anode materials of LIB

This study presents a comprehensive analysis of the influence of laser patterning on anode C-rate performance, with particular emphasis on the introduction of less tortuous ion conduction pathways. A trade-off between material loss due to laser micromachining and the high C-rate capacities achievable with dense graphite and SiO_x/graphite composite anodes is investigated. These anodes exhibit areal capacities of 4.8 mAh/cm² and 6 mAh/cm², respectively.

4.2 Experimental Methods

4.2.1 Preparation of electrode

The graphite electrodes used in the experiment were provided by Samsung SDI Co., Ltd. and had areal capacities of 4.8 mAh/cm² and 6 mAh/cm², densities of 1.602 g/cc and 1.6 g/cc, and a composition of over 96% active material. Variations in laser frequency, power rate, and repetitions are optimized to produce a controlled hexagonal array pattern while minimizing inadvertent damage to the electrodes using a WS-FLEX IR femtosecond laser. Laser micromachining technologies are used in conjunction with AUTOCAD design software to precisely generate the hexagonal array patterns.

4.2.2 Material Characterizations

A Panalytical XPert PRO Alpha-1 XRD was used for each XRD analysis. This made it possible to carefully examine the structural changes and impurity forms before and after the laser micromachining process. A 2 θ range from 15 to 60 degrees was covered. The samples were immersed in epoxy and allowed to cure for up to 24 hours before being cut into sections. The 4.8 mAh/cm² graphite and 6 mAh/cm² silicon mixed graphite anodes. Before being cut into sections, the samples were immersed in epoxy and allowed to cure for up to 24 hours. These specimens were then individually mounted using a 1:0.23 weight ratio of a two-part epoxy and hardening agent combination. After grinding the specimen to 4000 grit using a series of SiC papers, the specimen was polished using a 1 μ m diamond suspension on a PoliCloth (Buehler, USA). A final layer of polishing was applied using a Buehler VibroMet 2 and a 0.05 μ m colloidal silica slurry. Thorough cleaning with acetone and rinsing with isopropanol (IPA) to remove any remaining dirt or stains followed each step in this process.

A Leica digital microscope was then used to take cross-sectional images of the polished samples. To examine the channel size and spacing after laser micromachining, scanning electron microscopy (SEM SU8010) was used. In addition, 3D confocal imaging was used to analyze the pore morphology within the laser-micromachined electrodes over a range of channel widths and spacings. 3D images of the electrodes and templates were obtained using the Olympus LEXT OLS 4000 laser confocal microscope (Olympus Scientific Solutions Americas Inc., USA), which has a fixed laser wavelength of 405 nm and a magnification range of 108 to 17,000 times.

To determine the degree of electrolyte impregnation before and after laser patterning on electrodes with different channel sizes and spacings, an immersion test was performed. Pre-cut 15 mm wide strips and a Sigma 700/701 Tensiometer (Biolin Scientific AB, Beijing, CPR) were used for this procedure. A 1.0 M solution of LiPF_6 EC:DEC (V:V = 1:1) was used as the solvent. The mass of electrolyte absorbed by the electrode was recorded over time by a computer-controlled measurement procedure.

4.2.3 *Electrochemical Tests*

Following the first cycle at C/10 and C/5, further cycles were performed at different discharging rates (C/2, 1C, 2C, 3C) while keeping the charging rate at C/5. Each charge and discharge was followed by a 10 minute rest period. Electrochemical impedance spectroscopy was used to analyze the impedance and tortuosity of the electrodes. This spectroscopy was performed at open-circuit voltage after a 24-hour rest period following the formation of fresh half cells. Galvanostatic impedance data were collected between the frequencies of 100 kHz and 10 mHz. Nyquist plots were generated with an AC voltage of 10 mV.

4.3 Results and Discussion

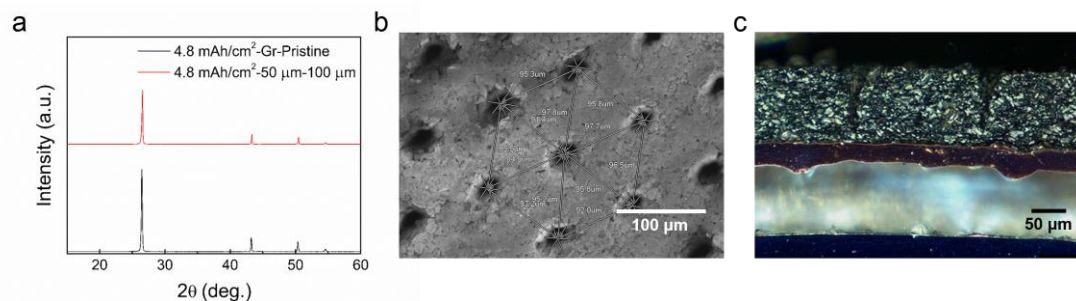


Figure 4.1 Material characterization of channel formation and morphology within a graphite electrode with a capacity of 4.8 mAh/cm² graphite electrodes. **a.** X-ray diffraction of the electrode before and after laser patterning (50 μm - 100 μm), demonstrating the absence of deleterious structural changes regardless of residual laser heat. **b.** Scanning electron microscopy (SEM) images show some non-uniform surface coloration, which may be due to heating caused during laser patterning **c.** Optical cross sectional image of a 30 μm - 100 μm laser-patterned electrode showing the formation of tapered channels.

Comparison of the X-ray diffraction (XRD) patterns of pristine and laser-patterned anodes indicates that the laser patterning and associated heat causes no obvious change in the bulk crystallinity of the electrodes (Figure 4.1a). By adjusting the laser power, repetition numbers of laser-patterning, and various other parameters of the laser source, size of the channels as well as their spacing can be modulated in a controllable manner, which allows systematic investigation of their roles in electrochemical cells.

Scanning Electron Microscope (SEM) images taken from the top view of the electrodes show that the holes are the expected size and are evenly spaced. They form a hexagonal pattern on the electrode surface (Figure 4.1b). The three-dimensional (3D) optical images show that the channels are approximately conical in shape, with the base on the electrode surface and the apex near the copper current collector. The length of these cones is equal to the thickness of the electrode as shown in the optical image of

the cross-section of the laser-patterned graphite electrode (Figure 4.1c). This shows that without seriously damaging the copper (Cu) current collector, the laser patterning technique used and the associated heat have sufficiently penetrated the entire electrode. Copper, which has a lower melting temperature (1085°C vs. 3600°C), reflects light and cools the laser-exposed area by dissipating heat, reducing the ablated area and forming conical laser-micromachined pore channels. Active mass loss due to the conical channel shape is approximately three times less than a cylindrical channel of equal radius. This effectively reduces the minimum average achievable channel radius by maintaining straight ion conduction paths to the Cu current collector. In addition, the conical shape of the channels selectively eliminates a higher proportion of the more tortuous (and possibly rate-limiting) anode area when the top layer of the electrode becomes denser and less porous. Therefore, this patterned anode design may be able to reduce through-plane tortuosity.

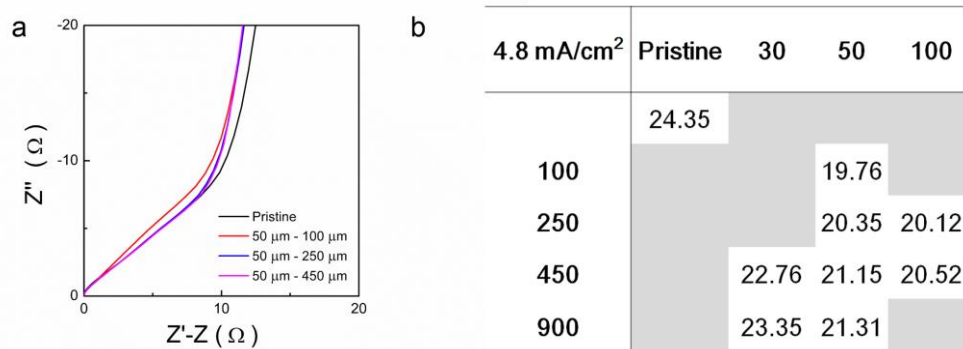


Figure 4.2 Effect of laser patterning on tortuosity and diffusivity as a function of channel spacing on 4.8 mA/cm² graphite electrode. The normalized Nyquist plot obtained for a. different laser-patterned channel sizes with channel size set to 50 μm and b. Table of McMillan numbers derived by linearly fitting the impedance of symmetric cells.

The holes are of the expected size and spacing according to scanning electron microscope (SEM) images taken from the top view of the electrodes. Studies were conducted to understand the effect of tapered channels on the overall tortuosity and wettability of the electrolyte by introducing laser-patterned graphite electrodes with tapered channels of various sizes (top/bottom diameters of approximately 30 μm , 50 μm , and 100 μm) and spacings (100 μm , 250 μm , 450 μm , and 900 μm). The first application of electrochemical impedance spectroscopy (EIS) to symmetrical cells (Fig. 4.2a) allowed the derivation of McMullin numbers, which are essentially the inverse ratio of the ionic conductance of the electrolyte-saturated electrode to the ionic conductance of the electrolyte occupying an equivalent electrode volume. Given the estimated 25% of the anode volume occupied by the electrolyte (to be confirmed), the pristine 4.8 mAh/cm² anode had a McMullin number of approximately 24.4, indicating a high degree of tortuosity. Figure 4.2b shows how the McMullin number varies with changing channel size and spacing. This study raises the possibility that ion conduction paths in the plane, as opposed to through the plane, may be less tortuous. If this were not the case, it would take too long to reach distant electrode particles from the surface of widely spaced conical channels, so the sparse micromachined channels would have little effect on the average diffusion time. It is conceivable that some of the more flexible graphitic particles could become flattened or oriented largely parallel to the electrode surface as a result of the anode calendaring process, which could result in a significant reduction in through-plane ion conduction. However, within the range of channel diameters studied, smaller channel spacing appeared to have a greater effect on tortuosity reduction than larger channel spacing.

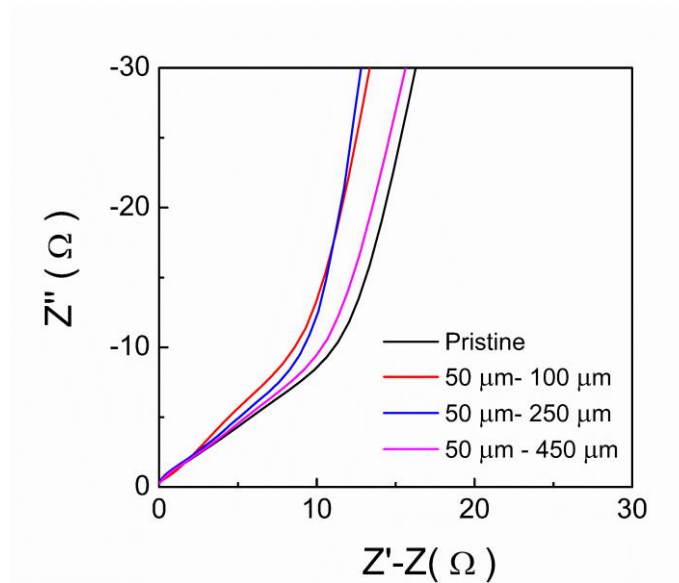


Figure 4.3 Effect of laser patterning on tortuosity and diffusivity as a function of channel spacing 6 mAh/cm² silicon blended graphite electrode. The normalized Nyquist plot obtained for a. different laser-patterned channel sizes with channel size set to 50 μm.

Upon channel micromachining, a similar trend was observed in the conductivity behavior of the 6 mAh/cm² SiOx/graphite composite anode (Fig. 4.3). The McMullin number for the pristine anode was slightly lower than that of pure graphite (22.8 vs. 24.4), indicating a possible benefit of incorporating more rigid and less deformable SiOx particles in transporting ions across the calendared anode.

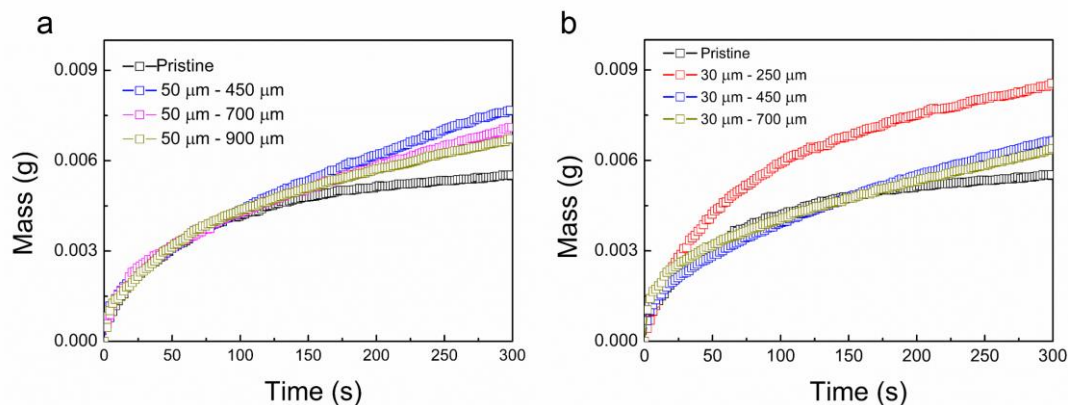


Figure 4.4 Evaluation of the effect of laser patterning on electrolyte absorption of 4.8 mAh/cm² graphite electrode. Electrode immersion measurements reveal the rate of electrolyte impregnation into laser-patterned electrodes with varying channel spacing with channel size fixed to a. 50 µm and b. 30 µm during the first 300 seconds after immersion in 1M LiPF₆ EC:DEC (V:V = 1:1) solution.

Electrolyte immersion tests were selectively performed on some of the laser-patterned 4.8 mAh/cm² graphite anodes. These anodes had moderately spaced conical channels (250-450 µm) and small to medium channel sizes (nominal base diameter of 30 and 50 µm). A significant improvement in electrolyte impregnation was observed in all patterned samples. The most significant effect was seen in the closely spaced channel pattern (250 µm spacing, Figure 4.4). The faster rate of electrolyte impregnation in the laser-patterned anodes suggests that such electrodes provide less tortuous pathways for the electrolyte to wet. This should allow for more homogeneous electrolyte flow, and thus more effective active material utilization in thick and dense anodes. These results are qualitatively consistent with the EIS studies showing the beneficial effect of conical channel arrays on Li⁺ ion transport (Figures 4.2 and 4.3).

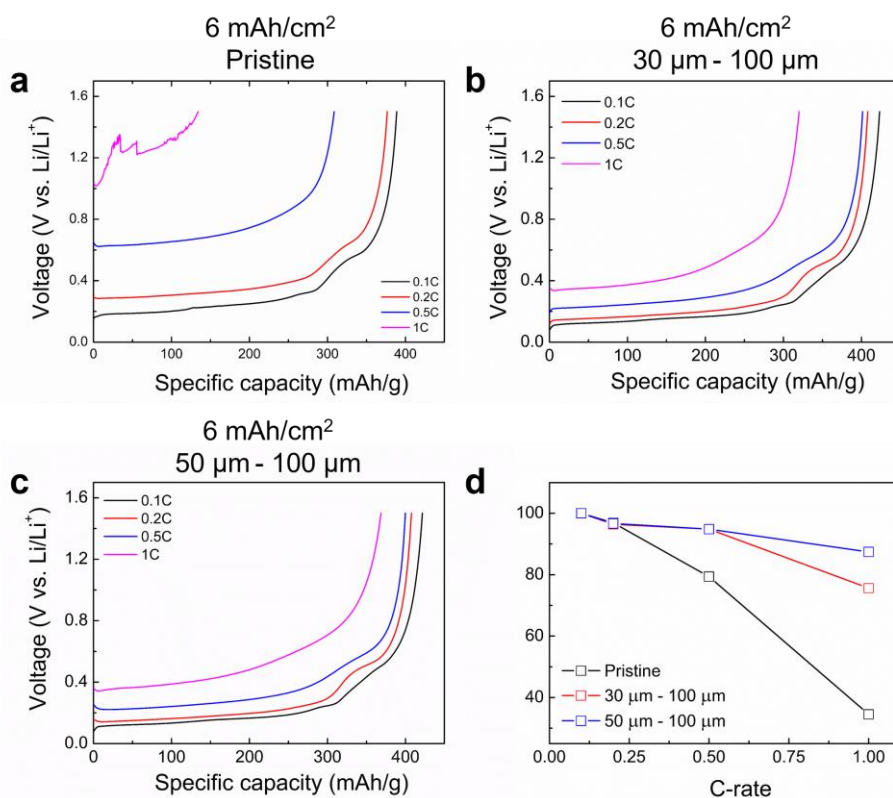


Figure 4.5 Electrochemical performance comparison of pristine and laser-patterned electrodes with capacities of 6 mAh/cm² silicon blended graphite electrodes. Charge rate capability tests for a. pristine and laser-patterned b. 30 μm – 100 μm and c. 50 μm – 100 μm. The discharge rate was held constant at 0.1C for the 0.1C cycle and 0.2C for the 0.2C, 0.5, 1C and charge rate cycles. d. The charge rate capacities shown in Figure 4.5a, Figure 4.5b, and Figure 4.5c were normalized based on the capacities obtained at 0.1C.

Based on the results of the tortuosity and electrolyte immersion experiments, it is expected that laser patterning will improve the electrochemical performance of the fast C-rate. To evaluate the C-rate capabilities of all anodes, identical conditions were applied to half-cells. The C-rates were varied from 0.1C to 2C to examine the voltage versus delithiation capacity profiles for both the SiOx/graphite composite (Figure 4.5) and the pristine and laser-perforated graphite anodes (Figure 4.6). In particular, the addition of SiOx resulted in a higher potential plateau (about 0.5 V vs. Li/Li⁺) as well as an increase in the gravimetric capacity of the anode. The voltage profile and the maximum capacity of the pristine and channel-patterned anodes were identical at the

slowest scan rate of 0.1C (as shown in Fig. 3a-c and 4a-c). However, as the current density increases, the beneficial effects of channel laser micromachining become apparent.

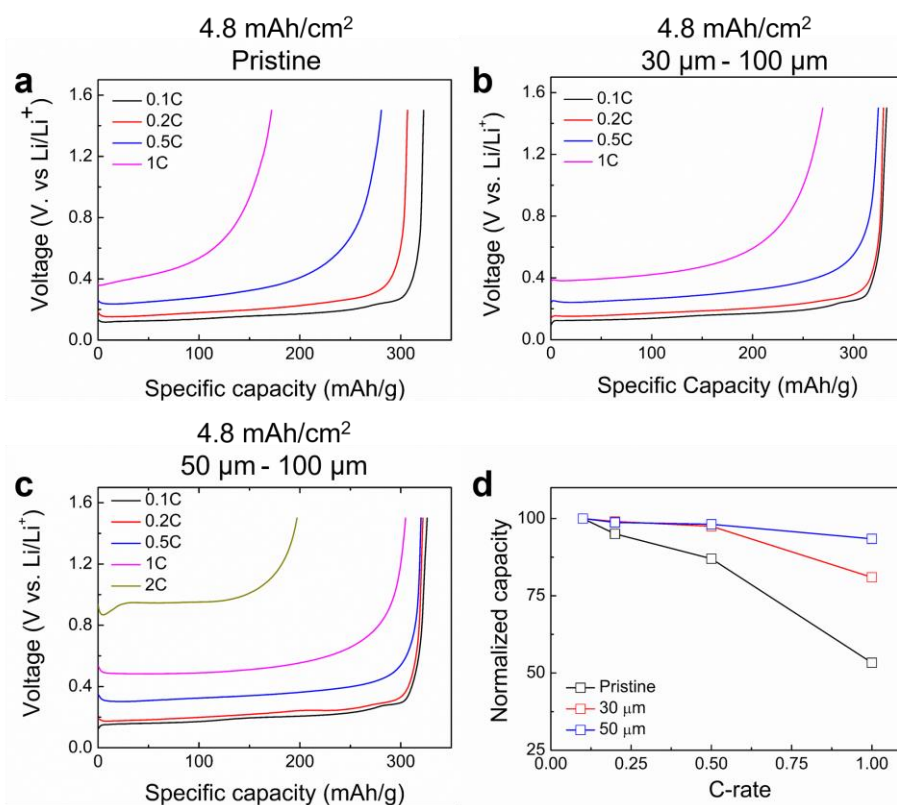


Figure 4.6 Electrochemical performance comparison of pristine and laser-patterned electrodes with capacities of 4.8 mAh/cm² graphite electrodes. Charge rate capability tests for a. pristine and laser-patterned b. 30 μm – 100 μm and c. 50 μm – 100 μm. The discharge rate was held constant at 0.1C for the 0.1C cycle and 0.2C for the 0.2C, 0.5, 1C and charge rate cycles. d. The charge rate capacities shown in Figure 4.6a, Figure 4.6b, and Figure 4.6c were normalized based on the capacities obtained at 0.1C.

Figures 4-6 and Supplementary Figure S4-2 show the effect of channel size (nominal base diameters of 30 and 50 μm) on rate capability for 100 μm and 700 μm channel arrays in a 4.8 mAh/cm² graphite anode. Significant increases in rate capability were observed for all patterned samples at C/2 and 1C rates. Increasing channel size

and decreasing spacing were both shown to improve rate performance. For example, increasing the current density from 0.1C to 1C only decreased the graphite capacitance by 7% and 19% for nominal channel diameters of 50 μm and 30 μm , respectively, at the narrowest possible channel spacing of 100 μm . In contrast, the pristine 4.8 mAh/cm^2 anode showed a reduction of more than 47%. This indicates a significantly lower performance (up to almost 6.7 times worse) in the pristine sample. A further increase in spacing to 700 μm did not result in a significant decrease in rate capability. In addition to improving rate capability, it's also important for anode materials to maintain a low potential to optimize energy density in an overall cell system. In contrast to their pristine counterparts, the laser-patterned electrodes exhibited a lower overpotential at higher C-rates due to their larger conical volume and smaller spacing. This implies that the potential of the patterned electrodes is more closely related to the thermodynamic equilibrium potential, highlighting the beneficial effects of the conical channels. For graphite anodes with high areal loading, this leads to an increase in both power density and energy density.

Upon channel formation, SiO_x /graphite composite anodes showed improvements in rate performance and a decrease in overpotential. Figures 4-5 and Supplementary Figure S4-1 show the effect of channel size on capacity retention for 100 μm and 450 μm channel arrays in an ultrahigh areal density anode (6 mAh/cm^2), comparing nominal 30 μm and 50 μm base diameters. Consistent with previous findings with a pure graphite anode, both decreasing spacing and increasing channel size improved rate performance. Specifically, the 50 μm nominal channel diameter and 100 μm pitch electrodes lost only 13% of their C/10C capacity at a 1C charge rate, while the unpatterned electrodes lost nearly 65 percent of their C/10C capacity, five times as much. The absolute values of the capacities were 400 mAh/g and 370 mAh/g at C-rates

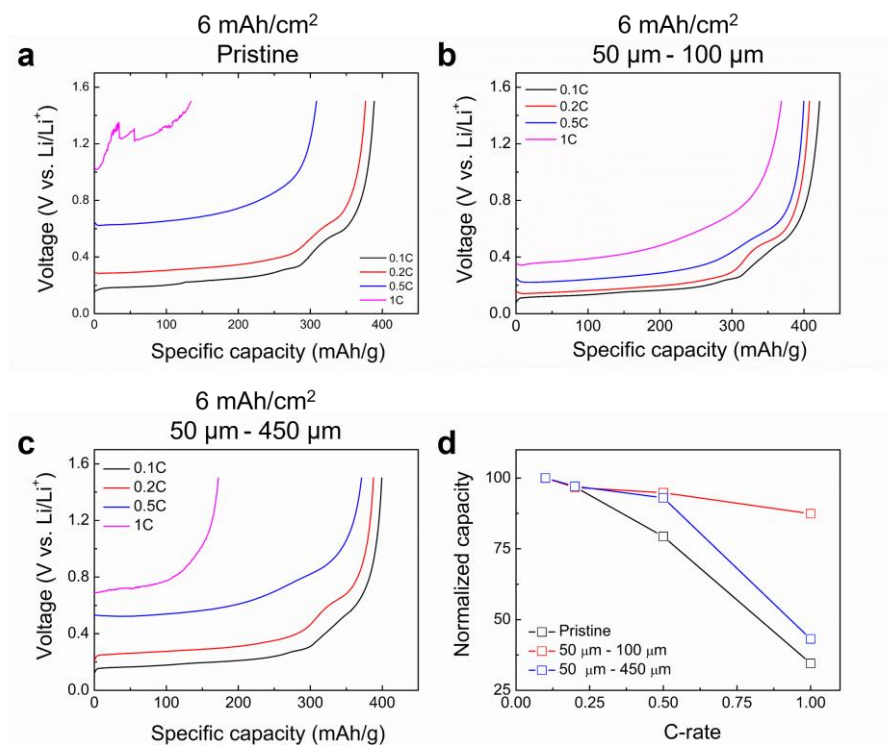
of 0.5 and 1C, respectively. In contrast, a cell with a pristine anode produced only 310 mAh/g and 130 mAh/g of capacity at the same C-rates.

Although there is a trade-off between capacity and active mass loss caused by the formation of conical channels, it is clear that the greater electrochemical performance at higher C-rates for thick and dense anodes successfully mitigates the effects of small mass loss. The introduction of additional low tortuous conduction pathways through channels of appropriate size and spacing allows for this mitigation.

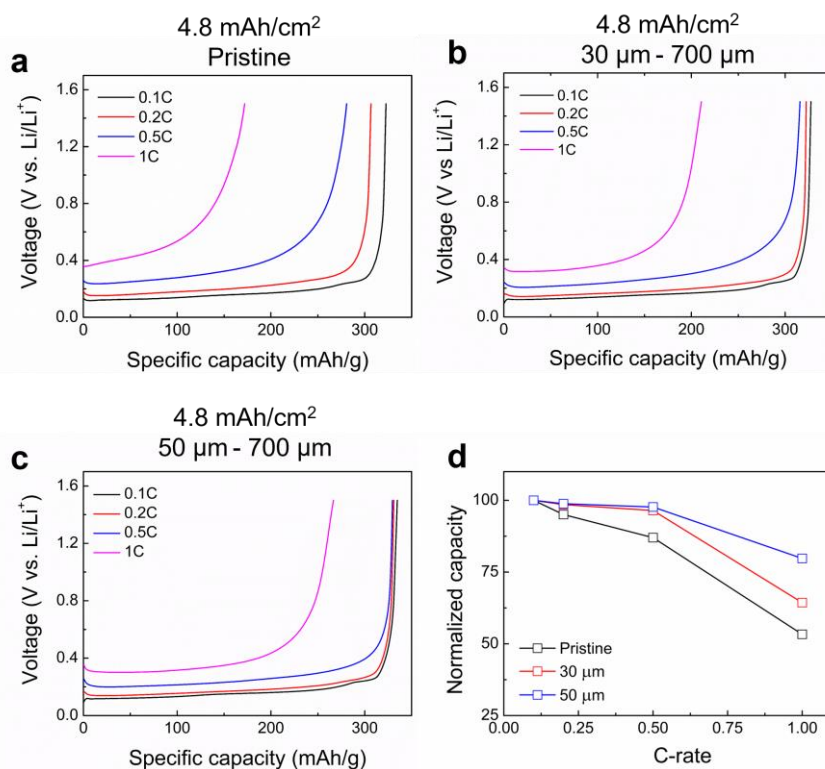
4.4 Conclusions

Taking advantage of the less tortuous ion conduction pathways created by laser patterning of thick (up to $\sim 90 \mu\text{m}$) and dense (porosity $< 20\%$; loading up to 16 mg/cm^2) electrode materials, we have demonstrated high achievable capacities for both graphite and graphite/silicon composite anodes. Although a small ($\sim 8 \%$) capacity is sacrificed due to material loss from laser patterning, the overall capacity at higher C-rates is much higher for the laser-patterned electrodes compared to the pristine, unpatterned electrodes. This is largely attributed to the faster and less tortuous ion transport and more effective electrolyte impregnation in the patterned electrodes compared to the pristine ones. Our systematic study of the electrochemical performance of thick and dense electrodes with artificially created conical channels and their comparisons with those of the pristine electrodes provides insight into the interdependence of tortuosity, electrolyte impregnation, and charge rate capability. If the knowledge disseminated and principles uncovered here can be extended to higher-capacity conversion-type anodes (e.g., Si), this strategy could dramatically improve the energy and power densities of future LIBs.

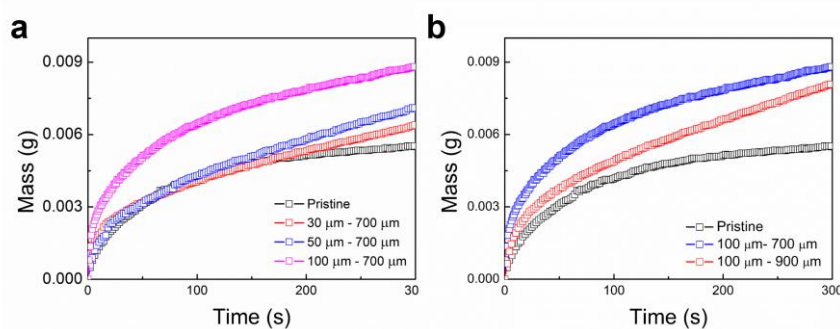
4.5 Supplementary Figures



Supplementary Figure S4-1 Electrochemical performance comparison of pristine and laser-patterned electrodes with capacities of 6 mAh/cm² silicon blended graphite electrodes. Charge rate capability tests for a. pristine and laser-patterned b. 50 μm – 100 μm and c. 50 μm – 450 μm. The discharge rate was held constant at 0.1C for the 0.1C cycle and 0.2C for the 0.2C, 0.5, 1C and charge rate cycles. d. The charge rate capacities shown in Supplementary Figure S4-1a, S4-1b, and S4-1c were normalized based on the capacities obtained at 0.1C.



Supplementary Figure S4-2 Electrochemical performance comparison of pristine and laser-patterned electrodes with capacities of 6 mAh/cm² silicon blended graphite electrodes. Charge rate capability tests for a. pristine and laser-patterned b. 50μm - 100μm and c. 50μm - 450μm. The discharge rate was held constant at 0.1C for the 0.1C cycle and 0.2C for the 0.2C, 0.5, 1C and charge rate cycles. d. The charge rate capacities shown in Supplementary Figure S4-2a, S4-2b, and S4-2c were normalized based on the capacities obtained at 0.1C.



Supplementary Figure S4-3 Evaluation of the effect of laser patterning on electrolyte absorption. Electrode immersion measurements reveal the rate of electrolyte impregnation into laser-patterned electrodes with varying channel size with channel spacing fixed to a. 700 μm and b. channel size fixed to 100 μm with varying spacing during the first 300 seconds after immersion in 1M LiPF₆ EC:DEC (V:V = 1:1) solution.

CHAPTER 5.

MICROPILLAR CHANNEL PATTERNING IN HIGH LOADING GRAPHITE AND SILICON BLENDED GRAPHITE ANODES

Doyoub Kim, Alexandre Magasinski, Seung-Hun Lee, Hana Yoo, Ah-Young Song, Gleb Yushin. Micropillar-Based Channel Patterning in High Loading Graphite Anodes for Superior Li-ion Batteries, *Submitted*

5.1 Introduction

To maximize energy density, active material fraction and anode thickness in our study were increased up to ~97 wt.% and 80 – 100 μm , respectively, while calendaring densified the electrode to keep the porosity to less than 20 vol.% to produce both high mass loading and high volumetric capacity graphite anode^{56,81,82}. Unfortunately, such thick and dense graphite electrodes notably suffer from high tortuous path for charge and Li-ion transport and subsequently experience Li plating when charged in LIB cells at a lower current density than conventional cells (with thinner and less dense anodes) and thus experience shorter cycle life, faster capacity degradation, higher potential drop at high current density and lower power.

To address these limitations in cells with thick and dense anodes, previous research investigated key parameters including active material fraction, tortuosity, porosity, electrode thickness, electrode loading and electrode structure^{40,49}. As part of electrode architecture engineering, one interesting approach was to employ a subtractive design by employing laser-micromachining to introduce straight pore channels to reduce the tortuous path of Li ions^{77,83}. Such an approach demonstrated success in both enhancing

electrolyte infiltration and facilitating a faster and more homogeneous electrochemical reactions throughout the patterned a significant electrode material loss of ~10 wt. % or even more^{41,84,85}. In addition, the volumetric capacity of such electrodes was similarly reduced by meaningful degree, thereby patterning on energy density and cost⁸⁶. In fact, in most cases the expected energy density was reduced rather than increased.

This study presents a low-cost, one-step electrode patterning method that uses a template with micropillars to indent a hexagonal array of channels in high-loading graphite anodes for faster electrolyte infiltration and Li-ion transport. In contrast to prior to studies on using laser micro-machining, active material losses could be completely avoided by the proposed methodology. The process can also be made roll-to-roll and continuous. Furthermore, the very small volume fraction of the introduced channels (<1 wt.%) has little-to-no impact on practically attainable energy density or specific energy. Yet, thus introduced pore channels significantly reduce electrolyte infiltration time and improve rate performance.

5.2 Experimental Methods

5.2.1 Material

This study is conducted using a 4.8 mAh/cm² graphite electrode with an electrode density of 1.602 g/cm³ supplied by Samsung SDI Co Ltd and an active material content of more than 96%.

5.2.2 Fabrication of a micropillar template

We fabricated a 4-inch × 4-inch square stamping template for electrode patterning using a 1-mm-thick Si wafer that was preheated at 150 °C to dehydrate

the surface of the silicon wafer to which hexamethyldisilazane (HDMS) primer had been applied. Briefly, a 7.5 μm photoresist layer (SPR 220-7.0) was uniformly deposited on the surface of the Si wafer using a spin-coating apparatus. The 900 μm hexagonal pattern in the photoresist was created using MLA Heidelberg (Heidelberg Instruments Inc, USA). After UV irradiation at a dose of 650 kJ/cm^2 and a laser wavelength of 405 nm, the photoresist cured and was removed from unpatterned areas using Microposit MF-319 developer. The silicon wafer was etched to form a trapezoidal tip and a silicon needle column using isotropic and anisotropic etching, respectively, using HRM ICP equipment (Surface Technology System, USA). Sulfur hexafluoride (SF_6) was used for isotropic etching to form the tip, while anisotropic etching involved sequentially alternating etching and passivation steps based on Bosch technology, using SF_6 and octafluorocyclobutane (C_4F_8) for etching and passivation, respectively. Oxygen was added to the SF_6 during the pickling step to improve sidewall passivation. The desired needle column height (50 to 350 μm) was achieved by repeating the etching cycles. By using the so-called Bosch process for Si etching and by controlling the etching conditions and the number of etching cycles, we fine-tuned the height of the micropillar columns and ⁸⁷. After 150 and 300 etching/passivation cycles by anisotropic etching, the column heights were up to 180 μm . SEM images of the prepared Si wafer stamp template show that the micropillars are cylindrical with the top edge in the shape of a tapered angled cone.

5.2.3 *Material characterization*

A scanning electron microscope was used to examine the top and side views of the micro-pillars on the fabricated silicon wafer template, as well as the top view of the

hexagonal array patterned electrode using the micro-pillar template, to observe the channel size and spacing of the indented patterns, and the width and the spacing of the fabricated micro-pillars.

Electrolyte wettability experiments were performed on pre-cut 15 mm wide strips using the DCAT 25 (Dataphysics, USA) and the wetting solvent was 1.0 M lithium hexafluorophosphate (LiPF₆) EC:DEC (V:V = 1:1) (Battery, Sigma, USA).

5.2.4 *Electrochemical Tests*

A cycle at rates of C/10 and C/5 is followed by additional cycles at different charge rates (C/5, C/2, and 1C) while the discharge rate remains constant at C/5. Cycle performance of graphite electrodes before and after 50 cycles at 0.5C following the initial 2 cycles at 0.1C and 2 cycles at 0.2C. A slower charge of 0.2C was used after each 1C charge. After 24 hours of rest, symmetrical cells were subjected to electrochemical impedance spectroscopy, which measured impedance data in a galvanostatic mode over a frequency range of 100 kHz to 10 mHz and used a 10 mV AC voltage amplitude to analyze electrode impedance and McMullin number of unpatterned and patterned electrodes.

5.3 Results and discussion

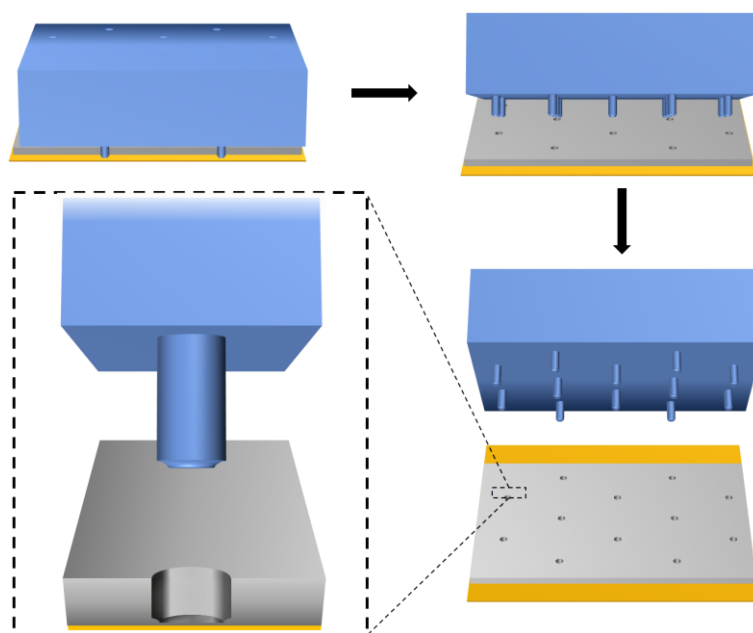


Figure 5.1 Schematic of the electrode patterning process using a hexagonal array of micro-pillars on a silicon wafer template with a hexagonal pattern. The process uses the stamping template to create an array of indentations or holes in fully densified, high mass loading graphite anodes in a matter of seconds.

We used a silicon (Si) wafer furnished with a custom-designed array of micropillars as a stamping template in this study (as shown in Fig. 1). In completely densified high-loading graphite anodes, we were able to produce an array of indentations, which can be characterized as straight pore channels or holes, in a relatively short time of a few seconds (as shown in Figure 5.1). Notably, this technique of imprinting arrays of indentations may also be suitable for other electrode types, such as those in mixed graphite-Si anodes. In addition, the process is designed to be transferred to a continuous roll-to-roll operation.

The primary goal was to design a hexagonal array of holes, ranging from conical to cylindrical in shape, extending to the top surface of the copper (Cu) current collector foils. From a pragmatic standpoint, conical holes might be more desirable due to their smaller volume fraction. Sparse conical holes, characterized by a tapered angle, have the potential to retain more than 99% of the initial volumetric electrode capacity, assuming the electrode density within the hole-free regions remains constant. As shown in Table 2.1, the combined effects of smaller hole diameters and larger spacing lead to a reduced volume fraction of holes. Notably, our method does not require the removal of any active materials, an important consideration. The simplicity, speed, and minimal active material loss associated with this one-step patterning process are key advantages, particularly for cost-sensitive applications such as lithium-ion batteries for electric vehicles.

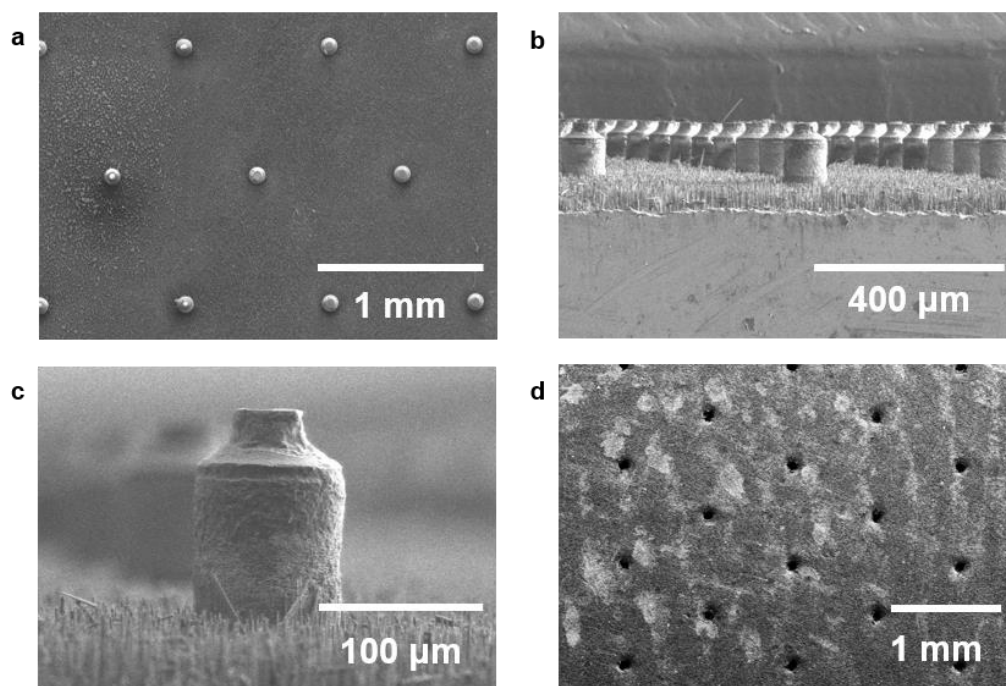


Figure 5.2 SEM images of the hexagonal array in top view, the micropillars in side view, a single micropillar in side view, and the top view of micropillar channels fabricated on a graphite electrode with 100 μm and 900 μm channel size and spacing.

In this work, we fabricated a 4-inch by 4-inch square stamping template for electrode patterning using a 1-mm-thick Si wafer. Scanning electron microscope (SEM) images of the fabricated Si wafer stamping template show that the micropillars have a cylindrical shape with a tapered, angled, truncated cone at the top. As shown in Figure 5-2, these micropillars have impressively succeeded in introducing hexagonal array channel indentations into highly mass loading graphite anodes.

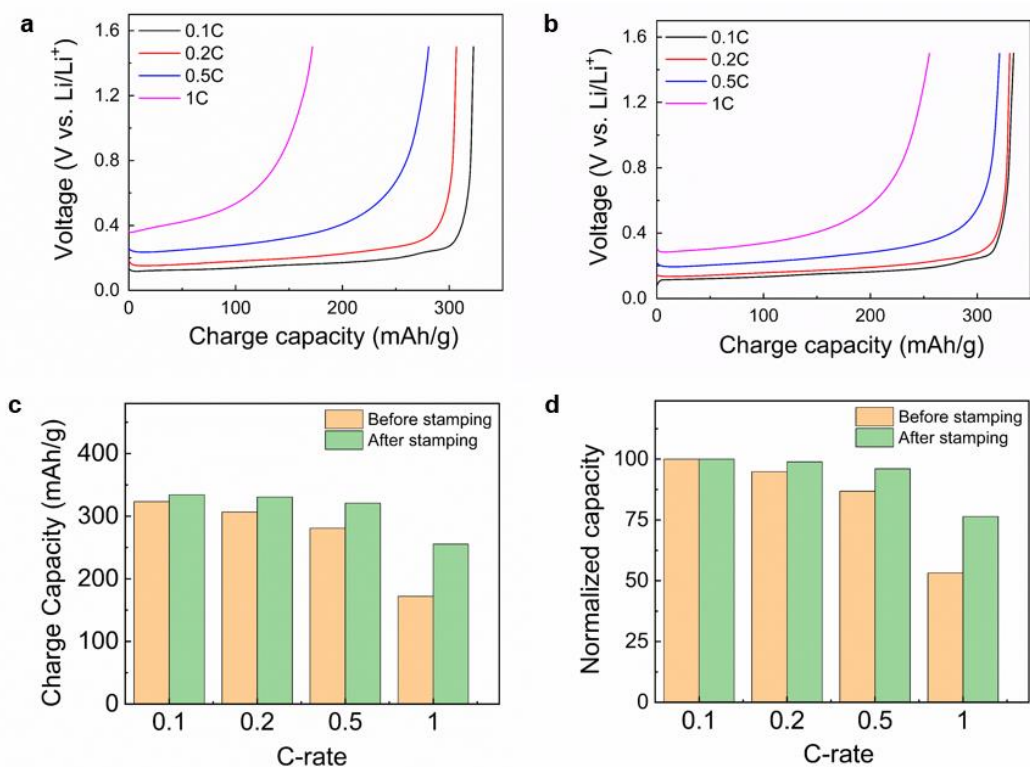


Figure 5.3 Charge curves of graphite anode at different C-rates a) before and b) after stamping using micropillar-based silicon wafer template for patterning hexagonal array patterns on thick and dense graphite electrodes. The effect of the hexagonal array patterning using the micropillar-based silicon wafer template on the c. specific and d. normalized charge capacities is further elucidated by comparative bar graphs.

Charge-discharge measurements at various current densities were performed on both plain and patterned electrodes in half-cell configurations to evaluate the effect of electrode architecture on rate performance (Figure 5.3). Both unpatterned and patterned electrodes exhibited a specific capacity of approximately 323 mAh/g and 334 mAh/g, respectively, at a rate of 0.1C. The achievable capacity of the patterned electrode showed a slight decrease of only 4 mAh/g (a tiny 1.1% with respect to the 0.1C capacity) when the charging C-rate was increased to 0.2C. The pristine electrode, on the other hand, had a more significant drop of 16 mAh/g and a 5% decrease in capacity compared to its 0.1C capacity (Figure 5.3c). As the C-rate increases, the disparity between specific and

normalized capacities becomes more apparent (Figure 5.3d). Surprisingly, even when the C-rate increases to 0.5C, the patterned electrode maintains an extraordinarily high capacity of about 321 mAh/g, or about 96.1% of its 0.1C capacity. On the other hand, the capacity of the unpatterned electrode gradually decreases to a specific capacity of 280 mAh/g, which is about 87% of its 0.1C capacity (see Fig. 3d). The patterned electrode retains a specific capacity of 255 mAh/g at a C-rate of 1C, which is 76% of its 0.1C capacity. In comparison, the perfect electrode has a drastically reduced specific capacity of 171 mAh/g, which is only 53% of its 0.1C capacity (see Fig. 3d). The much greater capacity retention at 1C current density (charge/discharge cycle shorter than 1h) (see Fig. 3d) serves as evidence that the thick and dense graphite electrode has a rate capability much greater than that of the pristine electrode. These trends indicate that a less tortuous ion transport pathway and improved electrolyte impregnation effectively prevent undesirable rapid capacity fading and contribute to the improved rate performance of thick and dense electrodes at high current density.

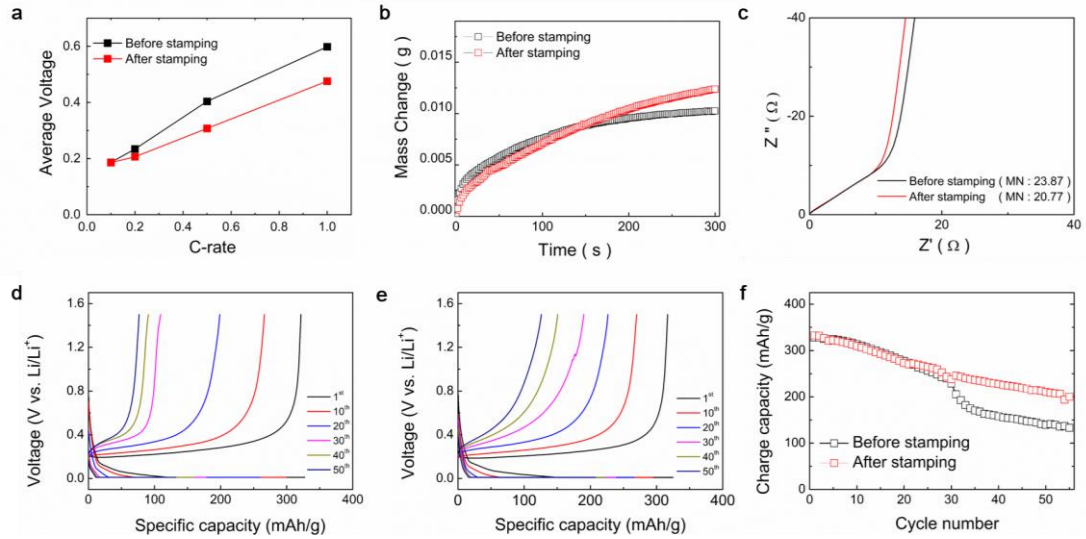


Figure 5.4 a. the average voltage at different C-rates before and after patterning with hexagonal arrays. **b.** An immersion test performed both before and after patterning to demonstrate the effect of micropillar patterning. **c.** An impedance measurement of the symmetrical cell is performed to derive the McMullin number both before and after patterning on the thick and dense graphite anode electrodes. MN is the McMullin number. The voltage profile of the **d.** pre-stamped and **e.** post-stamped 4.8 mAh/cm^2 graphite electrodes at 0.5C spanning from the 1st to the 50th cycle in the potential range of $0.01 \sim 1.6\text{V}$ (vs. Li/Li^+) is shown. **f.** The cycling performance of the pre- and post-stamped graphite electrodes at 0.5C for 50 cycles following the initial 2 cycles at 0.1C and 2 cycles at 0.2C is shown. Each 0.5C charge cycle was followed by a slower 0.2C charge.

The average operating potentials of the unpatterned and patterned electrodes (Figure 5.4a) during electrochemical testing further indicate that electrode patterning has a beneficial effect. Because it optimizes the achievable cell voltage and reduces the likelihood of Li plating^{22,23}, low-voltage hysteresis-defined as a higher average operating potential of an anode during charging and a lower average operating potential of an anode during discharge-is essential to LIB performance and safety. Higher voltage between the cathode and anode optimizes volumetric and gravimetric energy densities, while avoiding Li dendrites improves cycle life and safety, and enables faster charging²⁴⁻²⁷.

Both pristine and patterned electrodes show highly comparable average working potentials of 0.186V and 0.185V vs. Li/Li⁺ during discharge, similar to the comparison of 0.1C capacities. Only 0.027V separates the two states before and after micropillar-based patterning. However, at 1C (Figure 5.4a), the difference increases to -0.097V (the average working potentials of the pristine and patterned electrodes are around 0.404 V and 0.307 V, respectively). In summary, the patterned graphite electrode has a much lower average working potential, which ensures significantly higher energy densities, especially at higher C-rates.

To evaluate the average tortuosity of these electrodes and to determine the effect of introducing stamped pore channels on electrolyte wettability, pristine and patterned electrodes were prepared for use in (i) electrochemical impedance spectroscopy (EIS) tests in symmetrical cells in a non-faradaic environment. Electrolyte wettability test results (Figure 5.4b) show that patterned electrodes provide avenues for much faster electrolyte impregnation compared to pristine graphite electrodes. More efficient electrolyte filling would lead to faster LIB cell fabrication and perhaps even greater use of active elements in thick and dense electrodes (assuming such filling was previously inadequate). The McMullin number is a ratio between the ionic conductance of the electrodes and a numerical representation of the tortuosity of the electrode. The McMullin numbers were obtained from the EIS measurements. These tests showed that the micropillar template patterned graphite electrode significantly reduced the tortuosity (Figure 5.4c), indicating that the patterned channels should make it easier for Li ions to move along a less tortuous path and improve the rate performance of thick and dense graphite electrodes. The unpatterned graphite electrode also showed less favorable cycle stability in half cells (Figure 5.4f). A

half-cell platform cannot evaluate excellent cycle stability for large area electrodes due to the instability and volume changes of the lithium foil counter electrode. The conclusion is that mechanical electrode patterning does not result in faster degradation and likely has the opposite effect.

5.3 Conclusion

In summary, micropillar-based channel patterning for EV applications avoids trade-offs between rate performance and active material removal. Instead, it demonstrates a straightforward one-step channel patterning technique on a high-load graphite anode that facilitates electrolyte wetting, lowers tortuosity, improves rate performance, and reduces overpotential at fast charge C-rates while preventing inadvertent loss of active material from the LIB anode. We anticipate that micropillar technology can be easily adapted to use micropillar rollers and extended to continuous operation.

CHAPTER 6.

CONCLUSION AND FUTURE WORK

6.1 Conclusion

This thesis focuses on improving the performance of lithium-ion (Li-ion) batteries, focusing on electric vehicle (EV) applications. The focus is on mitigating the obstacles associated with high areal capacity automotive cathodes and anodes, including the formation of dense layers on the cathode surface that reduce ion transport kinetics and consequently battery rate performance.

A notable proposed solution involves laser patterning to create conical and tapered channels within the cathode material. These channels are shown to reduce the average ion transport distance, thereby improving electrolyte wetting and promoting more efficient ion transport.

The strategy also improves ion accessibility to electrode particles at high C-rates in thick and dense nickel cobalt aluminum oxide (NCA) cathodes. A key finding is the critical balance between the loss of mass (volumetric capacity) due to laser patterning and the increase in capacity retention due to faster ion transport. The research delves into a systematic analysis of this balance by modifying the size and spacing of the channels.

The work includes detailed experimental observations and diffusion modeling to explore the intricate interactions between electrochemical performance, tortuosity, and electrolyte wetting. The results are expected to provide significant advances in the design of Li-ion battery electrodes for automotive applications, enabling the

achievement of higher power and energy density at the cell level. This development can further the development of more affordable, longer range EVs while maintaining a high charging speed.

The thesis also demonstrates the possibility of achieving high capacity for both graphite and graphite/silicon composite anodes, albeit with a minor sacrifice in capacity due to the laser patterning. This outcome is primarily attributed to the faster and less tortuous ion transport and more effective electrolyte impregnation observed in the patterned electrodes as compared to pristine ones.

Moreover, a micropillar-based channel patterning technique is proposed for EV applications. This one-step method exhibits promise in enhancing electrolyte wetting, reducing tortuosity, improving rate performance, and reducing overpotential at fast charge C-rates, while effectively minimizing loss of active material from the LIB anode.

In conclusion, the research presents a compelling avenue for enhancing the performance of Li-ion batteries, particularly for EV applications, through the implementation of laser patterning and micropillar-based channel creation. It is envisioned that this technology can be seamlessly adapted for continuous operation, significantly boosting the energy and power densities of future LIBs.

6.1 Future work

Future research efforts should focus on combining different state-of-the-art methods to gain a better understanding of electrodes materials in order to advance energy storage technologies. Combining electrochemical cell performance testing with high-resolution nano/micro-CT imaging of electrodes, researchers could observe the detailed structure and porosity of electrodes at the nano/microscale, providing

important new information about electrode homogeneity and utilization and shape, morphology and distribution of active materials. The identical electrodes will be tested in parallel for electrochemical performance in complete cell configurations, providing relevant information on the correlation between the electrochemical behavior and electrode design parameters. In addition, it could help identify significant relationships between electrode microstructure and electrochemical performance, thereby allowing the discovery of important electrode design factors that could mitigate the limitations of thick and dense battery electrodes.

The study could be further advanced by using multi-physics machine learning techniques. When data from electrochemical performance cell testing and nano-CT imaging are put together, these advanced algorithms can find intricate correlations and patterns in the huge data sets that are made. Beyond the analytical capabilities of humans, the multi-physics machine learning system would be able to identify complex correlations between electrode microstructure and electrochemical performance. Researchers could unlock the potential for creating next-generation energy storage devices with unrivaled performance characteristics by using this new technique to reveal hidden design principles and recommendations for improving electrode materials. Ultimately, this multidisciplinary line of research has the potential to transform the energy storage industry and open the door to future energy solutions that are more efficient and sustainable.

APPENDICES

A.1 Permission for the Reuse of Copyright Materials

Licensed Content		Order Details	
Licensed Content Publisher	Springer Nature	Type of Use	Thesis/Dissertation
Licensed Content Publication	Nature	Requestor type	academic/university or research institute
Licensed Content Title	Issues and challenges facing rechargeable lithium batteries	Format	electronic
Licensed Content Author	J.-M. Tarascon et al	Portion	figures/tables/illustrations
Licensed Content Date	Nov 15, 2001	Number of figures/tables/illustrations	1
		Will you be translating?	no
		Circulation/distribution	1 - 29
		Author of this Springer Nature content	no
About Your Work		Additional Data	
Title	Graduate student	Portions	1
Institution name	Georgia Institute of Technology		
Expected presentation date	Jul 2023		
Requestor Location		Tax Details	
	Georgia Institute of Technology 771 Ferst Dr NW		
Requestor Location			
	ATLANTA, GA 30332 United States Attn: Georgia Institute of Technology		
Price			
Total	0.00 USD		

Total: 0.00 USD

SPRINGER NATURE

A non-academic perspective on the future of lithium-based batteries
Author: James T. Frith et al
Publication: Nature Communications
Publisher: Springer Nature
Date: Jan 26, 2023
Copyright © 2023, The Author(s)

Creative Commons
This is an open access article distributed under the terms of the [Creative Commons CC BY](#) license, which permits unrestricted use, distribution, and reproduction in any medium, provided the original work is properly cited.
You are not required to obtain permission to reuse this article.
To request permission for a type of use not listed, please contact [Springer Nature](#)

ACS Publications
Most Trusted. Most Cited. Most Read.

The Li-Ion Rechargeable Battery: A Perspective
Author: John B. Goodenough, Kyu-Sung Park
Publication: Journal of the American Chemical Society
Publisher: American Chemical Society
Date: Jan 1, 2013
Copyright © 2013, American Chemical Society

PERMISSION/LICENSE IS GRANTED FOR YOUR ORDER AT NO CHARGE

This type of permission/license, instead of the standard Terms and Conditions, is sent to you because no fee is being charged for your order. Please note the following:

- Permission is granted for your request in both print and electronic formats, and translations.
- If figures and/or tables were requested, they may be adapted or used in part.
- Please print this page for your records and send a copy of it to your publisher/graduate school.
- Appropriate credit for the requested material should be given as follows: "Reprinted (adapted) with permission from (COMPLETE REFERENCE CITATION), Copyright (YEAR) American Chemical Society." Insert appropriate information in place of the capitalized words.
- One-time permission is granted only for the use specified in your RightsLink request. No additional uses are granted (such as derivative works or other editions). For any uses, please submit a new request.

If credit is given to another source for the material you requested from RightsLink, permission must be obtained from that source.

[BACK](#)

[CLOSE WINDOW](#)

A-.2 US Patent



US 20210050599A1

(19) **United States**
 (12) **Patent Application Publication** (10) **Pub. No.: US 2021/0050599 A1**
 LEE et al. (43) **Pub. Date: Feb. 18, 2021**

(54) **HIGH LOADING ELECTRODES HAVING HIGH AREAL CAPACITY AND ENERGY STORAGE DEVICES INCLUDING THE SAME**
H01M 4/505 (2006.01)
H01M 10/0525 (2006.01)
H01M 4/38 (2006.01)
H01M 4/131 (2006.01)
H01M 4/133 (2006.01)
 (71) Applicants: **Samsung SDI Co., Ltd.**, Yongin-si (KR); **GEORGIA TECH RESEARCH CORPORATION**, Atlanta, GA (US)
H01G 11/66 (2006.01)
H01G 11/24 (2006.01)
H01G 11/52 (2006.01)
 (72) Inventors: **Seunghun LEE**, Yongin-si (KR); **Gleb YUSHIN**, Atlanta, GA (US); **Doyoub KIM**, Atlanta, GA (US)
 (52) **U.S. Cl.**
 CPC *H01M 4/80* (2013.01); *H01M 4/525* (2013.01); *H01M 4/0435* (2013.01); *H01M 4/505* (2013.01); *H01M 10/0525* (2013.01); *H01M 2004/021* (2013.01); *H01M 4/131* (2013.01); *H01M 4/133* (2013.01); *H01G 11/66* (2013.01); *H01G 11/24* (2013.01); *H01G 11/52* (2013.01); *H01M 4/38* (2013.01)
 (21) Appl. No.: **16/994,037**
 (22) Filed: **Aug. 14, 2020**

Related U.S. Application Data

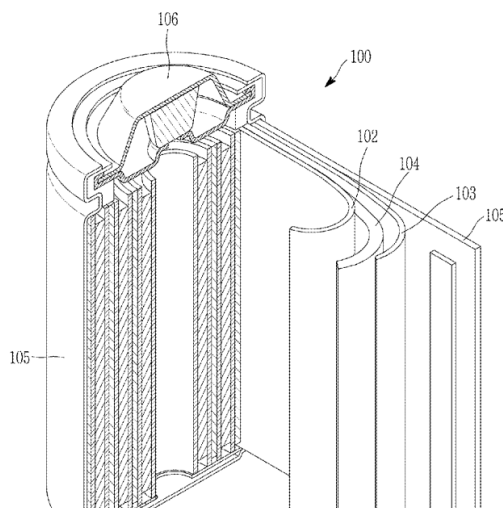
(60) Provisional application No. 62/888,203, filed on Aug. 16, 2019.

Publication Classification

(51) **Int. Cl.**
H01M 4/80 (2006.01)
H01M 4/525 (2006.01)
H01M 4/04 (2006.01)

(57) **ABSTRACT**

Provided is a high areal capacity loading electrode that includes: a metal current collector; and an active material layer on the metal current collector, wherein the electrode has high areal capacity loading of greater than or equal to about 2.0 mAh/cm², and the electrode is perforated with holes spaced from each other at an average distance ranging from about 70 μm to about 900 μm. An energy storage device including the high loading electrode is also provided.



A.3 Korea Patent



공개특허 10-2021-0020850

	(19) 대한민국특허청(KR) (12) 공개특허공보(A)	(11) 공개번호 10-2021-0020850 (43) 공개일자 2021년02월24일
(51) 국제특허분류(Int. Cl.) HO1M 4/13 (2010.01) HO1G 11/22 (2013.01) HO1G 11/70 (2013.01) HO1M 10/052 (2010.01) HO1M 4/02 (2006.01) HO1M 4/131 (2010.01) HO1M 4/133 (2010.01) HO1M 4/74 (2006.01)		(71) 출원인 삼성에스디아이 주식회사 경기도 용인시 기흥구 공세로 150-20 (공세동) 조지아 테크 리서치 코오포레이션 미국 조지아주 30332-0415 아틀란타 엔터블유 델 니 스트리트 926
(52) CPC특허분류 HO1M 4/13 (2013.01) HO1G 11/22 (2021.01)		(72) 발명자 이승훈 경기도 용인시 기흥구 공세로 150-20(공세동) 글렘 유신 미국 조지아주 30332-0415 아틀란타 10번가 505 김도엽 미국 조지아주 30332-0415 아틀란타 10번가 505
(21) 출원번호 10-2020-0103565 (22) 출원일자 2020년08월18일 심사청구일자 없음 (30) 우선권주장 62/888,203 2019년08월16일 미국(US)		(74) 대리인 팬코리아특허법인

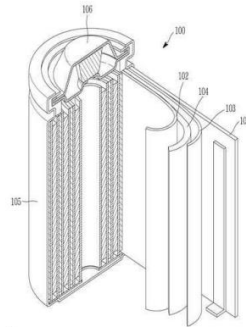
전체 청구항 수 : 총 17 항

(54) 발명의 명칭 **높은 면적당 용량을 가지는 고 로딩 전극 및 이를 포함하는 에너지 저장 장치**

(57) 요약

금속 집전체 및 상기 금속 집전체 위에 배치된 활물질층을 포함하는 전극으로, 상기 전극은 4.0 mAh/cm² 이상의 면적 용량 로딩량을 가지고, 상기 전극은 70 μm 내지 900 μm 간격으로 배치된 홀(hole)을 포함하고, 상기 홀은 규칙적인 육각형 패턴을 가지는 고 로딩 전극을 제공한다. 또한 상기 고 로딩 전극을 포함하는 에너지 저장 장치를 제공한다.

대표도



References

- 1 Raupach, M. R. *et al.* Global and regional drivers of accelerating CO₂ emissions. *Proceedings of the National Academy of Sciences* **104**, 10288-10293 (2007). <https://doi.org/doi:10.1073/pnas.0700609104>
- 2 Canadell, J. G. *et al.* Contributions to accelerating atmospheric CO₂ growth from economic activity, carbon intensity, and efficiency of natural sinks. *Proceedings of the National Academy of Sciences* **104**, 18866-18870 (2007). <https://doi.org/doi:10.1073/pnas.0702737104>
- 3 Manisalidis, I., Stavropoulou, E., Stavropoulos, A. & Bezirtzoglou, E. Environmental and Health Impacts of Air Pollution: A Review. *Frontiers in Public Health* **8** (2020). <https://doi.org/10.3389/fpubh.2020.00014>
- 4 Chang, S. Y. *et al.* Electric vehicle fleet penetration helps address inequalities in air quality and improves environmental justice. *Communications Earth & Environment* **4**, 135 (2023). <https://doi.org/10.1038/s43247-023-00799-1>
- 5 Xie, J. & Lu, Y.-C. A retrospective on lithium-ion batteries. *Nature Communications* **11**, 2499 (2020). <https://doi.org/10.1038/s41467-020-16259-9>
- 6 Manthiram, A. A reflection on lithium-ion battery cathode chemistry. *Nature Communications* **11**, 1550 (2020). <https://doi.org/10.1038/s41467-020-15355-0>
- 7 Frith, J. T., Lacey, M. J. & Ulissi, U. A non-academic perspective on the future of lithium-based batteries. *Nature Communications* **14**, 420 (2023). <https://doi.org/10.1038/s41467-023-35933-2>
- 8 Turcheniuk, K., Bondarev, D., Amatucci, G. G. & Yushin, G. Battery materials for low-cost electric transportation. *Materials Today* **42**, 57-72 (2021). [https://doi.org:https://doi.org/10.1016/j.mattod.2020.09.027](https://doi.org/https://doi.org/10.1016/j.mattod.2020.09.027)
- 9 Gonzalez, J. M. *et al.* Designing diversified renewable energy systems to balance multisector performance. *Nature Sustainability* **6**, 415-427 (2023). <https://doi.org/10.1038/s41893-022-01033-0>
- 10 Headley, A. J. & Copp, D. A. Energy storage sizing for grid compatibility of intermittent renewable resources: A California case study. *Energy* **198**, 117310 (2020). <https://doi.org:https://doi.org/10.1016/j.energy.2020.117310>
- 11 Nykvist, B. & Nilsson, M. Rapidly falling costs of battery packs for electric vehicles. *Nature Climate Change* **5**, 329-332 (2015). <https://doi.org/10.1038/nclimate2564>
- 12 Tarascon, J. M. & Armand, M. Issues and challenges facing rechargeable lithium batteries. *Nature* **414**, 359-367 (2001).

<https://doi.org/10.1038/35104644>

- 13 Ozawa, K. Lithium-ion rechargeable batteries with LiCoO₂ and carbon electrodes: the LiCoO₂/C system. *Solid State Ionics* **69**, 212-221 (1994). [https://doi.org/10.1016/0167-2738\(94\)90411-1](https://doi.org/10.1016/0167-2738(94)90411-1)
- 14 Megahed, S. & Scrosati, B. Lithium-ion rechargeable batteries. *Journal of Power Sources* **51**, 79-104 (1994). [https://doi.org/10.1016/0378-7753\(94\)01956-8](https://doi.org/10.1016/0378-7753(94)01956-8)
- 15 Manthiram, A., Knight, J. C., Myung, S.-T., Oh, S.-M. & Sun, Y.-K. Nickel-Rich and Lithium-Rich Layered Oxide Cathodes: Progress and Perspectives. *Advanced Energy Materials* **6**, 1501010 (2016). <https://doi.org/10.1002/aenm.201501010>
- 16 Myung, S.-T. *et al.* Nickel-Rich Layered Cathode Materials for Automotive Lithium-Ion Batteries: Achievements and Perspectives. *ACS Energy Letters* **2**, 196-223 (2017). <https://doi.org/10.1021/acseenergylett.6b00594>
- 17 Goodenough, J. B. & Park, K.-S. The Li-ion rechargeable battery: a perspective. *Journal of the American Chemical Society* **135**, 1167-1176 (2013).
- 18 Noelle, D. J., Wang, M., Le, A. V., Shi, Y. & Qiao, Y. Internal resistance and polarization dynamics of lithium-ion batteries upon internal shorting. *Applied Energy* **212**, 796-808 (2018). <https://doi.org/10.1016/j.apenergy.2017.12.086>
- 19 Lyu, Y. *et al.* An Overview on the Advances of LiCoO₂ Cathodes for Lithium-Ion Batteries. *Advanced Energy Materials* **11**, 2000982 (2021). <https://doi.org/10.1002/aenm.202000982>
- 20 Li, M. & Lu, J. Cobalt in lithium-ion batteries. *Science* **367**, 979-980 (2020). <https://doi.org/10.1126/science.aba9168>
- 21 Xie, M. Stabilizing an amorphous V₂O₅/carbon nanotube paper electrode with conformal TiO₂ coating by atomic layer deposition for lithium ion batteries. *Journal of Materials Chemistry A* **4**, 537-544 (2016).
- 22 Fu, W., Kim, D., Wang, F. & Yushin, G. Stabilizing cathodes and interphases for next-generation Li-ion batteries. *Journal of Power Sources* **561**, 232738 (2023). <https://doi.org/10.1016/j.jpowsour.2023.232738>
- 23 Wang, X., Ding, Y.-L., Deng, Y.-P. & Chen, Z. Ni-Rich/Co-Poor Layered Cathode for Automotive Li-Ion Batteries: Promises and Challenges. *Advanced Energy Materials* **10**, 1903864 (2020). <https://doi.org/10.1002/aenm.201903864>
- 24 Zeng, X. *et al.* Commercialization of Lithium Battery Technologies for Electric Vehicles. *Advanced Energy Materials* **9**, 1900161 (2019). <https://doi.org/10.1002/aenm.201900161>

- 25 Kim, J. *et al.* Prospect and Reality of Ni-Rich Cathode for Commercialization. *Advanced Energy Materials* **8**, 1702028 (2018). <https://doi.org/10.1002/aenm.201702028>
- 26 Patry, G., Romagny, A., Martinet, S. & Froelich, D. Cost modeling of lithium-ion battery cells for automotive applications. *Energy Science & Engineering* **3**, 71-82 (2015). <https://doi.org/10.1002/ese3.47>
- 27 Sun, Y.-K. *et al.* Nanostructured high-energy cathode materials for advanced lithium batteries. *Nature Materials* **11**, 942-947 (2012). <https://doi.org/10.1038/nmat3435>
- 28 Lim, B.-B. *et al.* Advanced Concentration Gradient Cathode Material with Two-Slope for High-Energy and Safe Lithium Batteries. *Advanced Functional Materials* **25**, 4673-4680 (2015). <https://doi.org/10.1002/adfm.201501430>
- 29 Lee, J. H. *et al.* High-energy-density lithium-ion battery using a carbon-nanotube–Si composite anode and a compositionally graded Li[Ni_{0.85}Co_{0.05}Mn_{0.10}]O₂ cathode. *Energy & Environmental Science* **9**, 2152-2158 (2016). <https://doi.org/10.1039/C6EE01134A>
- 30 Zhao, E. *et al.* Local structure adaptability through multi cations for oxygen redox accommodation in Li-Rich layered oxides. *Energy Storage Materials* **24**, 384-393 (2020). <https://doi.org/10.1016/j.ensm.2019.07.032>
- 31 Hong, J. *et al.* Metal–oxygen decoordination stabilizes anion redox in Li-rich oxides. *Nature Materials* **18**, 256-265 (2019). <https://doi.org/10.1038/s41563-018-0276-1>
- 32 Eum, D. *et al.* Voltage decay and redox asymmetry mitigation by reversible cation migration in lithium-rich layered oxide electrodes. *Nature Materials* **19**, 419-427 (2020). <https://doi.org/10.1038/s41563-019-0572-4>
- 33 Jarvis, K. *et al.* Surface Reconstruction in Li-Rich Layered Oxides of Li-Ion Batteries. *Chemistry of Materials* **29**, 7668-7674 (2017). <https://doi.org/10.1021/acs.chemmater.7b00120>
- 34 Luo, W. *et al.* Surface and Interface Engineering of Silicon-Based Anode Materials for Lithium-Ion Batteries. *Advanced Energy Materials* **7**, 1701083 (2017). <https://doi.org/10.1002/aenm.201701083>
- 35 Jin, Y., Zhu, B., Lu, Z., Liu, N. & Zhu, J. Challenges and Recent Progress in the Development of Si Anodes for Lithium-Ion Battery. *Advanced Energy Materials* **7**, 1700715 (2017). <https://doi.org/10.1002/aenm.201700715>
- 36 Zuo, X., Zhu, J., Müller-Buschbaum, P. & Cheng, Y.-J. Silicon based lithium-ion battery anodes: A chronicle perspective review. *Nano Energy* **31**, 113-143 (2017). <https://doi.org/10.1016/j.nanoen.2016.11.013>

- 37 He, S. *et al.* Considering Critical Factors of Silicon/Graphite Anode Materials for Practical High-Energy Lithium-Ion Battery Applications. *Energy & Fuels* **35**, 944-964 (2021). <https://doi.org/10.1021/acs.energyfuels.0c02948>
- 38 Eshetu, G. G. *et al.* Production of high-energy Li-ion batteries comprising silicon-containing anodes and insertion-type cathodes. *Nature Communications* **12**, 5459 (2021). <https://doi.org/10.1038/s41467-021-25334-8>
- 39 Heubner, C. *et al.* Recent Insights into Rate Performance Limitations of Li-ion Batteries. *Batteries & Supercaps* **4**, 268-285 (2021). <https://doi.org/10.1002/batt.202000227>
- 40 Boyce, A. M. *et al.* Design of Scalable, Next-Generation Thick Electrodes: Opportunities and Challenges. *ACS Nano* **15**, 18624-18632 (2021). <https://doi.org/10.1021/acsnano.1c09687>
- 41 Shodiev, A. *et al.* Deconvoluting the benefits of porosity distribution in layered electrodes on the electrochemical performance of Li-ion batteries. *Energy Storage Materials* **47**, 462-471 (2022). <https://doi.org/10.1016/j.ensm.2022.01.058>
- 42 Lim, J. *et al.* Origin and hysteresis of lithium compositional spatiodynamics within battery primary particles. *Science* **353**, 566-571 (2016). <https://doi.org/10.1126/science.aaf4914>
- 43 Wood, M. *et al.* Impact of secondary particle size and two-layer architectures on the high-rate performance of thick electrodes in lithium-ion battery pouch cells. *Journal of Power Sources* **515**, 230429 (2021). <https://doi.org/10.1016/j.jpowsour.2021.230429>
- 44 Röder, F., Sonntag, S., Schröder, D. & Krewer, U. Simulating the Impact of Particle Size Distribution on the Performance of Graphite Electrodes in Lithium-Ion Batteries. *Energy Technology* **4**, 1588-1597 (2016). <https://doi.org/10.1002/ente.201600232>
- 45 Zeng, C., Liang, J., Cui, C., Zhai, T. & Li, H. Dynamic Investigation of Battery Materials via Advanced Visualization: From Particle, Electrode to Cell Level. *Advanced Materials* **34**, 2200777 (2022). <https://doi.org/10.1002/adma.202200777>
- 46 Lu, X. *et al.* Multi-length scale microstructural design of lithium-ion battery electrodes for improved discharge rate performance. *Energy & Environmental Science* **14**, 5929-5946 (2021). <https://doi.org/10.1039/D1EE01388B>
- 47 Müller, S. *et al.* Quantifying Inhomogeneity of Lithium Ion Battery Electrodes and Its Influence on Electrochemical Performance. *Journal of The Electrochemical Society* **165**, A339 (2018). <https://doi.org/10.1149/2.0311802jes>
- 48 Iqbal, N., Ali, Y. & Lee, S. Chemo-mechanical response of composite electrode

- systems with multiple binder connections. *Electrochimica Acta* **364**, 137312 (2020). <https://doi.org/10.1016/j.electacta.2020.137312>
- 49 Zhu, P., Slater, P. R. & Kendrick, E. Insights into architecture, design and manufacture of electrodes for lithium-ion batteries. *Materials & Design* **223**, 111208 (2022). <https://doi.org/10.1016/j.matdes.2022.111208>
- 50 Elango, R. *et al.* Impact of electrode porosity architecture on electrochemical performances of 1 mm-thick LiFePO₄ binder-free Li-ion electrodes fabricated by Spark Plasma Sintering. *Journal of Power Sources* **488**, 229402 (2021). <https://doi.org/10.1016/j.jpowsour.2020.229402>
- 51 Sakamoto, Y. K. D. C. M. Improving Li-ion battery charge rate acceptance through highly ordered hierarchical electrode design. *Ionics* **24**, 2935-2943 (2018). <https://doi.org/10.1007/s11581-018-2502-x>
- 52 Huang, C. & Grant, P. S. Coral-like directional porosity lithium ion battery cathodes by ice templating. *Journal of Materials Chemistry A* **6**, 14689-14699 (2018). <https://doi.org/10.1039/C8TA05049J>
- 53 Huang, C., Dontigny, M., Zaghbi, K. & Grant, P. S. Low-tortuosity and graded lithium ion battery cathodes by ice templating. *Journal of Materials Chemistry A* **7**, 21421-21431 (2019). <https://doi.org/10.1039/C9TA07269A>
- 54 Hyun, G. *et al.* Three-Dimensional, Submicron Porous Electrode with a Density Gradient to Enhance Charge Carrier Transport. *ACS Nano* **16**, 9762-9771 (2022). <https://doi.org/10.1021/acsnano.2c03480>
- 55 Zhang, X. *et al.* Tunable Porous Electrode Architectures for Enhanced Li-Ion Storage Kinetics in Thick Electrodes. *Nano Letters* **21**, 5896-5904 (2021). <https://doi.org/10.1021/acs.nanolett.1c02142>
- 56 Itou, Y., Ogihara, N. & Kawauchi, S. Role of Conductive Carbon in Porous Li-Ion Battery Electrodes Revealed by Electrochemical Impedance Spectroscopy Using a Symmetric Cell. *The Journal of Physical Chemistry C* **124**, 5559-5564 (2020). <https://doi.org/10.1021/acs.jpcc.9b11929>
- 57 Orikasa, Y. *et al.* Ionic Conduction in Lithium Ion Battery Composite Electrode Governs Cross-sectional Reaction Distribution. *Scientific Reports* **6**, 26382 (2016). <https://doi.org/10.1038/srep26382>
- 58 Ogihara, N., Itou, Y. & Kawauchi, S. Ion Transport in Porous Electrodes Obtained by Impedance Using a Symmetric Cell with Predictable Low-Temperature Battery Performance. *The Journal of Physical Chemistry Letters* **10**, 5013-5018 (2019). <https://doi.org/10.1021/acs.jpcclett.9b01670>
- 59 Pietsch, P. *et al.* Quantifying microstructural dynamics and electrochemical activity of graphite and silicon-graphite lithium ion battery anodes. *Nature Communications* **7**, 12909 (2016). <https://doi.org/10.1038/ncomms12909>

- 60 Ebner, M., Chung, D.-W., García, R. E. & Wood, V. Tortuosity Anisotropy in Lithium-Ion Battery Electrodes. *Advanced Energy Materials* **4**, 1301278 (2014). <https://doi.org/10.1002/aenm.201301278>
- 61 Landesfeind, J., Hattendorff, J., Ehrl, A., Wall, W. A. & Gasteiger, H. A. Tortuosity Determination of Battery Electrodes and Separators by Impedance Spectroscopy. *Journal of The Electrochemical Society* **163**, A1373 (2016). <https://doi.org/10.1149/2.1141607jes>
- 62 Pouraghajan, F. *et al.* Quantifying Tortuosity of Porous Li-Ion Battery Electrodes: Comparing Polarization-Interrupt and Blocking-Electrolyte Methods. *Journal of The Electrochemical Society* **165**, A2644 (2018). <https://doi.org/10.1149/2.061181jes>
- 63 Kuang, Y., Chen, C., Kirsch, D. & Hu, L. Thick Electrode Batteries: Principles, Opportunities, and Challenges. *Advanced Energy Materials* **9**, 1901457 (2019). <https://doi.org/10.1002/aenm.201901457>
- 64 Kang, J., Atwair, M., Nam, I. & Lee, C.-J. Experimental and numerical investigation on effects of thickness of NCM622 cathode in Li-ion batteries for high energy and power density. *Energy* **263**, 125801 (2023). <https://doi.org/10.1016/j.energy.2022.125801>
- 65 Duffner, F., Mauler, L., Wentker, M., Leker, J. & Winter, M. Large-scale automotive battery cell manufacturing: Analyzing strategic and operational effects on manufacturing costs. *International Journal of Production Economics* **232**, 107982 (2021). <https://doi.org/10.1016/j.ijpe.2020.107982>
- 66 Ziegler, M. S., Song, J. & Trancik, J. E. Determinants of lithium-ion battery technology cost decline. *Energy & Environmental Science* **14**, 6074-6098 (2021). <https://doi.org/10.1039/D1EE01313K>
- 67 Li, W., Erickson, E. M. & Manthiram, A. High-nickel layered oxide cathodes for lithium-based automotive batteries. *Nature Energy* **5**, 26-34 (2020). <https://doi.org/10.1038/s41560-019-0513-0>
- 68 Liu, Y., Zhu, Y. & Cui, Y. Challenges and opportunities towards fast-charging battery materials. *Nature Energy* **4**, 540-550 (2019). <https://doi.org/10.1038/s41560-019-0405-3>
- 69 Heubner, C. *et al.* Understanding thickness and porosity effects on the electrochemical performance of LiNi_{0.6}Co_{0.2}Mn_{0.2}O₂-based cathodes for high energy Li-ion batteries. *Journal of Power Sources* **419**, 119-126 (2019). <https://doi.org/10.1016/j.jpowsour.2019.02.060>
- 70 Kalnaus, S., Livingston, K., Hawley, W. B., Wang, H. & Li, J. Design and processing for high performance Li ion battery electrodes with double-layer structure. *Journal of Energy Storage* **44**, 103582 (2021). <https://doi.org/10.1016/j.est.2021.103582>

- 71 Gallagher, K. G. *et al.* Optimizing Areal Capacities through Understanding the Limitations of Lithium-Ion Electrodes. *Journal of The Electrochemical Society* **163**, A138 (2016). <https://doi.org/10.1149/2.0321602jes>
- 72 Doyle, M. & Newman, J. Analysis of capacity–rate data for lithium batteries using simplified models of the discharge process. *Journal of Applied Electrochemistry* **27**, 846-856 (1997). <https://doi.org/10.1023/A:1018481030499>
- 73 Bae, C.-J., Erdonmez, C. K., Halloran, J. W. & Chiang, Y.-M. Design of Battery Electrodes with Dual-Scale Porosity to Minimize Tortuosity and Maximize Performance. *Advanced Materials* **25**, 1254-1258 (2013). <https://doi.org/https://doi.org/10.1002/adma.201204055>
- 74 Cobb, C. L. & Blanco, M. Modeling mass and density distribution effects on the performance of co-extruded electrodes for high energy density lithium-ion batteries. *Journal of Power Sources* **249**, 357-366 (2014). <https://doi.org/https://doi.org/10.1016/j.jpowsour.2013.10.084>
- 75 Lasagni, A. F. *et al.* *Direct laser interference patterning, 20 years of development: from the basics to industrial applications*. Vol. 10092 PWL (SPIE, 2017).
- 76 Habedank, J. B. *et al.* Increasing the Discharge Rate Capability of Lithium-Ion Cells with Laser-Structured Graphite Anodes: Modeling and Simulation. *Journal of The Electrochemical Society* **165**, A1563 (2018). <https://doi.org/10.1149/2.1181807jes>
- 77 Dunlap, N. *et al.* Laser ablation for structuring Li-ion electrodes for fast charging and its impact on material properties, rate capability, Li plating, and wetting. *Journal of Power Sources* **537**, 231464 (2022). <https://doi.org/https://doi.org/10.1016/j.jpowsour.2022.231464>
- 78 Singh, M., Kaiser, J. & Hahn, H. Thick Electrodes for High Energy Lithium Ion Batteries. *Journal of The Electrochemical Society* **162**, A1196 (2015). <https://doi.org/10.1149/2.0401507jes>
- 79 Kostovski, G., Stoddart, P. R. & Mitchell, A. The Optical Fiber Tip: An Inherently Light-Coupled Microscopic Platform for Micro- and Nanotechnologies. *Advanced Materials* **26**, 3798-3820 (2014). <https://doi.org/https://doi.org/10.1002/adma.201304605>
- 80 Othonos, A., Kalli, K., Pureur, D. & Mugnier, A. in *Wavelength Filters in Fibre Optics* (ed Herbert Venghaus) 189-269 (Springer Berlin Heidelberg, 2006).
- 81 Malifarge, S., Delobel, B. & Delacourt, C. Experimental and Modeling Analysis of Graphite Electrodes with Various Thicknesses and Porosities for High-Energy-Density Li-Ion Batteries. *Journal of The Electrochemical Society* **165**, A1275 (2018). <https://doi.org/10.1149/2.0301807jes>

- 82 Quarti, M., Bayer, A. & Bessler, W. G. Trade-off between energy density and fast-charge capability of lithium-ion batteries: A model-based design study of cells with thick electrodes. *Electrochemical Science Advances* **3**, e2100161 (2023). <https://doi.org/10.1002/elsa.202100161>
- 83 Elango, R., Demortière, A., De Andrade, V., Morcrette, M. & Seznec, V. Thick Binder-Free Electrodes for Li-Ion Battery Fabricated Using Templating Approach and Spark Plasma Sintering Reveals High Areal Capacity. *Advanced Energy Materials* **8**, 1703031 (2018). <https://doi.org/10.1002/aenm.201703031>
- 84 Shodiev, A. *et al.* Designing electrode architectures to facilitate electrolyte infiltration for lithium-ion batteries. *Energy Storage Materials* **49**, 268-277 (2022). <https://doi.org/10.1016/j.ensm.2022.03.049>
- 85 Wilhelm Pfleging, J. P. A new approach for rapid electrolyte wetting in tape cast electrodes for lithium-ion batteries. *Journal of Materials Chemistry A* **2**, 14918-14926 (2014). <https://doi.org/10.1039/c4ta02353f>
- 86 Wood, D. L., Li, J. & Daniel, C. Prospects for reducing the processing cost of lithium ion batteries. *Journal of Power Sources* **275**, 234-242 (2015). <https://doi.org/10.1016/j.jpowsour.2014.11.019>
- 87 Samco. *What is the Bosch Process (deep reactive ion etching)?*, (2020).